Engineering Journal

American Institute of Steel Construction

Third Quarter 2016 Volume 53, No. 3

www.aisc.org

Kinematics of Self-Centering Steel Plate Shear Walls with NewZ-BREAKSS Post-Tensioned Rocking Connection

DANIEL M. DOWDEN and MICHEL BRUNEAU

ABSTRACT

This paper presents information on the combined contribution of post-tensioning and beam-to-column joint rocking connections in self-centering steel plate shear walls (SC-SPSWs) with the NewZ-BREAKSS connection (i.e., NZ-SC-SPSW). Detailed free-body diagrams developed and presented in this paper provide insights on the basic, fundamental kinematic behavior of this lateral force-resisting system. The fundamental equations presented provide information on the behavior of SC-SPSWs and are suitable to facilitate design. These are needed for the implementation and understanding of these types of self-centering steel frame systems.

Keywords: rocking connection; self-centering; steel plate shear wall; moment frame; seismic response; resilient structure; seismic performance.

INTRODUCTION

Conventional steel lateral force-resisting systems (LFRSs) that comply with current building codes and the AISC seismic provisions (AISC, 2010) used in the United States are typically expected to suffer damage during moderate to severe earthquakes. Designed in accordance with prescribed detailing requirements proven by research to ensure ductile response (and protect occupants), these structural systems are not expected to collapse during a severe earthquake but will likely require significant repairs following a design level earthquake. Furthermore, the structure could be left with significant residual drifts and visible leaning following the earthquake (AIJ, 1995; Krawinkler et al., 1996; Kawashima et al., 1998; Christopoulos et al., 2003; Pampanin et al., 2003). Thus, although current conventional LFRSs can meet the code-specified objective of collapse prevention for standard buildings, significant structural damage occurs (albeit controlled damage), preventing use of the building for a significant repair period after a design level earthquake and possibly leading to demolition of the building in some cases. This seismic performance is typically expected for conventional LFRSs of any material and construction.

Recent research (Winkley, 2011; Clayton, 2013; Dowden, 2014) on self-centering steel plate shear walls (SC-SPSWs) has demonstrated that structures can be designed to achieve greater performance objectives by providing frame recentering capabilities after a seismic event, together with replaceable, energy-dissipating components. This self-centering capability in SPSWs is achieved here by using beam-to-column post-tensioned (PT) moment rocking frame connections, similar to what was done in past research on self-centering moment frames (e.g., Ricles et al., 2002; Christopoulos et al., 2002; Garlock et al., 2005; Rojas et al., 2005). However, to be fully successful, such self-centering strategies need to account for the interaction (due to the PT boundary frame expansion) between the LFRS and the gravity frame. Because self-centering buildings could economically provide a level of protection designated as available for "immediate occupancy" following an earthquake, this design strategy makes sense from a life-cycle cost perspective.

Toward that goal, this paper presents information on the analytical modeling and kinematics of a SC-SPSW with the proposed NewZ-BREAKSS (NZ) rocking connection (Dowden and Bruneau, 2011), a beam-to-column joint detail inspired by a moment-resisting connection developed and implemented in New Zealand (Clifton, 1996, 2005; Clifton et al., 2007; MacRae et al., 2008). This PT beam-to-column (i.e., horizontal boundary element–to–vertical boundary element, or HBE-to-VBE) rocking connection seeks to eliminate PT boundary frame expansion (i.e., beam

Daniel M. Dowden, Research Engineer, Structural Engineering and Earthquake Simulation Laboratory, Department of Civil, Structural, and Environmental Engineering, University at Buffalo, University at Buffalo, Buffalo, NY (corresponding). Email: dmdowden@buffalo.edu

Michel Bruneau, Professor, Department of Civil, Structural, and Environmental Engineering, University at Buffalo, University at Buffalo, Buffalo, NY. Email: bruneau@buffalo.edu

Paper No. 2015-23R

growth) that occurs in all the other previously researched rocking connections (referenced earlier). First, a review of the basic principles of the NZ-SC-SPSW is presented, from which equations for the moment, shear and axial force diagrams along the HBE are obtained from a capacity design approach based on yielding of the SPSW infill web plates. Using the derived equations, numerical models are then developed and results are compared with the closed-form analytical equations. Next, additional insight on the global force-displacement response of the NZ-SC-SPSW frame is provided through nonlinear monotonic pushover analyses. Furthermore, detailed free-body diagrams are developed to investigate infill web plate demands with frames with HBE-to-VBE rocking connections. Finally, insight on unrestrained PT boundary frame expansion of frames with HBE-to-VBE rocking connections gained from experiments (Dowden and Bruneau, 2014; Dowden et al., 2016) is provided, leading to an improved NewZ-BREAKSS detail.

BASIC PRINCIPLES OF THE NZ-SC-SPSW SYSTEM

An SC-SPSW differs from a conventional SPSW in that HBE-to-VBE rigid moment connections in a conventional SPSW are replaced by PT rocking moment connections. This allows a joint gap opening to form between the VBE and HBE interface about a rocking point, leading to a PT elongation, which is the self-centering mechanism. This particular rocking connection then eliminates PT boundary frame expansion typically encountered in the previously researched connections (that rock about both of their beam flanges) by, instead, maintaining constant contact of the HBE top flange with the VBEs during lateral drift. By doing so, when one of the rocking joint "opens," the rocking joint at the opposite end of the HBE "closes," as shown schematically in Figure 1a. As a result, the net gap opening (due to PT boundary frame expansion) is zero over the full length of the HBE. However, in this configuration, the PT elements require anchorage to the HBE, and while the PT at the opening joint will always contribute to frame recentering, the PT element at the closing joint may or may not, depending on the relationship between the initial PT force provided and the instantaneous frame drift.

A schematic of the NewZ-BREAKSS detail is shown in Figure 1b. In that figure, the connection detail includes an initial gap at the bottom of the HBE flanges, which allows rocking about the HBE top flanges only. As a result, during frame sway, an immediate increase and decrease of PT force occurs at the opening and closing joint locations, respectively. Compared to frames with HBE-to-VBE rocking joints that rock about both flanges (i.e., flange-rocking, or FR, connections), this results in a reduced PT boundary frame stiffness because, for FR connections, a delay in relative HBE-to-VBE gap opening occurs (because both top and bottom HBE flanges are initially in contact with the VBE). For frames detailed with FR connections, this frame type has the benefit that, at incipient initiation of joint gap opening (referred to as the condition when the "decompression-moment" strength of the joint is reached), the joint stiffness is comparable to that of a rigid-moment connection. Additionally, PT boundary frame stiffness softening also occurs with frames detailed with the NewZ-BREAKSS connection due to the relaxation of the PT elements at the closing joints during frame sway. However, scaled and full-scale tests (Dowden and Bruneau, 2014; Dowden et al., 2016) have shown that the absence of a decompression moment and relaxation of the PT elements at the closing joints do not have a detrimental effect on the response of NZ-SC-SPSWs.

Furthermore, the base connection of the VBEs for an SC-SPSW should be detailed such to allow free rotation without the formation of a plastic hinge mechanism (in contrast to conventional SPSWs, where a fixed VBE base connection is typically assumed). If a plastic hinge is able to form at the base of the VBE member, this could limit the self-centering potential of the PT boundary frame. Furthermore, providing a foundation detail free of damage would also use the SC-SPSW to its full potential. As a result, the only needed replaceable elements after a moderate or design level earthquake would be the infill web plates because all other elements are designed to remain essentially elastic.

Figure 1c shows the free-body diagram (FBD) of a NZ-SC-SPSW frame,

where

P_{S1} = PT axial compression force applied to the HBE at the gap opening joint

P_{S2} = PT axial compression force applied to the HBE at the gap closing joint

V_i = externally applied lateral forces at story i due to applied seismic forces

V_{BASE} = total base shear

M_{BASE} = total base overturning moment

ω = diagonal tension yield force developed by the steel web plates

All other terms have been previously defined. The diagonal tension yield forces of the web plate, ω, can be resolved into vertical and horizontal components on the VBE and HBE as provided in Equations 1 and 2 (Sabelli and Bruneau, 2007; Berman and Bruneau, 2008), respectively:

$$\omega_{cx} = F_{yp}t(\sin\alpha)^2 \qquad \omega_{cy} = \frac{F_{yp}t\sin 2\alpha}{2} \tag{1}$$

$$\omega_{bx} = \frac{F_{yp}t\sin 2\alpha}{2} \qquad \omega_{by} = F_{yp}t(\cos\alpha)^2 \tag{2}$$

where

w_{cx} and w_{cy} = horizontal and vertical components, respectively, along the height of the VBEs

w_{bx} and w_{by} = horizontal and vertical components, respectively, along the length of the HBEs

F_{yp} and t = yield stress and thickness of the web plate, respectively

α = angle of inclination of the diagonal tension field from the vertical axis, as typically calculated for SPSWs (AISC, 2010)

Here, forces shown on the FBD are taken assuming that the web plate thickness varies proportional to increasing story shears. Furthermore, the PT boundary frame is designed to essentially remain elastic, and hysteretic energy dissipation is intended to be provided by the infill web plates only.

The total hysteretic response of an NZ-SC-SPSW is provided by the combined elastic response of the PT boundary frame and the inelastic energy dissipation of the infill web plates. The idealized tension-only cyclic hysteretic response assuming a rigid boundary frame and an elastic-perfectly plastic hysteretic model of the infill web plates is shown in Figure 2. In particular, the PT boundary frame stiffness is bilinear elastic, where a reduced secondary PT boundary frame stiffness occurs when the PT at the closing joint becomes fully relaxed; analytical and experimental results (Dowden and Bruneau, 2014) show that this phenomenon has no significant detrimental effect on structural behavior and can be accommodated by design. Furthermore, past research has shown that solid infill web plates do not exhibit a tension-only behavior (as typically assumed for design), but some compression strength of the infill web plate develops due to the deformation of the infill web plate through tension field action (Winkley, 2011; Clayton, 2013; Webster, 2013; Dowden, 2014). However, recent research has also shown that, for dynamic earthquake loadings, this compression effect provides a slight amount of additional energy dissipation and strength but does not affect frame recentering (Dowden and Bruneau, 2014; Dowden et al., 2016).

HBE FREE-BODY-FORCE DIAGRAM

To understand the behavior of an NZ-SC-SPSW system, the moment, shear, and axial force diagrams for the HBE are first developed based on first principles. First, Figure 3 shows the general FBD of HBE and VBE elements located at an intermediate floor level of an SC-SPSW frame once the web plate has fully yielded, where W_{bx1}, W_{bx2} and W_{by1}, W_{by2} are, respectively, the horizontal and vertical force resultants

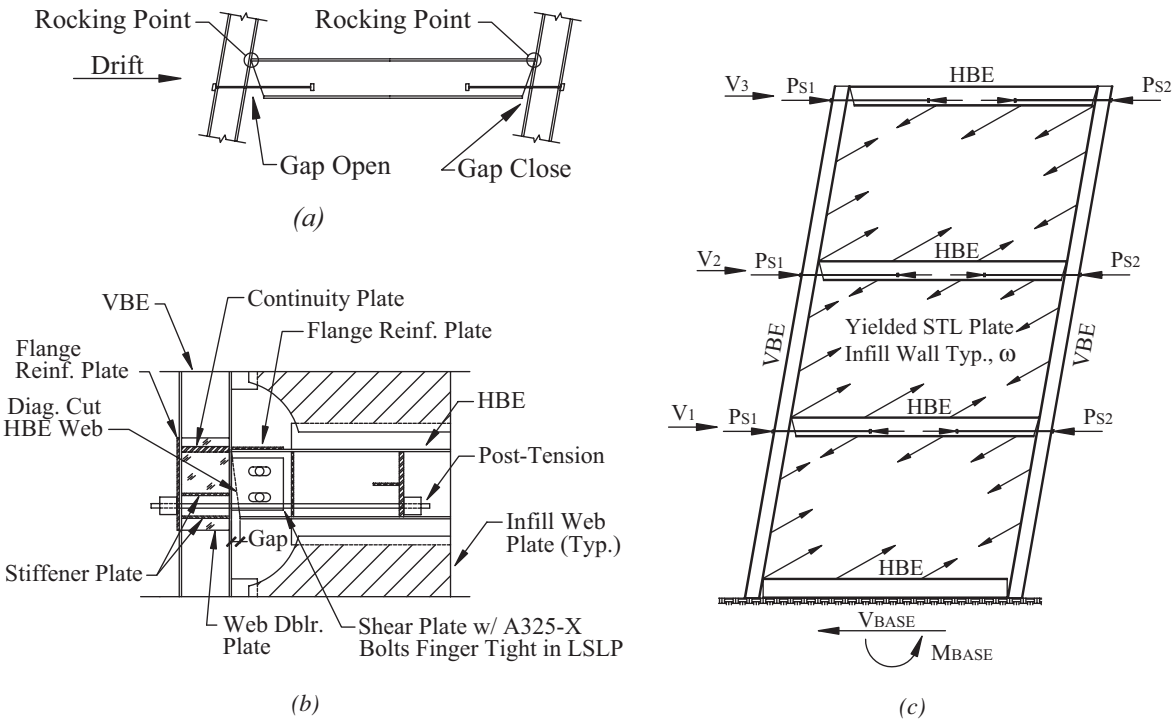

Fig. 1. NZ-SC-SPSW: (a) rocking joints; (b) rocking joint detail; (c) yield mechanism.

along the length of the HBE; W_{cx1}, W_{cx2} and W_{cy1}, W_{cy2} are, respectively, the horizontal and vertical force resultants along the height of the VBE; subscripts 1 and 2, respectively, denote the level below and above the HBE (here assuming that the force components labeled with subscript 1 are larger than subscript 2 associated with a thicker web plate below the HBE than above); H is the story height; and all other terms have been previously defined. Note that the vertical HBE end reactions would have to be resisted by a shear tab connection to the VBE (or equivalent); however, for clarity, the shear tab is not shown in the FBD illustrated.

Next, Figure 4 shows the resultant force FBD of an intermediate HBE for the condition shown in Figure 3 (neglecting gravity forces),

where

V_i = story shear force (as presented in Dowden et al., 2012, for the flange-rocking SC-SPSW) and is assumed to be equally distributed on each side of the frame

W_{bx} = infill web plate horizontal yield force resultant along the length of the HBE

W_{by} = infill web plate vertical yield force resultant along the length of the HBE

$P_{HBE(VBE)}$ = horizontal reaction at the rocking point of the yield force resultant of the infill web plate acting on the VBE (as presented in Sabelli and Bruneau, 2007)

P_s = PT force

P_{sVBE} = horizontal reaction of the post-tension force at the rocking point

R_1 = vertical reaction required for equilibrium of the vertical yield force component of the infill web plate along the HBE, as shown in Figure 5

R_2 = vertical reaction required for equilibrium of the horizontal yield force component of the infill web plate along the HBE, as shown in Figure 6

R_3 = vertical reaction required for equilibrium of the post-tensioned forces acting on the HBE, as shown in Figure 7

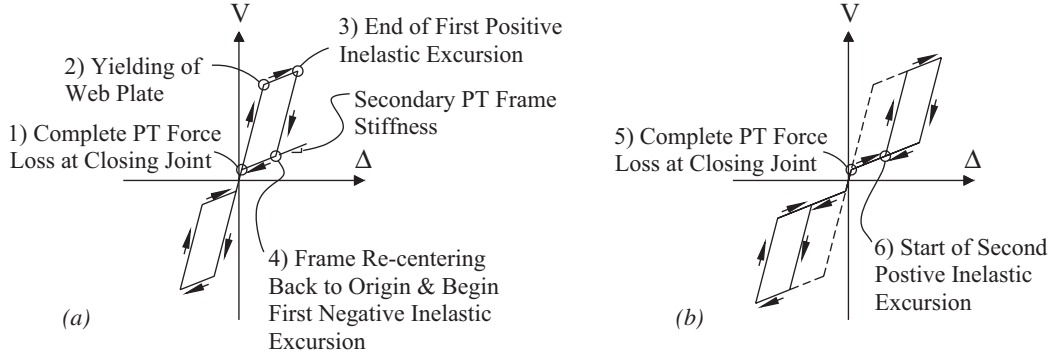

Fig. 2. Idealized hysteretic response of NZ-SC-SPSW: (a) cycle 1; (b) cycle 2.

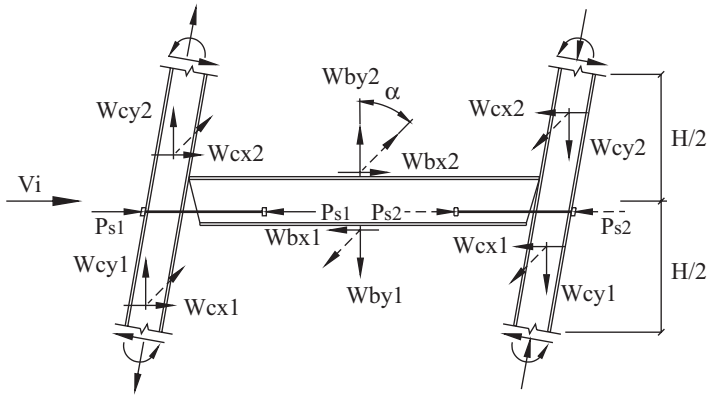

Fig. 3. Resultant force free-body diagram.

y = distance from the HBE neutral axis to the centroid of the PT

d = depth of the HBE

R = length of the radius corner cutout of the infill plate and represents the length of the end segments of the HBEs where the infill web plate is not attached as shown in Figure 1b (and will be further addressed subsequently)

L_1 = length of the HBE that corresponds to the HBE-to-VBE rocking point to the location of the post-tension anchor at the "opening joint" end of the HBE

L_2 = length of the HBE that corresponds to the HBE-to-VBE rocking point to the location of the post-tension anchor at the "closing joint" end of the HBE

L = clear span of the HBE. Also, it is assumed that the boundary frame and PT remain elastic and only the infill web plate yields

Furthermore, in Figure 4, the location of the PT anchor point along the beam will depend on the strain demands of the PT elements at the maximum target drift. The anchor location should be provided such to ensure that the PT strains remain elastic up to that drift demand. Additionally, to clarify the effects of P_{s1} and P_{s2}, each P_s component is composed of two forces: the initial post-tension force P_o, applied prior to drift and the force induced due to post-tension elongation during building drift, ΔP. For the condition shown, from geometry, elongation of post-tension will occur in P_{s1} while "relaxation" of the post-tension element P_{s2} will occur (for reasons described earlier), resulting in the following post-tension forces on the HBE:

$$P_{s1} = P_o + \Delta P = P_o + \frac{A_{PT1}E_{PT1}}{L_{PT1}}\left(\Delta_{drift} - \Delta_{loss}\right) \qquad (3)$$

$$P_{s2} = P_o - \Delta P = P_o - \frac{A_{PT2}E_{PT2}}{L_{PT2}}\left(\Delta_{drift} + \Delta_{loss}\right) \qquad (4)$$

Here, the subscripts 1 and 2 refer to the equation variables located on the HBE segment at the opening and closing joint, respectively, and

L_{PT} = length of the post-tension elements

A_{PT} = area of post-tension

E_{PT} = modulus of elasticity of the post-tension

Δ_{loss} = axial shortening that occurs along the HBE span length between the end of the HBE to the post-tension anchor point locations on the HBE

Δ_{drift} = drift-induced elongation of the post-tension elements at the HBE-to-VBE joint connection producing the incremental force ΔP, calculated as:

$$\Delta_{drift} = \phi_{drift}\left(\frac{d}{2} + y\right) \qquad (5)$$

where ϕ_{drift} is the relative HBE-to-VBE joint rotation in units of radians, and all other terms have been defined previously. From Equations 3 and 4, for a given lateral frame drift, an increase in force P_{s1} results in a simultaneous decrease in force of P_{s2} (and vice versa for lateral drift in the opposite direction). Additionally, if the force ΔP equals P_o, P_{s2} will become fully "relaxed," and this force component will vanish. In other words, for the condition when Δ_{net} (i.e., Δ_{drift} less Δ_{loss}) is equal to or greater than Δ_o, P_{s2} will equal zero. Consequently, the effectiveness of P_{s2} depends on the amount of initial post-tension force P_o as well as the maximum drift reached.

To calculate the loss in post-tension force from HBE axial shortening, using the PT located at the opening joint location to illustrate (as that condition will govern the PT design), equilibrium of axial forces in the post-tension elements requires that the increase in tension forces in the

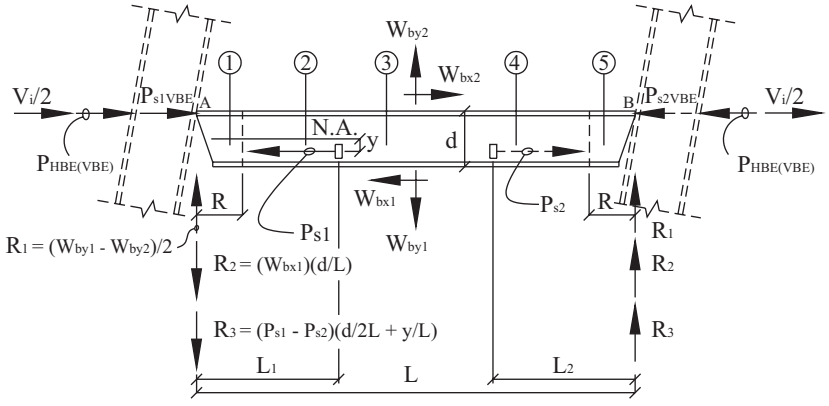

Fig. 4. Complete force-resultant free-body diagram of HBE.

post-tension elements equals the increase in compressive forces on the HBE (Garlock, 2002). For SC-SPSW systems, for equal story force at each end of the HBE (i.e., $V_i/2$ each end of the SC-SPSW frame), the post-tension force losses are attributed to the HBE axial shortening under the axial compression force from the VBE and the axial compression force due to the post-tension elongation during lateral drift (with the simplified assumption of rigid VBEs). Furthermore, the PT force contributing to HBE axial shortening along the length of the HBEs between PT anchor points, is a smaller fractional value of the tension force in the PT elements; a schematic of this is illustrated in Figure 8. The calculation of PT force losses due to HBE axial shortening then follows:

$$\Delta_{loss} = \frac{(P_{PT} \times SF) L_1}{A_{HBE} E_{HBE}} + \frac{P_{HBE(VBE)} L_1}{A_{HBE} E_{HBE}} \tag{6}$$

where

SF = some scale factor (presented subsequently)

P_{PT} = force in the post-tension element (i.e., P_{s1})

A_{HBE} = cross-section area of the HBE

E_{HBE} = modulus of elasticity of the HBE

All other terms have been previously defined. Next, solving Equation 6 for P_{PT} leads to the following:

$$P_{PT} = \frac{1}{SF}\left(\frac{A_{HBE} E_{HBE}}{L_1} \Delta_{loss} - P_{HBE(VBE)}\right) \tag{7}$$

Correspondingly, the net effective axial tension force in the post-tension elements is the elongation due to drift minus the axial shortening of the HBE that occurs along the length of the post-tension elements and is calculated as follows:

$$P_{PT} = \left(\frac{A_{PT} E_{PT}}{L_{PT}}\right)\left(\Delta_{drift} - \Delta_{loss}\right) = k_{PT}\left(\Delta_{drift} - \Delta_{loss}\right) \tag{8}$$

Next, equating Equations 7 and 8, then solving for Δ_{loss}, leads to the amount of post-tension relaxation that should be considered for design and is calculated as:

$$\Delta_{loss} = \frac{P_{HBE(VBE)}}{k^*_{PT} + \dfrac{A_{HBE} E_{HBE}}{L_1}} + \left(\frac{k^*_{PT}}{k^*_{PT} + \dfrac{A_{HBE} E_{HBE}}{L_1}}\right)\Delta_{drift} \tag{9}$$

where the SF and the post-tension axial stiffness terms have been combined such that:

$$k^*_{PT} = \left(\frac{A_{PT} E_{PT}}{L_{PT}}\right) SF = (k_{PT})(SF) \tag{10}$$

and, from Figure 8, the scale factor can be approximated as:

$$SF = \left(\frac{h - y}{h + 0.5d}\right) \tag{11}$$

where

h = distance from the bottom of the VBE to the centroid of the HBE

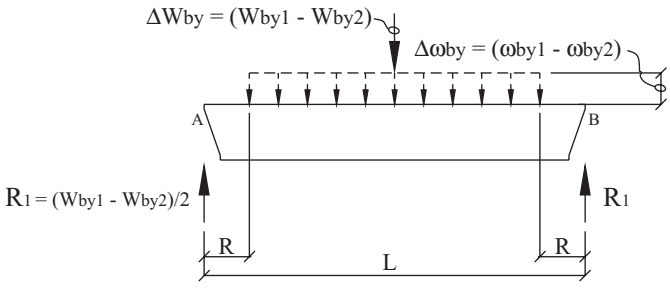

Fig. 5. Free-body diagram vertical component.

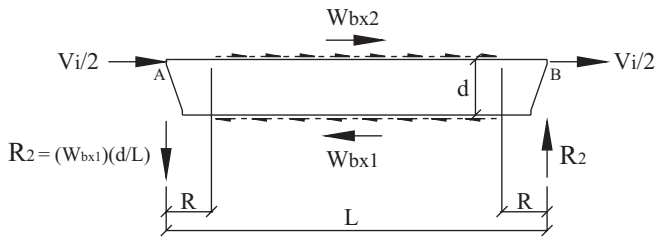

Fig. 6. Partial free-body diagram horizontal component.

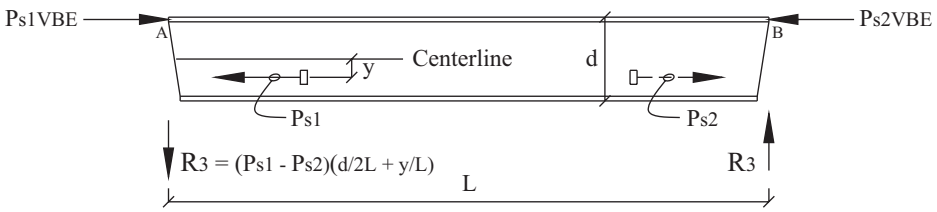

Fig. 7. Free-body diagram post-tension forces.

y = distance of the PT from the HBE centroid

d = depth of the HBE

Finally, the resulting equations for P_s, for the rightward drift condition shown in Figure 1c, which includes losses due to HBE axial shortening, is obtained by substituting Equation 9 into Equations 3 and 4, leading to:

$$P_{s1} = P_o + \left(\frac{k_{b1}k_{PT}^*}{k_{b1}+k_{PT}^*}\right)\Delta_{drift} - \frac{k_{PT}^*}{k_{b1}+k_{PT}^*}P_{HBE(VBE)} \quad (12)$$

$$P_{s2} = P_o - \left(\frac{k_{b2}k_{PT}^* + 2\left(k_{PT}^*\right)^2}{k_{b2}+k_{PT}^*}\right)\Delta_{drift} - \frac{k_{PT}^*}{k_{b2}+k_{PT}^*}P_{HBE(VBE)} \quad (13)$$

where, in Equations 12 and 13, k_{b1} and k_{b2} are the HBE axial stiffness along length L_1 and L_2, respectively.

Development of HBE Moments

The moment distribution to be used in the design of an HBE incorporating self-centering components can be determined from the free-body diagram of Figure 4. As indicated in that figure, five locations along the HBE are considered: the two segments of HBE where the infill web plate is cut out (thus not connected to the HBE flange), the two segments of the HBE between the infill web plate corner cutout and the post-tension anchor point, and the segment of the HBE between the post-tension anchor points along the length of the HBE. These locations, for the purpose of presentation, are designated as zone 1, zone 2, zone 3, zone 4, and zone 5. The FBD for zone 1 is shown in Figure 9.

Furthermore, for illustration purposes, in Figure 9 the horizontal compression reaction at the HBE-to-VBE flange rocking point and vertical HBE end reaction (components shown in Figure 4) are combined into a single variable C and R_A, respectively. The determination of the HBE flexural strength demand then follows by taking moment equilibrium at the HBE section cut 1; the moment relationship in terms of force resultants is:

$$M_1 = R_a x + C\left(\frac{d}{2}\right) \quad (14)$$

Substituting Equations 1 and 2, along with the equivalent force per unit length quantities for the resultant forces defined earlier, into Equation 14, the resulting moment relationship expressed in terms of the infill web plate yield forces per unit length along the HBE along zone 1 is:

$$\begin{aligned} M_1 = {} & P_{s1(VBE)}\left(\frac{d}{2}\right) - P_{s1}\left(\frac{d}{2L}x + \frac{y}{L}x\right) + P_{s2}\left(\frac{y}{L}x + \frac{d}{2L}x\right) \\ & + \left(\omega_{by1} - \omega_{by2}\right)\left(\frac{L}{2}x - Rx\right) \\ & + \left(\omega_{cx1} + \omega_{cx2}\right)\left(\frac{dh}{4} - \frac{d^2}{4} - \frac{dR}{2}\right) \\ & + \omega_{bx1}\left(\frac{2dR}{L}x - dx\right) + V_i\left(\frac{d}{4}\right) \end{aligned} \quad (15)$$

Similarly, by moment equilibrium at the remaining sections 2 through 5, the moment distribution along these zones is:

$$\begin{aligned} M_2 = {} & P_{s1(VBE)}\left(\frac{d}{2}\right) - P_{s1}\left(\frac{d}{2L}x + \frac{y}{L}x\right) + P_{s2}\left(\frac{y}{L}x + \frac{d}{2L}x\right) \\ & + \left(\omega_{by1} - \omega_{by2}\right)\left(\frac{L}{2}x - \frac{x^2}{2} - \frac{R^2}{2}\right) + \left(\omega_{cx1} + \omega_{cx2}\right)\left(\frac{dh}{4} - \frac{d^2}{4} - \frac{dR}{2}\right) \\ & + \omega_{bx1}\left(\frac{2dR}{L}x - \frac{d}{2}x - \frac{dR}{2}\right) + \omega_{bx2}\left(\frac{d}{2}x - \frac{dR}{2}\right) + V_i\left(\frac{d}{4}\right) \end{aligned} \quad (16)$$

$$\begin{aligned} M_3 = {} & P_{s1(VBE)}\left(\frac{d}{2}\right) + P_{s1}\left(y - \frac{d}{2L}x - \frac{y}{L}x\right) + P_{s2}\left(\frac{y}{L}x + \frac{d}{2L}x\right) \\ & + \left(\omega_{by1} - \omega_{by2}\right)\left(\frac{L}{2}x - \frac{x^2}{2} - \frac{R^2}{2}\right) + \left(\omega_{cx1} + \omega_{cx2}\right)\left(\frac{dh}{4} - \frac{d^2}{4} - \frac{dR}{2}\right) \\ & + \omega_{bx1}\left(\frac{2dR}{L}x - \frac{d}{2}x - \frac{dR}{2}\right) + \omega_{bx2}\left(\frac{d}{2}x - \frac{dR}{2}\right) + V_i\left(\frac{d}{4}\right) \end{aligned} \quad (17)$$

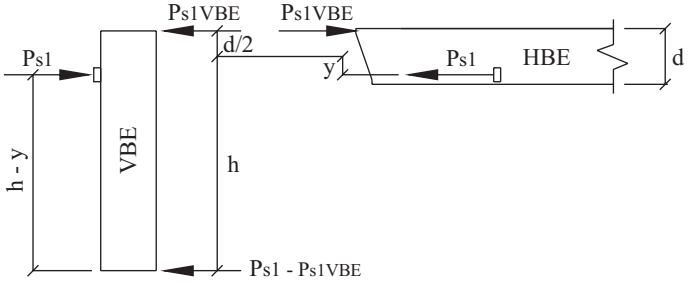

Fig. 8. Reduced post-tension force on HBE.

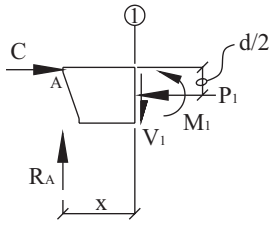

Fig. 9. Free-body diagram along zone 1.

$$M_4 = P_{s1VBE}\left(\frac{d}{2}\right) + P_{s1}\left(y - \frac{d}{2L}x - \frac{y}{L}x\right) + P_{s2}\left(\frac{y}{L}x + \frac{d}{2L}x - y\right) + \left(\omega_{by1} - \omega_{by2}\right)\left(\frac{L}{2}x - \frac{x^2}{2} - \frac{R^2}{2}\right) + \left(\omega_{cx1} + \omega_{cx2}\right)\left(\frac{dh}{4} - \frac{d^2}{4} - \frac{dR}{2}\right) + \omega_{bx1}\left(\frac{2dR}{L}x - \frac{d}{2}x - \frac{dR}{2}\right) + \omega_{bx2}\left(\frac{d}{2}x - \frac{dR}{2}\right) + V_i\left(\frac{d}{4}\right) \quad (18)$$

$$M_5 = P_{s1(VBE)}\left(\frac{d}{2}\right) + P_{s1}\left(y - \frac{d}{2L}x - \frac{y}{L}x\right) + P_{s2}\left(\frac{y}{L}x + \frac{d}{2L}x - y\right) + \left(\omega_{by1} - \omega_{by2}\right)\left(\frac{L^2}{2} + Rx - \frac{L}{2}x - LR\right) + \left(\omega_{cx1} + \omega_{cx2}\right)\left(\frac{dh}{4} - \frac{d^2}{4} - \frac{dR}{2}\right) + \omega_{bx1}\left(\frac{2dR}{L}x - dx + \frac{dL}{2} - dR\right) + \omega_{bx2}\left(\frac{dL}{2} - dR\right) + V_i\left(\frac{d}{4}\right) \quad (19)$$

Development of HBE Shear and Axial Forces

The shear distribution to be used in the design of an HBE can be determined using the same FBD and procedure as presented earlier, which then leads to:

$$V_1 = R_a = \frac{\left(\omega_{by1} - \omega_{by2}\right)(L - 2R)}{2} - \frac{(\omega_{bx1})(L - 2R)}{L}d - (P_{s1} - P_{s2})\left(\frac{d}{2L} + \frac{y}{L}\right) \quad (20)$$

$$V_2 = V_3 = V_4 = R_a - \left(\omega_{by1} - \omega_{by2}\right)(x - R) \quad (21)$$

$$V_5 = R_a - \left(\omega_{by1} - \omega_{by2}\right)(L - 2R) \quad (22)$$

Similarly, for axial forces over each of the five zones:

$$P_1 = C = \frac{\left(\omega_{bx1} - \omega_{bx2}\right)(L - 2R)}{2} + \left(\omega_{cx1} + \omega_{cx1}\right)\left(\frac{h}{2} - \frac{d}{2} - R\right) + P_{s1(VBE)} \quad (23)$$

$$P_2 = C - \left(\omega_{bx1} - \omega_{bx2}\right)(x - R) \quad (24)$$

$$P_3 = C - \left(\omega_{bx1} - \omega_{bx2}\right)(x - R) - \left(P_{s1} + P_{s2}\right) \quad (25)$$

$$P_4 = C - \left(\omega_{bx1} - \omega_{bx2}\right)(x - R) \quad (26)$$

$$P_5 = C - \left(\omega_{bx1} - \omega_{bx2}\right)(L - 2R) \quad (27)$$

Note that the development of the HBE moment, shear, and axial force formulations presented are based on a capacity design approach where the web plates have fully yielded. Consideration of PT force losses due to HBE elastic axial shortening has been considered. However, some vertical deflection of the HBE will occur due to the vertical component of the infill web plate tension forces pulling on the HBE. This results in HBE-to-VBE rotational components that will have an influence on the actual joint gap opening/closing, thus affecting the axial elongation response of the PT elements. However, this contribution of joint gap response can be neglected, without significant loss in accuracy, as will be observed in the following section. But to precisely account for this effect, a nonlinear pushover analysis would be needed. Furthermore, the derivations of the closed-form equations presented for the HBE strength demands assume rigid VBEs. In particular, the contribution of the flexibility of the VBEs contributing to PT force losses is neglected. Consideration of VBE flexibility can be included in a nonlinear pushover analysis once the numerical model is established (for which the equations presented earlier can be used to facilitate the initial design). Finally, as shown in Figure 4, Equations 14 through 27 were derived with the assumption that the story force (i.e., V_i) is equally distributed on each side of the frame. For the condition when the story force is delivered to only one side of the frame, Figure 6 would be modified to show V_i acting at location A and $V_i = 0$ at location B in that figure (note that the value of the reaction R_2 shown in that figure would remain unchanged). This would have the effect of increasing the HBE moment and axial force demand proportionally to V_i versus $V_i/2$.

NUMERICAL MODEL COMPARISON

The formulations describing the distribution of moment, shear and axial forces developed earlier were compared to results from nonlinear pushover analysis conducted using SAP2000 (CSI, 2009). Additionally, numerical modeling in OpenSees (Mazzoni et al., 2009) is also presented subsequently for reference. The example SPSW used for this purpose consisted of a single-bay, single-story frame with a bay width of 20 feet and story height of 10 feet. The SPSW web plate consisted of a 16-gauge infill light-gauge plate. A total of eight ½-in.-diameter, Grade 270 ksi steel monostrands were provided at each end of the HBE with a distance of 6 in. below the neutral axis of the HBE to the centroid of the tendons. An initial post-tensioning force of approximately 20% of the yield strength of the PT was provided. The depth of the HBE was taken to be 18 in., corresponding to a W18 beam.

Furthermore, a strip model was used for the infill web plate (Sabelli and Bruneau, 2007), as shown in Figure 10. Accordingly, because the hysteretic behavior of SPSWs relies on yielding of the infill web plate through diagonal tension field action, the infill web plate was conservatively

modeled by using a series of tension-only strips. Each of the strips was assigned an axial plastic hinge model to account for nonlinear hysteretic behavior. The PT boundary frame and post-tension elements were designed to remain elastic.

For the rocking connection in SAP2000, a rigid-beam element was used as a link to model the post-tension anchor points to the HBE to capture the applied moment during rocking motion about the HBE centerline. Joint constraints in the translational vertical global degrees-of-freedom (DOF) and in-plane (HBE strong axis bending) rotational DOF were provided at key nodes. For the case of modeling in OpenSees, rigid-link beams are used in lieu of joint constraints (with the exception of modeling the HBE to VBE shear transfer). The connection models for use in SAP2000 and OpenSees are shown in Figure 11.

For the current example, the designed SPSW is used to avoid abstract complexities in keeping the problem parametric. Additionally, the boundary frame members are assumed rigid here such that PT force losses due to HBE axial shortening can be ignored because this has a negligible impact on the results and keeps the conceptual illustration manageable. The formulations developed earlier are applicable regardless of whether PT force losses are considered. Only the P_{s1} and P_{s2} terms in the equations are affected and would need to include the PT force losses as presented in Equations 12 and 13. Figure 12 provides comparisons of the moment, shear and axial force distributions along the length of the HBE using the formulations developed earlier to those with the numerical model of the SAP2000 analysis for a rightward 3% drift condition. Note that because the SAP2000 model uses a finite number of strips to represent the infill web plate, the shear and axial force diagrams obtained from the

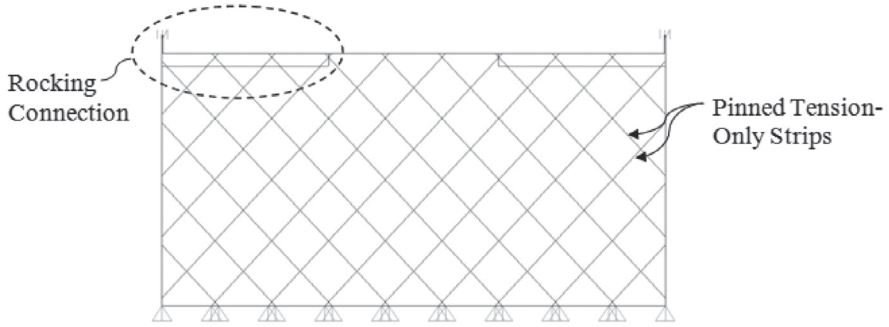

Fig. 10. NZ-SC-SPSW model.

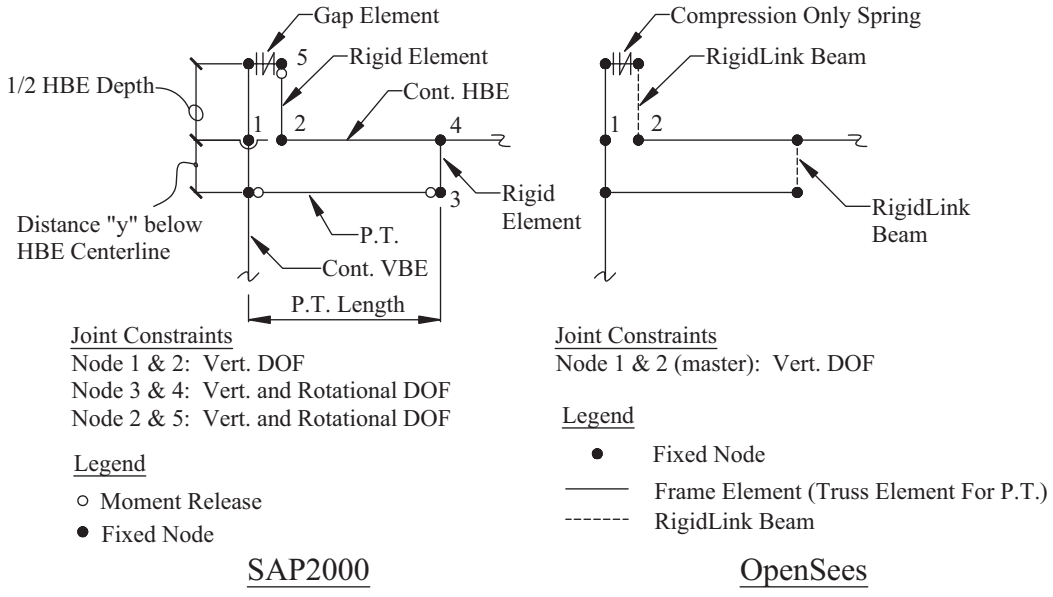

Fig. 11. NewZ-BREAKSS connection model.

SAP2000 analysis are stepped as compared to the continuous force diagrams using the analytical formulations.

Furthermore, the analytical formulations are compared to two different SAP2000 curves labeled "actual" and "idealized," where, for the condition of a rigid HBE, the idealized curve matches the analytical one almost perfectly for the moment and shear diagrams. The difference between the two different numerical models is that the idealized curves assume a pinned connection at the HBE-to-VBE flange contact rocking point. This represents the idealized condition assumed in the development of the equations presented previously. The actual model uses the compression-only element shown in Figure 11, which models more accurately the real condition of the joint detail. To further clarify, the preceding derivations assume that the effects on the post-tension (i.e., terms P_{s1} and P_{s2}) are exactly equal; which is essentially true for the rigid HBE condition if the HBE is pin connected to the VBEs. However, with the use of the compression-only element, some differences arise in response because now the compression force at the closing joint can be reduced (from the global effects captured by the numerical frame model that is not considered in the analytical formulations), leading to small differences in the kinematics governing the axial tension in the post-tension elements. It is also observed that on the SAP2000 moment and axial diagram curves, the post-tension force at the closing joint has not fully relaxed because there is a vertical step in the response curves. The results from the SAP2000 analysis and the corresponding analytical formulations compare reasonably along the full length of the HBE.

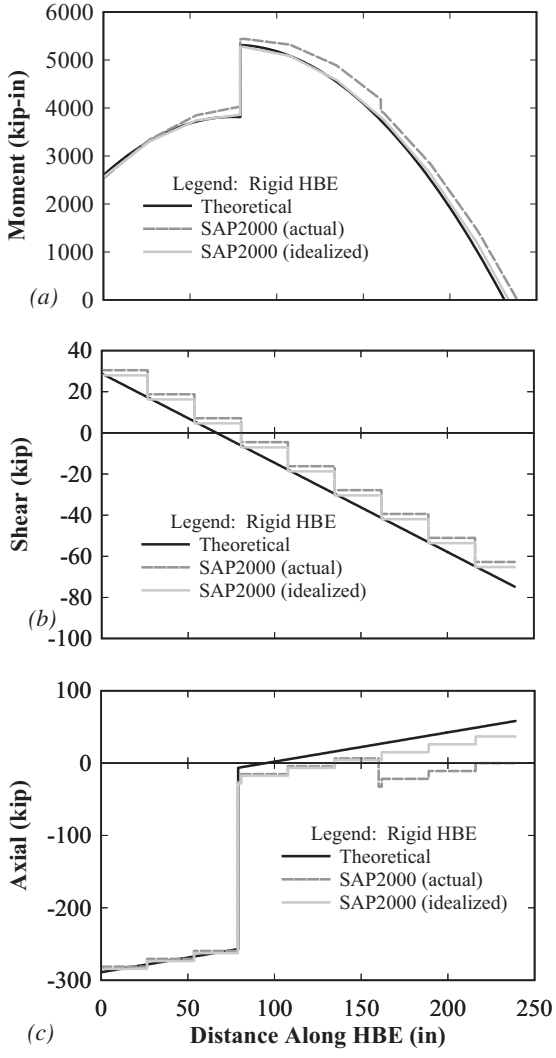

Fig. 12. SAP2000 nonlinear pushover analysis comparison.

To provide some comparison of numerical results using SAP2000 versus OpenSees, a nonlinear cyclic pushover analysis was conducted for the one-third-scale, single-bay, three-story NZ-SC-SPSW test frame investigated by Dowden and Bruneau (2014). The design parameters of the frame along with the corresponding numerical model are shown in Figure 13. Material properties consisted of ASTM A992, A416 and A1008 for the boundary frame, ½-in.-diameter PT monostrands, and infill web plate members, respectively. The VBE column bases were detailed with a clevis-and-pin base to allow free rotation, and all anchor connections to the foundation were bolted. To model the nonlinear hysteretic response of the infill web plates, nonlinear axial hinge assignments were used in the numerical model based on results from coupon testing. Additionally, an initial post-tensioning force of approximately 20% of the PT yield strength was used. The comparison of the base shear versus roof drift response obtained using the programs SAP2000 and OpenSees is shown in Figure 14; the results are practically identical.

POST-TENSION FORCE EFFECTS ON GLOBAL FRAME RESPONSE

A general base shear versus roof displacement response for the NZ-SC-SPSW was presented in Figure 2, where the contribution of the PT boundary frame response is observed to be bilinear elastic. To investigate the effects of various PT parameters on the response of the boundary frame, the variation in frame response when changing the initial PT force (T_o) and the quantity of PT strands (A_{PT}) is presented for the frame shown in Figure 13. In the following figures, response curves for the condition labeled 1xT_o and 1xA_{PT} correspond to the PT design parameters used in the test specimen (as a reference point). In this investigation, note that (1) all other design parameters (i.e., member sections, distance of PT eccentricity to the rocking point, etc.) remain the same because changing those would require other design changes, and (2) practical considerations of construction tolerances

are not considered because only the consequences of relative change in response are of interest here. Furthermore, this investigation is only made for the PT boundary frame, with the understanding that the total response is a superposition of the effects of the PT boundary frame and the infill web plate.

The variation in response due to T_o as the parametric variable is presented in Figure 15a, with A_{PT} held constant. Note that if significant PT yield occurs for a given T_o, no additional parametric curves are presented for that frame because only the elastic response of the boundary frame is of interest here (i.e., no yielding of PT elements, which would alter the frame response). It is observed that with T_o = 0 kips (i.e., 0xT_o), the frame response moves along a single elastic curve; thus, the presence of an initial PT force is what defines the bilinear frame response. Of particular interest, the location of the transition point between the initial and secondary stiffnesses is defined by the magnitude of T_o (as shown in Figure 2). More specifically, increasing the initial applied PT force results in (1) a positive shift of that transition point along the horizontal axis, resulting in an increase of the initial stiffness range of response that has the largest stiffness along the bilinear response curve, and (2) a positive shift of that transition point along the vertical axis, contributing more strength to the hysteretic response of the entire system.

The variation in response due to A_{PT} is presented in Figure 15b, with T_o held constant. In doing so, the quantity of PT strands (or rods) affects the stiffness (i.e., slopes) of the response curves (as would be expected). Furthermore, as A_{PT} increases, the effects of the secondary PT boundary frame stiffness (i.e., condition when T_o reduces to zero) become more dominant over the initial stiffness. This is due to a reduction in T_o in each corresponding PT strand (i.e., T_o remains constant; however, T_o per strand decreases proportional to the increase in A_{PT}). As a consequence, not only does increasing A_{PT} affect both initial and secondary stiffness of the PT boundary frame response curves, but increasing A_{PT} also shifts the transition point between the initial and secondary frame stiffness toward the axis origin (whereas increasing T_o shifts the transition point away). In comparison to Figure 15a, a significant increase in stiffness can be achieved without concern of yielding the PT elements for a target drift; however, it is at the expense of larger strength demands on the boundary frame than consideration of T_o alone.

INFILL WEB PLATE STRAINS EFFECTS DUE TO HBE-TO-VBE GAP OPENING

As presented earlier, radius corner cutouts are provided at the infill web plate corner locations. The primary purpose of this detail is to remove the portion of the infill web plate at the corner locations that would otherwise be subjected to excessive tensile strains during lateral frame drift due to the opening of the rocking joint (as schematically shown in Figure 16).

To determine the appropriate value of the radius corner cutout to use in design, a review of the kinematics of the joint detail under frame sway is necessary and is performed next,

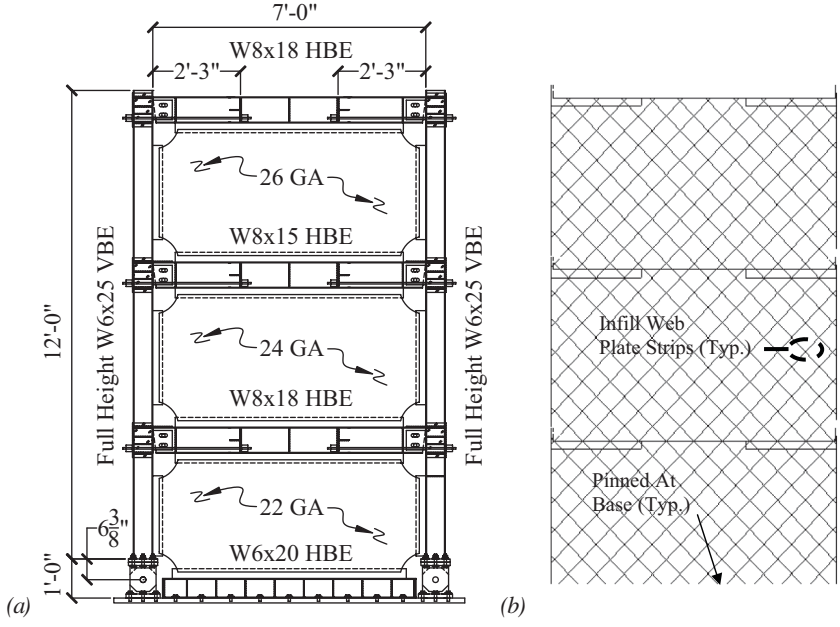

Fig. 13. (a) Frame parameters; (b) numerical model.

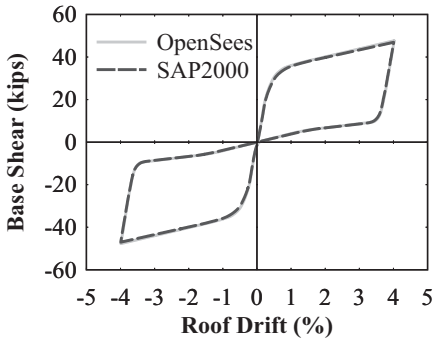

Fig. 14. Comparison of SAP2000 and OpenSees.

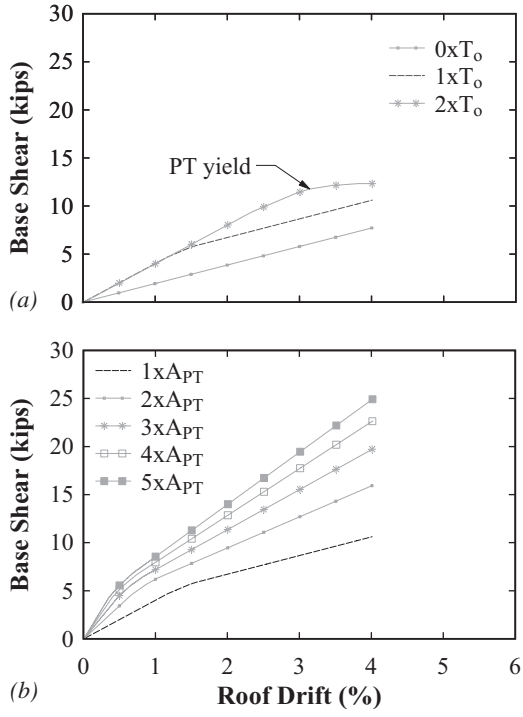

Fig. 15. PT boundary frame: (a) T_o variable; (b) A_{PT} variable.

based on small-angle theory. Figure 17 shows the geometry and parameters necessary to establish the kinematic relationships governing the infill web plate tensile strains when also including the HBE-to-VBE gap openings in the calculation of strains.

In Figure 17, R is the radius length of the corner cutout, L is the length of the adjacent infill web strip to the corner (shown idealized), α is the angle of inclination of the tension field to the vertical axis, ΔR are differential lengths dependent on the value α, Δgap is the HBE-to-VBE gap opening, d is the depth of the HBE, and γ is the gap opening rotation. To determine the total cumulative axial tensile strain of the strip adjacent to the tip of the radius cutout, the following relationships are established from geometry. The length L is obtained from the initial condition geometry (triangle 1-2-3) as:

$$L = \frac{R + \Delta R_1}{\sin\alpha} \tag{28}$$

Next, the axial tensile deformation of the infill web strip due to gap opening is (using the geometry of triangle 5-6-7):

$$\delta = \left(\Delta_{gap}\right)\cos(90 - \alpha) \tag{29}$$

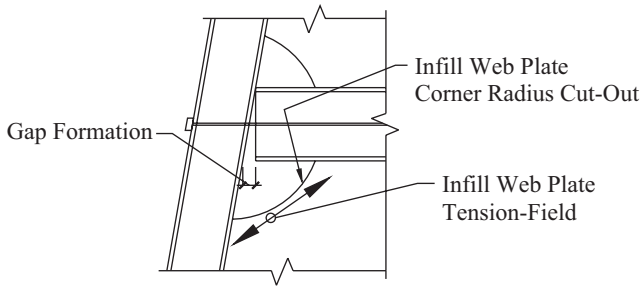

Fig. 16. HBE-to-VBE joint gap formation.

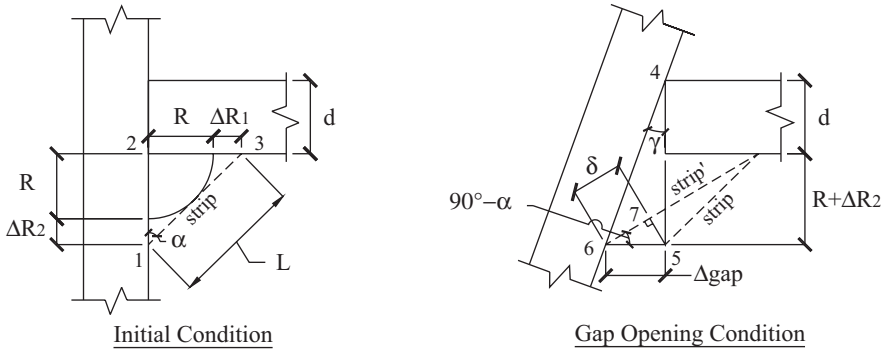

Fig. 17. HBE-to-VBE rocking joint kinematics.

The gap opening can then be calculated (using geometry of triangle 4-5-6) as:

$$\Delta_{gap} = \gamma\left(d + R + \Delta R_2\right) \tag{30}$$

It is also observed that (using the geometry of triangle 1-2-3):

$$\tan\alpha = \frac{\left(R + \Delta R_1\right)}{\left(R + \Delta R_2\right)} \tag{31}$$

Next, the differential term ΔR_2 is established (for reasons to be made clear subsequently). To proceed, Figure 18 shows the additional information needed to determine this quantity.

It then follows, using triangle 1 in Figure 18 and the sine double-angle identity, that the parameter $x1$ is:

$$x1 = R\sin(90 - \alpha) = R\cos\alpha \tag{32}$$

Furthermore, from the same triangle 1, the term $y1$ can be determined as follows:

$$y1 = R\sin\alpha \tag{33}$$

Next, from the geometry of triangle 2 in Figure 18, substituting Equation 32 for $x1$ and solving for $y2$ leads to:

$$y2 = \frac{R\cos\alpha}{\tan\alpha} \tag{34}$$

Furthermore, in Figure 18 it is observed that:

$$\Delta R_2 + R = y1 + y2 \tag{35}$$

which, substituting Equations 33 and 34 for $y1$ and $y2$, respectively, in Equation 35 and solving for ΔR_2, leads to:

$$\Delta R_2 = y1 + y2 - R = R\sin\alpha + \frac{R\cos\alpha}{\tan\alpha} - R \tag{36}$$

The resulting infill web plate tensile strain can then be expressed as:

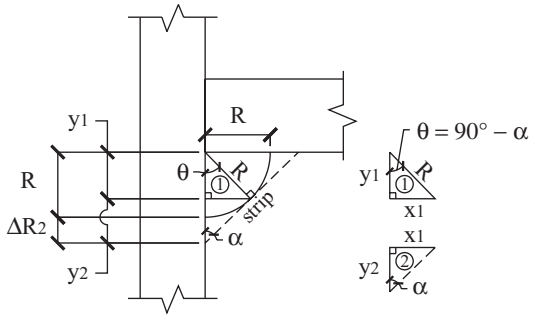

Fig. 18. Infill web plate corner cutout dimensions.

$$\varepsilon = \frac{\delta}{L} = \frac{\Delta_{gap}\sin\alpha}{\left(\dfrac{R + \Delta R_1}{\sin\alpha}\right)} \tag{37}$$

Substituting the terms for Δ_{gap} and $(R + \Delta R_1)$ using Equations 30 and 31 into Equation 37, it then follows that:

$$\varepsilon = \frac{\gamma\left(d + R + \Delta R_2\right)\sin^2\alpha}{\left(R + \Delta R_2\right)\tan\alpha} \tag{38}$$

Next, substituting ΔR_2 from Equation 36 and simplifying leads to:

$$\varepsilon = \frac{\gamma\left(d + \dfrac{R\cos\alpha}{\tan\alpha} + R\sin\alpha\right)\left(\sin\alpha\cos\alpha\right)}{R\left(\dfrac{\cos\alpha}{\tan\alpha} + \sin\alpha\right)} \tag{39}$$

Finally, Equation 39 can be further simplified by the substitution of the sine double-angle identity, which then results in the following expression:

$$\varepsilon_{Total} = \frac{\gamma\sin 2\alpha}{2}\left(\frac{\dfrac{d}{R}\tan\alpha + \cos\alpha + \sin\alpha\tan\alpha}{\cos\alpha + \sin\alpha\tan\alpha}\right) \tag{40}$$

Equation 40 represents the total tensile strain on the infill web plate for HBE-to-VBE rocking connections at a distance R away from the HBE-to-VBE flange rocking point. To further clarify the effects of Equation 40, for the case of $\alpha = 45$ degrees, Equation 40 results in the following:

$$\varepsilon_{Total} = Component1 + Component2 = \frac{\gamma d\sqrt{2}}{4R} + \frac{\gamma}{2} \tag{41}$$

where, in Equation 41, *Component*1 is the contribution of tensile strain from the gap opening and *Component*2 is the contribution from lateral frame drift (i.e., a rigid panel sway mechanism). To further illustrate, Figure 19a shows the axial strain demand for several different lateral drift conditions. From the results shown, the closer the infill web plate is to the corner (corresponding to a smaller R), the larger the strain demands. In particular, if $R = 0$, the theoretical strain is infinite.

Furthermore, Figure 19b shows the total axial tensile strain, together with the strain corresponding to each component, for a 2% drift condition. From the results shown, the concentration of strains in the infill web plate due to the use of a rocking connection is a localized phenomenon, with values approaching those for the rigid-panel sway mechanism away from the rocking connection gap opening. Note that in the examples presented, the gap rotation was assumed to be equal to the drift rotation, which assumes rigid sway

behavior as an approximation; a more exact joint rotation could be obtained from a rigorous frame analysis. Nonetheless, the preceding equations provide an approach to select the radius of the corner cutouts. As an example, SC-SPSW test specimens investigated by Dowden and Bruneau (2014) were detailed with an R/d ratio of approximately 1. For this condition shown in Figure 19a (i.e., $\alpha = 45$ degrees), for the case of 2% roof drift, Equation 40 predicts a maximum theoretical infill web plate tensile strain of approximately 1.7%. In particular, from observations of the experimental results presented by Dowden and Bruneau (2014), infill web plate separation from the boundary frame started to develop at approximately 2% roof drift (a drift magnitude expected for a design level earthquake), propagating from the plate corners. This provides some indication that the R/d ratio of 1.0 used in the HBE-to-VBE joint detail for the infill web plate corners performed reasonably well to delay the effects of initial web plate tearing from the boundary frame.

Finally, note that the preceding strain equations are applicable to any HBE-to-VBE joint rocking configuration because only the distance from the rocking contact point to the HBE flange needs to be modified in the equations presented. For example, for a centerline-rocking frame (Dowden and Bruneau, 2014), $d/2$ (half-depth of the HBE) would be used in lieu of d in the equations, and for the NewZ-BREAKSS and flange-rocking (Clayton et al., 2012; Dowden et al., 2012) connections, no changes to the equations presented are required because both connections follow the same kinematics at the opening joints when the HBE-to-VBE gap is present.

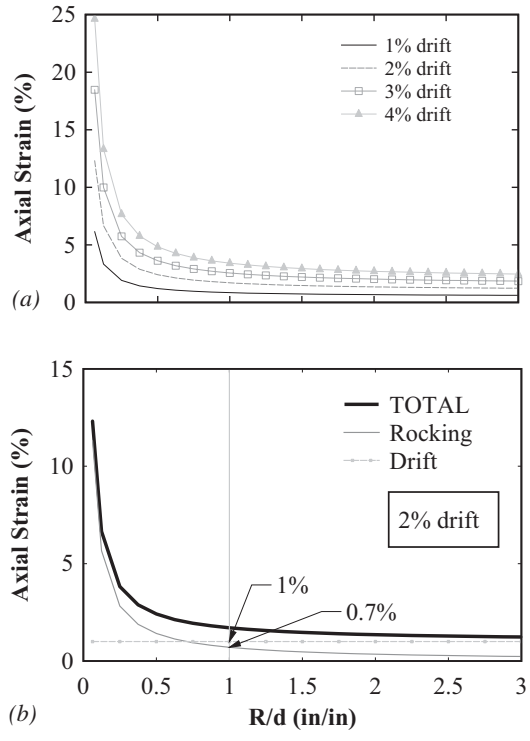

Fig. 19. Corner infill web plate: (a) strain demands; (b) strain components.

PT BOUNDARY FRAME EXPANSION: A DERIVATION OF UNRESTRAINED BEAM-GROWTH

A widespread concern with the practical implementation of self-centering frames with HBE-to-VBE rocking connections is the issue of "beam-growth" (i.e., frame beam elongation or PT boundary frame expansion). This phenomenon occurs because the joint opening at each end of the beam (which is required in order to induce PT tensile strains for recentering) manifests itself as an apparent increase in horizontal length of the beams (although physically the beam length remains essentially the same). This has the undesired effect of the beams pushing outward against the columns by the amount of the gap openings at the beam-to-column rocking joints. As a consequence, strength demands on the columns are increased (i.e., columns must flexurally deform to accommodate the beam growth) as well as strain compatibility issues of the diaphragm connection to the beams arise (i.e., the diaphragm must slip/tear or deform to accommodate the beam growth).

Large-scale experimental investigation (Dowden and Bruneau, 2014; Dowden et al., 2016) of a single-bay, two-story NZ-SC-SPSW showed that even though the NewZ-BREAKSS rocking connection was proposed to eliminate beam-growth effects, a small but observable amount of beam growth does develop for the NewZ-BREAKSS rocking connection, contrary to what was initially assumed (insignificant compared to connections rocking about their top and bottom HBE flanges but, nonetheless, required to be understood). As a result of this observation, closer scrutiny of the kinematics of this connection has lead to a better understanding of beam growth; equations that could be used to inform design and optional modifications to the NewZ-BREAKSS detail to completely eliminate beam-growth effects are presented.

The analytical relationship for unrestrained beam growth can be obtained by reviewing the free-body diagram shown in Figure 20 and observing that, for the rightward drift shown in that figure, the rotation at the left and right VBE differ by an incremental amount $\Delta\theta$ as a result of beam growth, where the additional parameters in the figure are defined as follows:

θ = VBE rotation at a known drift level

$h1$ = height from the VBE base to the bottom most rocking contact point of interest

L_{HBE} = length of the HBE

$\Delta L1$ = horizontal length due to drift rotation θ

$\Delta L2$ = horizontal length due to the drift gap opening θ at the opening joint

d_{VBE} = depth of the VBE, which is shown in a position before and after rotation of the VBE

$D1$ = flange rocking depth rotation lever arm

ΔV, $\Delta H1$ and $\Delta H2$ = incremental dimensions dependent on the VBE base rotation at the VBE location effected by $\theta + \Delta\theta$

x = length parameter used to define $\theta + \Delta\theta$ for subsequent derivation

From the parameters defined, the quantity $\Delta H2$ is the key parameter needed to define the real relationship of unrestrained beam growth (for the conditions noted later) and represents the change in length reduction in the bottom of the parallelogram (indicated in Figures 20 and 21) that takes into account the VBE base rotation $\theta + \Delta\theta$.

Note that the subsequent derivation is based on using a two-story frame with NewZ-BREAKSS rocking connections for illustration purposes. However, the formulations can be applied to a frame of any height and any rocking connection because (1) the height just above ground level controls the kinematic equations, and (2) the parameter associated with the type of rocking connection affecting beam growth is only dependent on the depth of the rocking point rotation lever arm. Furthermore, in this analytical approach, the following simplifications and assumptions was made: (1) The boundary frame is taken as rigid members; (2) the rocking contact points are at the extreme edge of the HBE-to-VBE flange bearing point shown by the "Rocking Contact Point" indicated in Figure 20; (3) local deformation effects at the rocking contact points are neglected; (4) elevation of the HBEs remain unchanged for a given VBE rotation during drift; (5) the HBE-to-VBE joints are frictionless and no PT clamping force is present, allowing the joint to rotate and move freely; and (6) at each VBE location, the line created by joining the points of HBE flange rocking and VBE base rocking points are parallel to the longitudinal axis of the associated VBE.

The formulation of a relationship for unrestrained beam growth first requires the development of an equation for the incremental VBE rotation $\Delta\theta$. This proceeds by first obtaining all of the incremental dimensions at the base of the affected VBE shown in the close-up detail in Figure 20. It

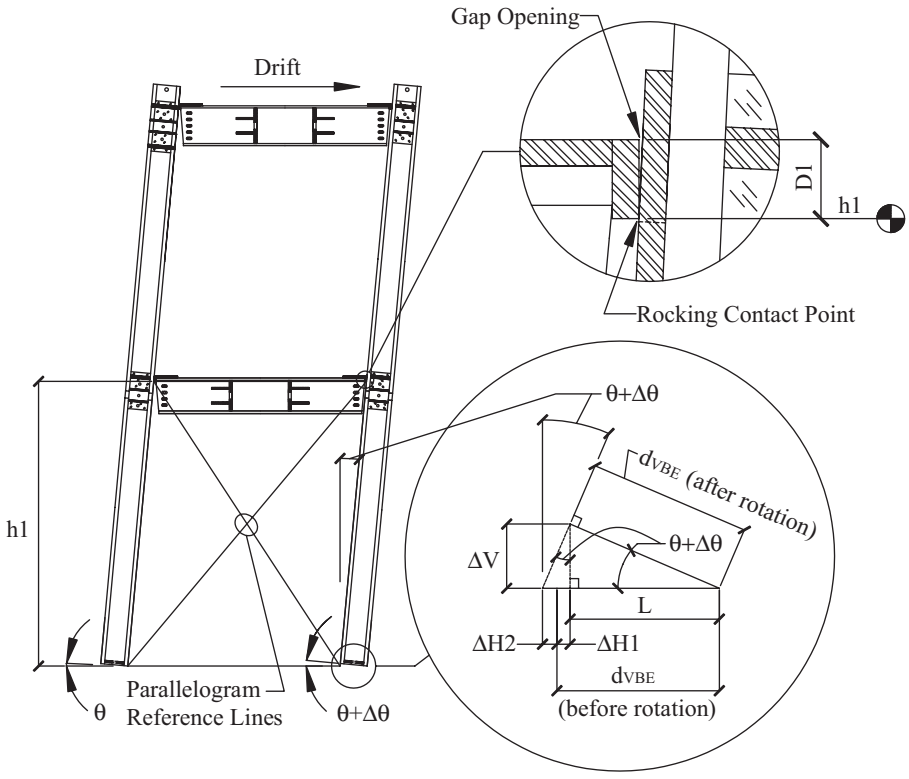

Fig. 20. Frame beam-growth kinematics: free-body diagram 1.

then follows, from geometry, that the vertical displacement at the VBE flange due to rotation is:

$$\Delta V = d_{VBE}\left[\sin(\theta+\Delta\theta)\right] \tag{42}$$

Next, the length of the horizontal projection of the base of the rotated VBE is found to be:

$$L = d_{VBE}\left[\cos(\theta+\Delta\theta)\right] \tag{43}$$

The additional unknown parameter needed to completely define the kinematics at the base of the VBE is ΔH. Derivation of the expression for this term is done in three steps. First, ΔH is equal to the sum of $\Delta H1$ and $\Delta H2$ such that:

$$\Delta H = \Delta H1 + \Delta H2 \tag{44}$$

Second, expanding Equation 44 into an expression in terms of tanθ shown directly in Figure 20 leads to:

$$\Delta H = (\Delta V)\left[\tan(\theta+\Delta\theta)\right] \tag{45}$$

Third, substituting Equation 42 into Equation 45 leads to:

$$\Delta H = d_{VBE}\left[\tan(\theta+\Delta\theta)\sin(\theta+\Delta\theta)\right] \tag{46}$$

Toward derivation of an expression for Δθ, the horizontal projection of the base of the rotated VBE extending beyond the footprint of the VBE prior to rotation needs to be established (i.e., $\Delta H2$), which can be calculated as:

$$\begin{aligned}\Delta H2 &= (\Delta H + L) - d_{VBE}\\ &= d_{VBE}\left[\tan(\theta+\Delta\theta)\sin(\theta+\Delta\theta)+\cos(\theta+\Delta\theta)-1\right]\end{aligned} \tag{47}$$

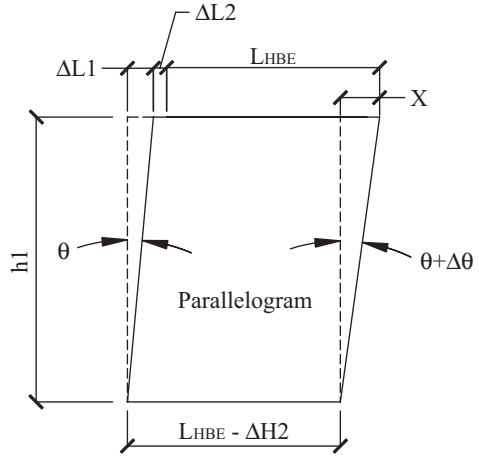

Fig. 21. Frame beam-growth kinematics: free-body diagram 2.

Additionally, the inside surface of the deformed frame displacement can be bounded by a parallelogram from which the geometry θ + Δθ can be determined and from which Δθ can then be calculated for any known value of θ (i.e., typically by selecting a target drift). From the free-body diagram of the parallelogram in Figure 21 for all remaining derivation steps, begin with defining the horizontal length due to frame drift as:

$$\Delta L1 = h1(\tan\theta) \tag{48}$$

The incremental horizontal length due to HBE-to-VBE gap opening is:

$$\Delta L2 = D1(\tan\theta) \tag{49}$$

Next, solving for tan(θ + Δθ), and substituting Equations 47, 48 and 49 for $\Delta H2$, $\Delta L1$ and $\Delta L2$, respectively, into Equation 50 leads to:

$$\begin{aligned}\tan(\theta+\Delta\theta) &= \frac{x}{h1}\\ &= \frac{(\Delta L1+\Delta L2+L_{HBE})-(L_{HBE}-\Delta H2)}{h1}\\ &= \frac{\Delta L1+\Delta L2+\Delta H2}{h1}\\ &= \frac{(h1+D1)\left[\tan(\theta)\right]+d_{VBE}\left[\tan(\theta+\Delta\theta)\sin(\theta+\Delta\theta)+\cos(\theta+\Delta\theta)-1\right]}{h1}\end{aligned} \tag{50}$$

Solving Equation 50 for tan(θ) leads to the following relationship defining unrestrained beam growth:

$$\tan(\theta) = \frac{\tan(\theta+\Delta\theta)\left\{h1-d_{VBE}\left[\sin(\theta+\Delta\theta)\right]\right\}+d_{VBE}\left[1-\cos(\theta+\Delta\theta)\right]}{h1+D1} \tag{51}$$

In this equation, all parameters have been defined previously and are known except for Δθ. One approach to solve Equation 51 consists of iterating on the value of Δθ until convergence. Once the parameter Δθ is known, the beam growth at each floor level can then be calculated.

Although the solution for Δθ will converge fairly quickly, an alternate simplified formulation can be used that provides an approximate solution without iteration. This is obtained by realizing that the reduction in length of the bottom of the parallelogram due to $\Delta H2$ (from the VBE base rotation) is insignificant. The procedure then follows by letting $\Delta H2 = 0$ in the preceding derivation; thus, the expression for tan(θ + Δθ) simplifies to:

$$\tan(\theta+\Delta\theta) \cong \frac{h1+D1}{h1}\left[\tan(\theta)\right] \tag{52}$$

Given the insignificance of $\Delta H2$, the approximate solution to obtain $\Delta\theta$ using Equation 52 will be within a percent accuracy compared to that using the exact relationship shown in Equation 51 that requires more computational effort. Once $\Delta\theta$ is known, the calculation of beam-growth demand at each level can be obtained. To illustrate the calculation of beam growth and the distribution along the frame height, using the frame shown in Figure 20 as an example, the calculations are made with the following assumptions:

- The story heights at each level are equal to h.
- The rocking depth at HBE level 1 and 2, respectively, is $D1 = D2 = D$.
- The height to the bottom gap opening $h1$ is equal to h to keep calculations simple for illustration purposes. This will lead to an approximate solution because $h1$ at the ground level is actually $h1 = h - D$ if story heights are equal.

The following calculations are then made:

Step 1 Calculate the gap adjustment $\delta = (\Delta\theta)(h1)$ due to beam-growth at the level 1 HBE. Because the adjustment is required at the level 1 HBE, the bottom of flange gap opening is zero (i.e., in bearing contact with the VBE flange). The top of flange gap opening is equal to $(D)(\theta + \Delta\theta)$.

Step 2 Calculate the gap openings at the roof HBE. The bottom of flange gap is equal to $(\Delta\theta)(2h)$; this represents the incremental gap opening required due to beam-growth. The top of flange gap is equal to $(\Delta\theta)(2h) + (\theta + \Delta\theta)(D)$; the first component represents the incremental gap opening required due to beam growth (also is the gap opening at the bottom of flange), and the latter component is the gap opening due to the joint rotation.

Note that if additional stories were present, beam-growth at each subsequent level would increase proportionally to the height of the bottom of flange level at that location only. For example, if there was an additional floor level in the example shown, the bottom of the flange gap would be equal to $(\Delta\theta)(3h)$ and the top of flange gap would be equal to $(\Delta\theta)(3h) + (\theta + \Delta\theta)(D)$. That is, the component due to the gap opening due to the joint rotation remains constant, and only the incremental gap opening due to beam growth increases with story height. Furthermore, to capture the beam-growth behavior about the top flange in the numerical model response, an alternate (but more complex) HBE-to-VBE model presented by Dowden and Bruneau (2014) would be required.

Two alternative modifications to the original proposed NewZ-BREAKSS rocking flange detail (Dowden and Bruneau, 2011) are proposed to eliminate the effects due to beam growth observed in the referenced large-scale NZ-SC-SPSW test. The first modification is to provide a semispherical bearing bar plate at the end of the HBE flange and reinforcement plates, as shown in Figure 22a. The second option is to provide both a semispherical bearing bar plate and additional PT elements near the bottom of the top flange, as shown in Figure 22b; these latter supplemental PT elements would be designed to always remain in tension. Although the first alternative should eliminate beam-growth effects, the latter option would further enhance the performance of the NewZ-BREAKSS connection and would also provide some increase in the recentering potential of the PT boundary frame.

SUMMARY AND CONCLUSIONS

Self-centering steel plate shear walls having NewZ-BREAKSS connections (i.e., NZ-SC-SPSW) are an alternative lateral-force-resisting system to conventional steel plate

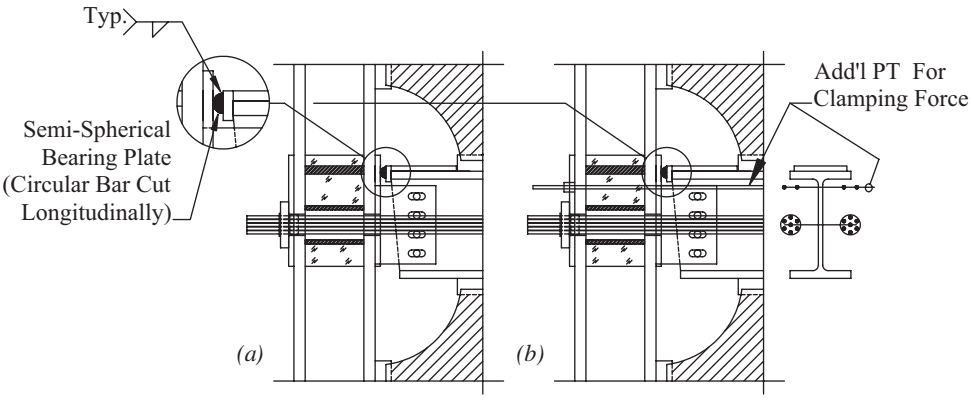

Fig. 22. Modified NewZ-BREAKSS detail: (a) alternative 1; (b) alternative 2.

shear walls for buildings located in regions of high seismicity. In this paper, the fundamental kinematic behavior of the NZ-SC-SPSW has been established. Closed-form solutions equations were derived for (1) HBE strength demands along the HBE based on capacity design principles, (2) infill web plate strains for HBE-to-VBE rocking joints, and (3) unrestrained beam growth with frames with rocking joints susceptible to beam-growth effects. Additionally, numerical models for the NewZ-BREAKSS connection using the programs SAP2000 and OpenSees were presented. Furthermore, nonlinear pushover analyses were conducted to validate the derived HBE strength demand equations and to provide insight on the effects of the PT on base shear versus roof drift frame response. The equations and free-body diagrams presented not only provide insight on the behavior of the NZ-SC-SPSW system, but also inform design. Furthermore, a modified NewZ-BREAKSS connection is proposed to eliminate beam-growth effects observed from recent large-scale tests (Dowden and Bruneau, 2014; Dowden et al., 2016).

ACKNOWLEDGMENTS

Financial support for this study was provided by the National Science Foundation as part of the George E. Brown Network for Earthquake Engineering Simulation under award number CMMI-0830294. Additional financial support for D. Dowden was provided by MCEER. Any opinions, findings, conclusions and recommendations presented in this paper are those of the authors and do not necessarily reflect the views of the sponsors.

REFERENCES

AIJ (1995), "Performance of Steel Buildings During the 1995 Hyogoken–Nanbu Earthquake," Tokyo: Architectural Institute of Japan. (In Japanese with English summary).

AISC (2010), *Seismic Provisions for Structural Steel Buildings,* ANSI/AISC 341-05, American Institute of Steel Construction, Chicago, IL.

Berman, J. and Bruneau, M. (2008), "Capacity Design of Vertical Boundary Elements in Steel Plate Shear Walls," *Engineering Journal*, AISC, Vol. 45, No. 1, 1st Quarter, pp. 57–71.

Christopoulos, C., Filiatrault, A., Uang, C.M. and Folz, B. (2002), "Posttensioned Energy Dissipating Connections for Moment-Resisting Steel Frame," *Journal of Structural Engineering*, ASCE, Vol. 128, No. 9, pp. 1,111–1,120.

Christopoulos, C., Pampanin, S. and Priestley, M.J.N. (2003), "Performance-Based Seismic Response of Frame Structures Including Residual Deformations. Part I: Single-Degree of Freedom Systems," *Journal of Earthquake Engineering*, Vol. 7, No. 1, pp. 97–118.

Clayton, P.M. (2013), "Self-Centering Steel Plate Shear Wall: Subassembly and Full-Scale Testing," Ph.D. dissertation, Department of Civil and Environmental Engineering, University of Washington, Seattle, WA.

Clayton, P.M., Berman, J.W. and Lowes, L.N. (2012), "Seismic Design and Performance of Self-Centering Steel Plate Shear Walls," *Journal of Structural Engineering*, ASCE, Vol. 138, No. 1, pp. 22–30.

Clifton, G.C. (1996), "Development of Perimeter Moment-Resisting Steel Frames Incorporating Semi-Rigid Elastic Joints," *Proc. New Zealand National Society for Earthquake Engineering Conference*, pp. 177–184.

Clifton, G.C. (2005), "Semi-Rigid Joints for Moment Resisting Steel Framed Seismic Resisting Systems," Ph.D. dissertation, Department of Civil and Environmental Engineering, University of Auckland, New Zealand.

Clifton, G.C., MacRae, G.A., Mackinven, H., Pampanin, S. and Butterworth, J. (2007), "Sliding Hinge Joints and Subassemblies for Steel Moment Frames," *Proc. New Zealand Society of Earthquake Engineering Annual Conference,* Paper 19, Palmerston North, New Zealand.

CSI (2009), "SAP2000: Static and Dynamic Finite Element Analysis of Structures (Version 14.1.0)," Computers and Structures Inc., Berkeley, CA.

Dowden, D.M. (2014), "Resilient Self-Centering Steel Plate Shear Walls," Ph.D. dissertation, Department of Civil and Environmental Engineering, University at Buffalo, Buffalo, NY.

Dowden, D.M. and Bruneau, M. (2014), "Analytical and Experimental Investigation of Self-Centering Steel Plate Shear Walls," *Technical Report MCEER-14-0010*, Multidisciplinary Center for Earthquake Engineering Research, State University of New York Buffalo, Buffalo, New York.

Dowden, D.M., Clayton, P.M., Li, C.-H., Berman, J.W., Bruneau, M, Lowes, L.N. and Tsai, K.C. (2016), "Full-Scale Pseudo-Dynamic Testing of Self-Centering Steel Plate Shear Walls," *Journal of Structural Engineering*, ASCE, Vol. 142, No. 1, doi: 10.1061/(ASCE) ST.1943-541X.0001367.

Dowden, D.M. and Bruneau, M. (2011), "NewZ-BREAKSS: Post-Tensioned Rocking Connection Detail Free of Beam Growth," *Engineering Journal*, AISC, Vol 48, No. 2, 2nd Quarter, pp. 153–158.

Dowden, D.M., Purba, R. and Bruneau, M. (2012),"Behavior of Self-Centering Steel Plate Shear Walls and Design Considerations." *Journal of Structural Engineering*, ASCE, Vol. 138, No. 1, pp. 11–21.

Garlock, M. (2002), "Design, Analysis, and Experimental Behavior of Seismic Resistant Post-Tensioned Steel Moment Frames," Ph.D. dissertation, Department of Civil and Environmental Engineering, Lehigh University, Bethlehem, PA.

Garlock, M., Ricles, J. and Sause, R. (2005), "Experimental Studies of Full-Scale Posttensioned Steel Connections," *Journal of Structural Engineering*, ASCE, Vol. 131, No. 3, pp. 438–448.

Kawashima, K., MacRae, G.A., Hoshikuma, J.-I. and Nagaya, K. (1998), "Residual Displacement Response Spectrum," *Journal of Structural Engineering*, ASCE, Vol. 124, No. 5, pp. 523–530.

Krawinkler, H., Anderson, J., Bertero V., Holmes, W. and Theil, C., Jr. (1996), "Steel Buildings," *Earthquake Spectra,* Vol. 12, No. S1, pp. 25–47.

MacRae, G.A., Clifton, G.C., Mackinven, H., Mago, N., Butterworth, J. and Pampanin, S. (2008), "The Sliding Hinge Joint Moment Connection," *Bulletin of the New Zealand Society for Earthquake Engineering,* Vol. 43, No. 3, pp. 202–212.

Mazzoni, S., McKenna, F., Scott, M.H. and Fenves, G.L. (2009), "Open System for Earthquake Engineering Simulation User Command-Language Manual—OpenSees Version 2.0," Pacific Earthquake Engineering Research Center, University of California, Berkeley, Berkeley, CA.

Pampanin, S., Christopoulos, C. and Priestley, M.J.N. (2003), "Performance-Based Seismic Response of Frame Structures Including Residual Deformations. Part II: Multi-Degree of Freedom Systems," *Journal of Earthquake Engineering*, Vol. 7, No. 1, pp. 119–147.

Ricles J.M., Sause R., Peng, S. and Lu, L. (2002), "Experimental Evaluation of Earthquake Resistant Posttensioned Steel Connections," *Journal of Structural Engineering*, ASCE, Vol. 128, No. 7, pp. 850–859.

Rojas, P., Ricles, J.M. and Sause, R. (2005), "Seismic Performance of Post-Tensioned Steel Moment Resisting Frames with Friction Devices," *Journal of Structural Engineering*, ASCE, Vol. 131, No. 4, pp. 529–540.

Sabelli, R. and Bruneau, M. (2007), *Steel Plate Shear Walls*, Design Guide 20, AISC, Chicago, IL.

Webster, D.J. (2013), "The Behavior of Unstiffened Steel Plate Shear Wall Web Plates and Their Impact on the Vertical Boundary Elements," Ph.D. dissertation, Department of Civil and Environmental Engineering, University of Washington, Seattle, WA.

Winkley, T.B. (2011), "Self-Centering Steel Plate Shear Walls: Large Scale Experimental Investigation," M.S. thesis, Department of Civil and Environmental Engineering, University of Washington, Seattle, WA.

Notes on the AISC 360-16 Provisions for Slender Compression Elements in Compression Members

LOUIS F. GESCHWINDNER and MATTHEW TROEMNER

ABSTRACT

Compression member strength is controlled by the limit states of flexural buckling, torsional buckling, and flexural-torsional buckling, as applicable. These compression members may buckle globally or locally, depending on the overall column slenderness and the local plate element slenderness for the plates that make up the shape. If any of the plate elements will buckle at a stress lower than that which would cause the column to buckle globally, the local buckling of the plate will control the overall column strength. When this occurs, the column is said to be composed of slender elements.

This paper will briefly discuss past specification provisions for slender element compression members and introduce the new provisions in the 2016 AISC *Specification*. It will present a simplification that reduces the number of constants that must be used and will present the specification requirements in an alternate format. Because the 2016 requirements result in different strengths than the 2010 requirements, figures are provided to illustrate the overall impact of these changes on column strength.

Key Words: compression members, plate buckling, slender elements, AISC *Specification*.

INTRODUCTION

Compression member strength is controlled by the limit states of flexural buckling, torsional buckling and flexural-torsional buckling, as applicable (AISC, 2010). These compression members may buckle globally or locally, depending on the overall column slenderness and the local plate element slenderness for the plates that make up the shape. If any of the plate elements will buckle at a stress lower than that which would cause the column to buckle globally, the local buckling of the plate will control the overall column strength. When this occurs, the column is said to be composed of slender elements.

This paper briefly discusses past specification provisions for slender element compression members and introduces the new provisions in the 2016 AISC *Specification*. It will present a simplification that reduces the number of constants that must be used and will present the specification requirements in an alternate format. Because the 2016 requirements result in different strengths than the 2010 requirements, figures are provided to illustrate the overall impact of these changes on column strength.

Louis F. Geschwindner, Ph.D, P.E., Senior Engineer, Providence Engineering Corporation, and Professor Emeritus, Architectural Engineering, The Pennsylvania State University, State College, PA (corresponding). Email: lfg@psu.edu

Matthew Troemner, Engineering and Research Intern, American Institute of Steel Construction, and Student, Architectural and Structural Engineering, Illinois Institute of Technology, Chicago, IL. Email: troemner@aisc.org

Paper No. 2015-29

HISTORICAL PERSPECTIVE

The AISC *Specification* approach for determining the element slenderness at which local buckling begins to control column strength has evolved over the years. Prior to the 1961 AISC *Specification*, a simple, maximum, width-to-thickness ratio was specified. For instance, in the 1949 *Specification,* the projecting elements of single-angle struts had a limiting width-to-thickness ratio of 12. In the 1961 *Specification,* the provisions were revised to include recognition that new materials with different yield strengths were being used and that yield strength of the material then played a role in determining at what stress level local buckling should be considered. The limit was changed to $2{,}400/\sqrt{F_y}$, where F_y was taken in pounds per square inch. In 1969, the limit was essentially unchanged but was presented as $76.0/\sqrt{F_y}$ with F_y now taken in kips per square inch. In order to convert the 1993 LRFD *Specification* to metric units, the 1994 Metric LRFD *Specification* set the limit as a unitless equation by restoring the variable E in the limit. Thus, this same limit became $0.45\sqrt{E/F_y}$. Over that same period of time, several new elements were defined. For the 2010 *Specification,* there were nine cases defined in Table B4.1a for the limiting width-to-thickness ratios for compression elements in members subject to axial compression. However, the actual limits were essentially the same as they had been since 1961.

During this same period, the approach to account for the influence of elements that exceeded these limitations also evolved. Prior to the 1969 *Specification,* the practice was to remove the width of the plate that exceeded the limitation. This approach required the section properties to be recalculated based on this new geometry, a cumbersome and

uneconomical approach. With the 1969 *Specification* (AISC, 1969), a new approach was introduced that followed the approach used in the 1969 AISI *Specification for the Design of Cold-Formed Steel Structural Members* (AISI, 1969). A reduction factor, Q, was defined as the ratio of the local buckling stress to the yield stress for members with slender elements. In the column strength equations, F_y was replaced by QF_y. Two separate approaches were used for determining Q. One was for unstiffened elements, which were assumed to reach their limit state when the element reached its local buckling stress. The other was for stiffened elements, which made use of their post-buckling strength. For unstiffened elements, Q was directly determined through specification equations based on material and geometric properties of the elements. For stiffened elements, an effective width was determined, and the ratio of the effective area to the gross area was used to establish Q. This approach was based on the actual stress in the member under the buckling load rather than the yield stress as was used for unstiffened elements. The provisions in the 2016 AISC *Specification* use the effective width approach for both stiffened and unstiffened elements following the practice used by AISI for cold-formed members since 2001 (AISI, 2001).

2016 SLENDERNESS PROVISIONS

To determine if one must even consider element slenderness in determining column strength, there needs to be some value against which the element width-to-thickness ratio can be compared. As has been the case since the 1961 *Specification*, when F_y was introduced as part of the limiting ratio, the assumption used to determine that limit is that the member can be uniformly stressed to the yield stress even though compression members are rarely stressed to this level. This limit, when exceeded, is used to direct the designer to Section E7, "Members with Slender Elements," of the *Specification* (AISC, 2010). This assumption caused some designers difficulty when they subsequently determined, after following all the requirements of Section E7, that the section strength was not reduced due to element slenderness. This can be understood by recognizing that the member is not stressed to the yield stress, as originally assumed to direct the designer to these provisions, so the element is less likely to buckle. Although the limits shown in Section E7 for 2016 now include the critical stress for the column determined without consideration of slender elements, it is still the width-to-thickness limit based on F_y from *Specification* Table B4.1a that tells the designer to consider the slender element provisions.

The 2016 provisions are written in a unified form for both stiffened and unstiffened elements using the effective width formulation for all but round HSS. This change is not so much the result of new research as it is a reinterpretation of the foundational work of von Kármán et al. (1932), Winter (1947), and Peköz (1987), as summarized in Ziemian (2010). The effective widths are used to determine the effective area, and that area is multiplied by the critical stress, determined without consideration of slender elements, to obtain the nominal compressive strength. The 2016 provisions, except for round HSS, are given as:

(a) When $\lambda \le \lambda_r \sqrt{\frac{F_y}{F_{cr}}}$

$$b_e = b \qquad \text{(2016 Spec. Eq. E7-2)}$$

(b) When $\lambda > \lambda_r \sqrt{\frac{F_y}{F_{cr}}}$

$$b_e = b\left(1 - c_1\sqrt{\frac{F_{el}}{F_{cr}}}\right)\sqrt{\frac{F_{el}}{F_{cr}}} \qquad \text{(2016 Spec. Eq. E7-3)}$$

where b is the element width, b_e is the element effective width, and F_{cr} is the critical stress determined in accordance with Section E3 or E4 without consideration of slender elements.

The limiting slenderness, λ_r, is taken from Table B4.1a and, in all cases, is a function of $\sqrt{E/F_y}$. The width-to-thickness ratio, λ, is, according to Table B4.1a, b/t, d/t or h/t, depending on the element being considered. Thus, the widths in Equations E7-2 and E7-3 will also be taken as b, d or h, depending on the element being considered.

The elastic local buckling stress, F_{el}, from classic plate buckling theory (Ziemian, 2010) is

$$F_{el} = k\frac{\pi^2 E}{12\left(1-\nu^2\right)\left(\frac{b}{t}\right)^2} \qquad (1)$$

which is written in the 2016 *Specification* as

$$F_{el} = \left(c_2\frac{\lambda_r}{\lambda}\right)^2 F_y \qquad \text{(2016 Spec. Eq. E7-4)}$$

The constant c_1 is the empirical correction factor associated with imperfection sensitivity and c_2 is a constant determined by c_1 alone and used only for convenience. The constants c_1 and c_2, given in 2016 *Specification* Table E7.1, are

Table E7.1 Effective Width Imperfection Adjustment Factor, c_1 and c_2 Factor			
Case	**Slender Element**	c_1	c_2
(a)	Stiffened elements except walls of square and rectangular HSS	0.18	1.31
(b)	Walls of square and rectangular HSS	0.20	1.38
(c)	All other elements	0.22	1.49

Table 1. Constants for Effective Width Equation								
Table B4.1a Case	**Table E7.1 Case**	k_c	c_1	c_2	c_3	c_4	c_5	**Appendix A Equation Number**
1	(c)	1.0	0.22	1.49	0.56	0.834	0.184	A-3
2	(c)	k_c	0.22	1.49	0.64	0.954	0.210	A-5
3	(c)	1.0	0.22	1.49	0.45	0.671	0.148	A-9
4	(c)	1.0	0.22	1.49	0.75	1.12	0.246	A-7
5	(a)	1.0	0.18	1.31	1.49	1.95	0.351	A-11
6	(b)	1.0	0.20	1.38	1.40	1.93	0.386	A-15
7	(a)	1.0	0.18	1.31	1.40	1.83	0.330	A-13
8	(a)	1.0	0.18	1.31	1.49	1.95	0.351	A-11

2016 SLENDERNESS PROVISIONS —SIMPLIFIED

Because these provisions require the use of the tabulated limiting slenderness ratio from Table B4.1a and the constants c_1 and c_2 from Table E7.1 each time a particular type element is considered, it may be helpful for the user to combine them all one time and then use this new equation. To accomplish this simplification, the limits from Table B4.1a are taken as $\lambda_r = c_3\sqrt{\frac{k_cE}{F_y}}$, so that the resulting equation can be used for all cases covered in that table except for round HSS. The variable k_c is taken as 1.0 for all cases in Table B4.1a, except Case 2 (flanges of built-up I-shaped sections and plates or angles projecting from built-up I-shaped sections), where it can vary from 0.35 to 0.76 (no change from earlier *Specifications*). Thus, the limit on application of Equation E7-3 becomes

$$\frac{b}{t} = \lambda > \lambda_r\sqrt{\frac{F_y}{F_{cr}}} = c_3\sqrt{\frac{k_cE}{F_y}}\sqrt{\frac{F_y}{F_{cr}}} = c_3\sqrt{\frac{k_cE}{F_{cr}}} \qquad (2)$$

Then determine F_{el} in terms of c_3. Thus,

$$F_{el} = \left(c_2\frac{\lambda_r}{\lambda}\right)^2 F_y = \left[c_2\left(\frac{c_3\sqrt{k_cE/F_y}}{b/t}\right)\right]^2 F_y = \left(\frac{c_2c_3\sqrt{k_cE/F_y}}{b/t}\right)^2 F_y \qquad (3)$$

Substituting F_{el} from Equation 3 into Equation E7-3 yields

$$b_e = b\left(1-c_1\sqrt{\frac{F_{el}}{F_{cr}}}\right)\sqrt{\frac{F_{el}}{F_{cr}}} = b\left[1-c_1\sqrt{\frac{\left(\frac{c_2c_3\sqrt{k_cE/F_y}}{b/t}\right)^2F_y}{F_{cr}}}\right]\sqrt{\frac{\left(\frac{c_2c_3\sqrt{k_cE/F_y}}{b/t}\right)^2F_y}{F_{cr}}} \qquad (4)$$

which simplifies to

$$b_e = c_2c_3t\sqrt{\frac{k_cE}{F_{cr}}}\left[1-\frac{c_1c_2c_3}{(b/t)}\sqrt{\frac{k_cE}{F_{cr}}}\right] \qquad (5)$$

Combining the constants in Equation 5 yields

$$b_e = c_4t\sqrt{\frac{k_cE}{F_{cr}}}\left[1-\frac{c_5}{(b/t)}\sqrt{\frac{k_cE}{F_{cr}}}\right] \qquad (6)$$

where $c_4 = c_2c_3$ and $c_5 = c_1c_2c_3$.

For all cases in Table B4.1a, except for round HSS for which the specification provisions are different and remain essentially unchanged from 2010, the constants are as tabulated in Table 1.

Table 2. Description of Shapes Used to Develop Figures				
Figure	**Shape**	**F_y, ksi**	**Element Slenderness**	**Limiting Slenderness for Local Buckling**
1	W30×90	50	$\frac{h}{t_w} = 57.5$	$1.49\sqrt{\frac{E}{F_y}} = 35.9$
2	HSS16×4×3/16	46	$\frac{h}{t} = 89$	$1.40\sqrt{\frac{E}{F_y}} = 35.2$
3	WT15×45	50	$\frac{d}{t_w} = 31.5$	$0.75\sqrt{\frac{E}{F_y}} = 18.1$
4	L5×3×¼	36	$\frac{d}{t} = 20$	$0.45\sqrt{\frac{E}{F_y}} = 12.8$
5	Built-up I-shape (slender flange) Flange: 24 in. × ½ in. Web: 24 in. × ¾ in.	50	$\frac{b_r}{2t_f} = 24$ $\frac{h}{t_w} = 32$	$0.56\sqrt{\frac{E}{F_y}} = 13.5$ $1.49\sqrt{\frac{E}{F_y}} = 35.9$
6	Built-up I-shape (slender flange and web) Flange: 24 in. × ½ in. Web: 24 in. × ½ in.	50	$\frac{b_r}{2t_f} = 24$ $\frac{h}{t_w} = 48$	$0.56\sqrt{\frac{E}{F_y}} = 13.5$ $1.49\sqrt{\frac{E}{F_y}} = 35.9$

Thus, for webs of doubly symmetric rolled I-shaped sections—Case 5 in Table B4.1a and Case (a) in Table E7.1—the following constants are determined:

$c_1 = 0.18$
$c_2 = 1.31$
$c_3 = 1.49$
$c_4 = 1.95$
$c_5 = 0.351$

and Equation E7-3 becomes, from Equation 6,

$$b_e = 1.95t\sqrt{\frac{E}{F_{cr}}}\left[1 - \frac{0.351}{(b/t)}\sqrt{\frac{E}{F_{cr}}}\right] \quad (7)$$

This effective width equation is very close to Equation E7-17 from the 2010 *Specification,* with the constants only slightly different. In addition, F_{cr} here is the same as f in Equation E7-17. The 2016 provisions are rewritten using Equation 6 and presented in full in this paper's Appendix.

The same comparison to the 2010 *Specification* cannot be made for unstiffened elements because the effective width approach in the 2016 *Specification* is a new approach for those elements.

IMPACT OF 2016 PROVISIONS

It is the intent of these new 2016 provisions to reduce the complex nature of the previous slender element provisions and to present a unified approach for both stiffened and unstiffened elements. In some instances, the changes implemented for 2016 will have little to no impact on the strength of slender element compression members, while in other instances, they may yield a significant increase in predicted strength. Where significant strength increase is seen with the 2016 provisions, the overly conservative nature of the previous provisions has been reduced.

Figures 1 through 6 illustrate the nominal strength for several slender element compression members, showing the results of the 2010 provisions and those of the 2016 provisions. As an aid to understanding the overall significance of slender elements on reducing column strength, the nominal strength, with the reduction for slender elements ignored, is also shown. The shapes used for Figures 1 through 6 and their element slenderness values are tabulated in Table 2.

In each of the cases presented, the rolled shape was selected because it is the one with the most slender element for that shape. The built-up shape was selected as an extreme case to illustrate the significance of the new provisions for

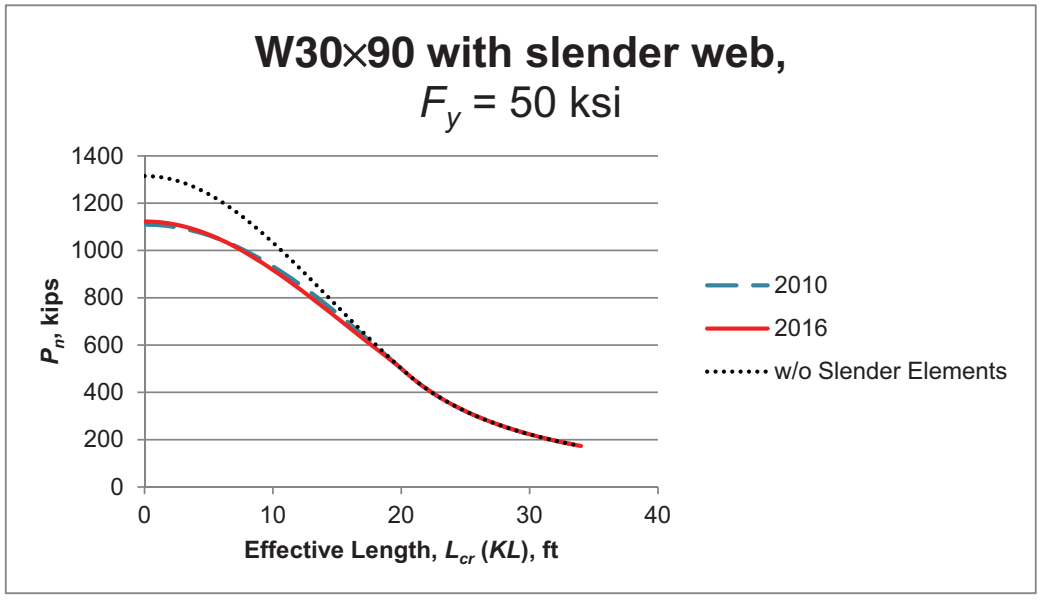

Fig. 1. Comparison of 2010 and 2016 slender element column strength, W30×90, F_y = 50 ksi.

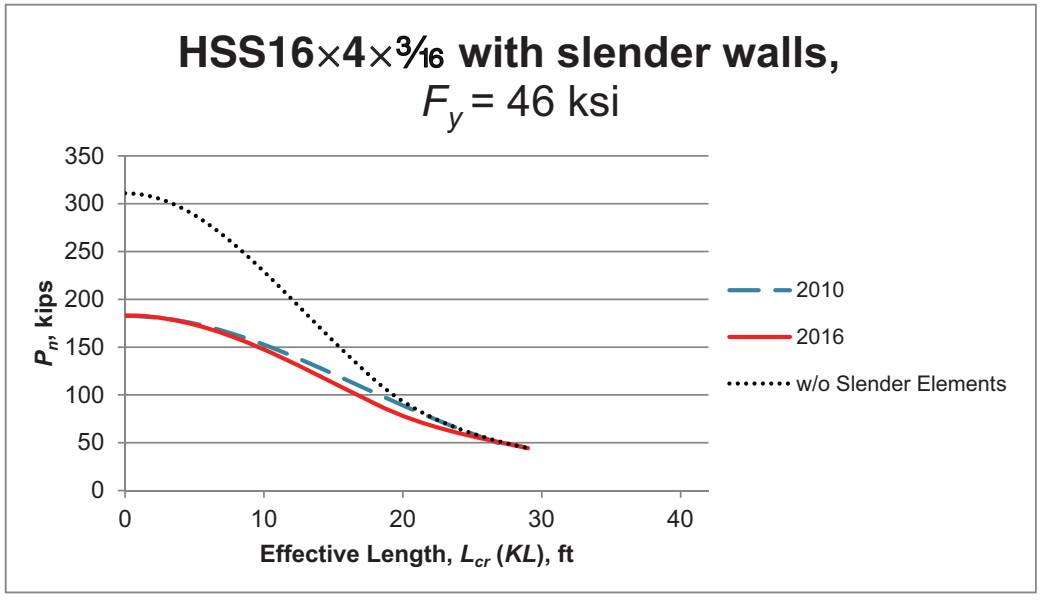

Fig. 2. Comparison of 2010 and 2016 slender element column strength, HSS16×4×3/16, F_y = 46 ksi.

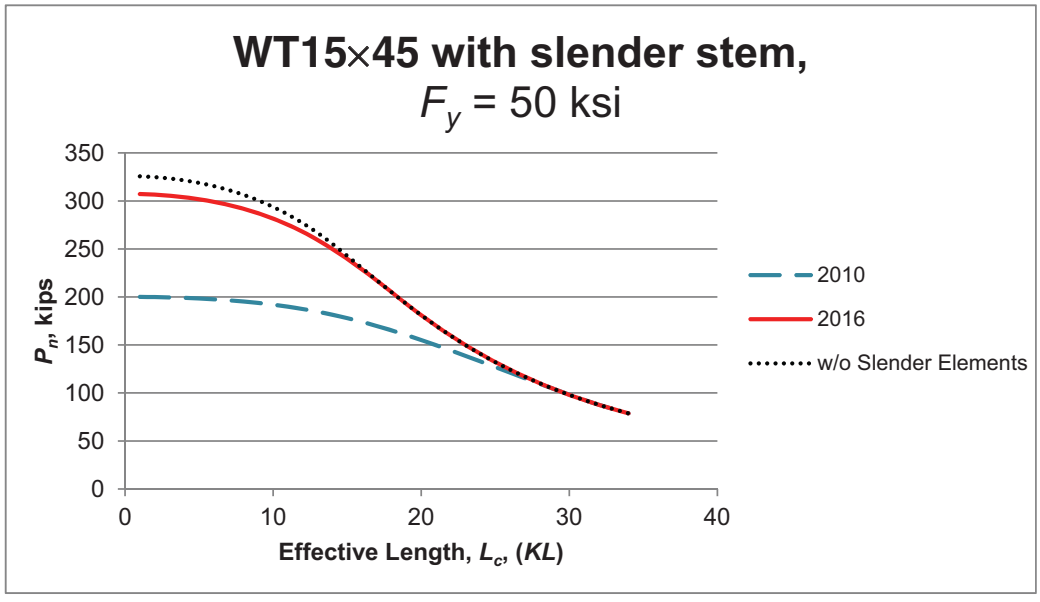

Fig. 3. Comparison of 2010 and 2016 slender element column strength, WT15×45, F_y = 50 ksi.

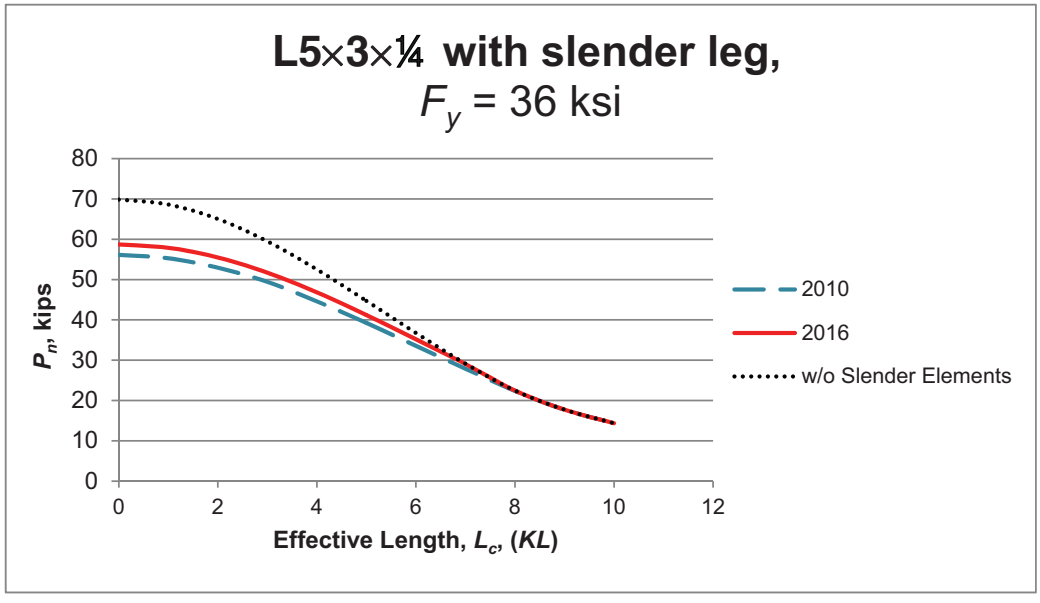

Fig. 4. Comparison of 2010 and 2016 slender element column strength, L5×3×¼, F_y = 36 ksi.

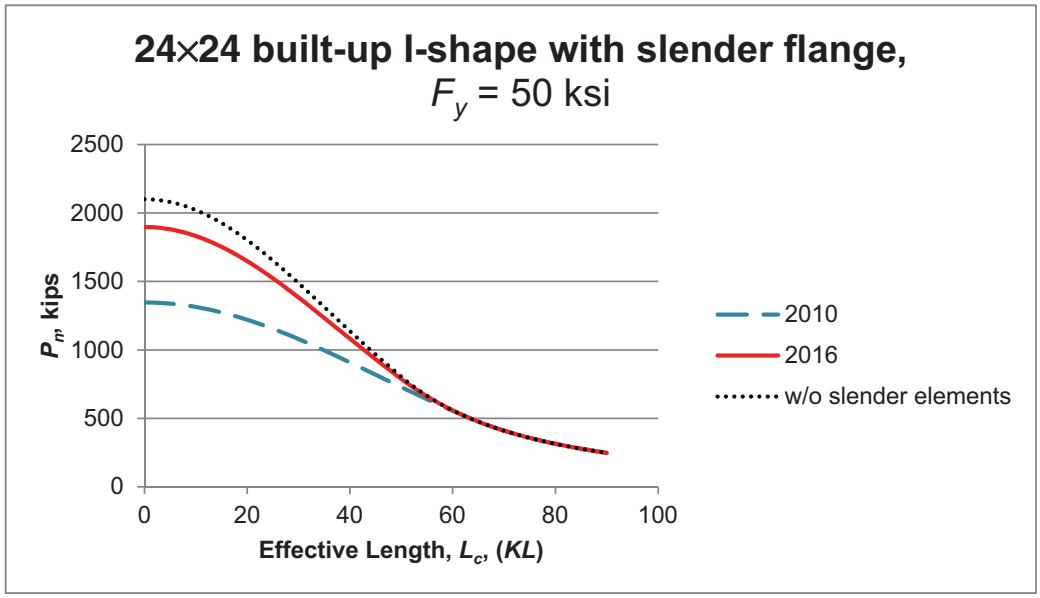

Fig. 5. Comparison of 2010 and 2016 slender element column strength, 24×24 built-up I-shape, F_y = 50 ksi.

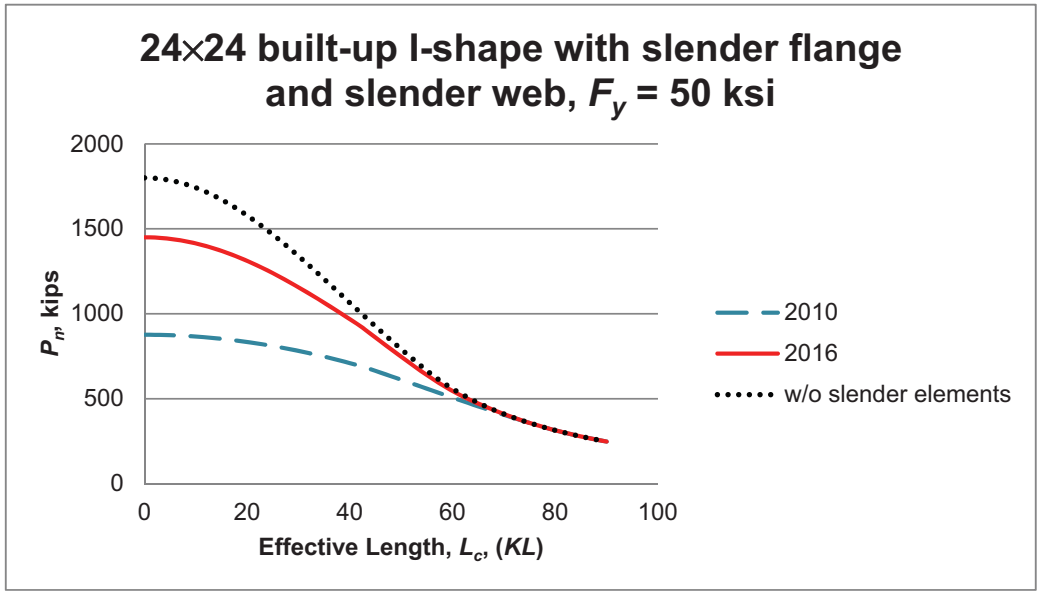

Fig. 6. Comparison of 2010 and 2016 slender element column strength, 24×24 built-up I-shape, slender web and slender flange, F_y = 50 ksi.

both slender flanges and slender webs. The shapes that show the most significant change are the built-up I-shape, WT and angle. These are all members with unstiffened slender elements. The W-shape and the HSS show less change, illustrating the relatively minor impact on columns with slender stiffened elements.

CONCLUSIONS

The 2016 *Specification* provisions for slender compression elements in compression members treats stiffened and unstiffened elements in a similar fashion through the same governing equation. It also accounts for the fact that columns are not designed to be stressed to the yield stress, so limiting width-to-thickness ratios need not be based on a limit established using the yield stress.

A comparison between the 2010 *Specification* and 2016 *Specification* for six slender element members shows that the change in strength can be significant for members with slender unstiffened elements. Two alternate approaches have been presented that produce the same results as the new 2016 *Specification*. Equation 6, with the constants given in Table 1, may be used for all slender element members except round HSS, or the expanded presentation given in the Appendix may be used.

REFERENCES

AISC (1969), *Specification for the Design, Fabrication, and Erection of Structural Steel for Buildings*, American Institute of Steel Construction, New York, NY.

AISC (2010), *Specification for Structural Steel Buildings*, ANSI/AISC 360-10, American Institute of Steel Construction, Chicago, IL.

AISI (1969), *Specification for the Design of Cold-Formed Steel Structural Members*, American Iron and Steel Institute, Washington, DC.

AISI (2001), *North American Specification for the Design of Cold-Formed Steel Structural Members*, American Iron and Steel Institute, Washington, DC.

Peköz, T. (1987), *Development of a Unified Approach to Design of Cold-Formed Steel Members*, American Iron and Steel Institute, Washington, DC.

von Kármán, T., Sechler, E.E. and Donnell, L.H. (1932), "The Strength of Thin Plates in Compression," *Transactions of the ASME*, Vol. 54.

Winter, G. (1947), "Strength of Thin Steel Compression Flanges," *Transactions of ASCE*, Vol. 112, p. 547.

Ziemian, R.D., ed. (2010), *Guide to Stability Design Criteria for Metal Structures*, 6th Ed., John Wiley & Sons Inc., Hoboken, NJ.

APPENDIX

This presentation reorganizes Section E7 of the 2016 AISC *Specification* with specific equations given for each case, similar to the 2010 *Specification*. The constants from Table E7.1 and Table 1 have been included in the equations. With the 2016 *Specification*, each time a particular shape is considered, the same constants will need to be used and the same equation will eventually result. Thus, writing out the equations once for each case, as done here, may be a simplification useful to the designer.

E7. MEMBERS WITH SLENDER ELEMENTS

This section applies to slender-element compression members, as defined in Section B4.1 for elements in uniform compression.

The nominal compressive strength, P_n, shall be the lowest value based on the applicable limit states of flexural buckling, torsional buckling, and flexural-torsional buckling.

$$P_n = F_{cr} A_e \tag{A-1}$$

where

A_e = summation of the effective areas of the cross-section based on the reduced effective width, b_e or d_e, in.^{2} (mm^2), or as given by Equations A-16 or A-17

F_{cr} = critical stress determined in accordance with Section E3 or Section E4, ksi (MPa)

1. Slender Unstiffened Elements

The effective width, b_e or d_e, for slender unstiffened elements is determined as follows:

(a) For flanges, angles and plates projecting from rolled columns or other compression members:

(i) When $\dfrac{b}{t} \le 0.56\sqrt{\dfrac{E}{F_{cr}}}$

$$b_e = b \tag{A-2}$$

(ii) When $\dfrac{b}{t} > 0.56\sqrt{\dfrac{E}{F_{cr}}}$

$$b_e = 0.834t\sqrt{\frac{E}{F_{cr}}}\left[1 - \frac{0.184}{\left(b/t\right)}\sqrt{\frac{E}{F_{cr}}}\right] \tag{A-3}$$

(b) For flanges, angles and plates projecting from built-up I-shaped columns or other compression members:

(i) When $\frac{b}{t} \le 0.64\sqrt{\frac{k_c E}{F_{cr}}}$

$$b_e = b \tag{A-4}$$

(ii) When $\frac{b}{t} > 0.64\sqrt{\frac{k_c E}{F_{cr}}}$

$$b_e = 0.954t\sqrt{\frac{k_c E}{F_{cr}}}\left[1-\frac{0.210}{(b/t)}\sqrt{\frac{k_c E}{F_{cr}}}\right] \tag{A-5}$$

where

$k_c = \frac{4}{\sqrt{h/t_w}}$ and shall not be taken less than 0.35 nor greater than 0.76 for calculation purposes

(c) For stems of tees:

(i) When $\frac{d}{t} \le 0.75\sqrt{\frac{E}{F_{cr}}}$

$$d_e = d \tag{A-6}$$

(ii) When $\frac{d}{t} > 0.75\sqrt{\frac{E}{F_{cr}}}$

$$d_e = 1.12t\sqrt{\frac{E}{F_{cr}}}\left[1-\frac{0.246}{(d/t)}\sqrt{\frac{E}{F_{cr}}}\right] \tag{A-7}$$

(d) For single angles, double angles with separators, and all other unstiffened elements:

(i) When $\frac{b}{t} \le 0.45\sqrt{\frac{E}{F_{cr}}}$

$$b_e = b \tag{A-8}$$

(ii) When $\frac{b}{t} > 0.45\sqrt{\frac{E}{F_{cr}}}$

$$b_e = 0.671t\sqrt{\frac{E}{F_{cr}}}\left[1-\frac{0.148}{(b/t)}\sqrt{\frac{E}{F_{cr}}}\right] \tag{A-9}$$

where

b = width of unstiffened compression element, as defined in Section B4.1, in. (mm)

d = depth of tee, as defined in Section B4.1, in. (mm)

t = thickness of element, as defined in Section B4.1, in. (mm)

2. Slender Stiffened Elements

The effective width, b_e, for slender stiffened elements is determined as follows:

(a) For all shapes except cover plates, diaphragm plates, walls of square and rectangular HSS and round HSS:

(i) When $\frac{b}{t} \le 1.49\sqrt{\frac{E}{F_{cr}}}$

$$b_e = b \tag{A-10}$$

(ii) When $\frac{b}{t} > 1.49\sqrt{\frac{E}{F_{cr}}}$

$$b_e = 1.95t\sqrt{\frac{E}{F_{cr}}}\left[1-\frac{0.351}{(b/t)}\sqrt{\frac{E}{F_{cr}}}\right] \tag{A-11}$$

(b) For cover plates and diaphragm plates:

(i) When $\frac{b}{t} \le 1.40\sqrt{\frac{E}{F_{cr}}}$

$$b_e = b \tag{A-12}$$

(ii) When $\frac{b}{t} > 1.40\sqrt{\frac{E}{F_{cr}}}$

$$b_e = 1.83t\sqrt{\frac{E}{F_{cr}}}\left[1-\frac{0.330}{(b/t)}\sqrt{\frac{E}{F_{cr}}}\right] \tag{A-13}$$

(c) For walls of square and rectangular HSS:

(i) When $\frac{b}{t} \le 1.40\sqrt{\frac{E}{F_{cr}}}$

$$b_e = b \tag{A-14}$$

(ii) When $\frac{b}{t} > 1.40\sqrt{\frac{E}{F_{cr}}}$

$$b_e = 1.93t\sqrt{\frac{E}{F_{cr}}}\left[1-\frac{0.386}{(b/t)}\sqrt{\frac{E}{F_{cr}}}\right] \tag{A-15}$$

(d) For round HSS, the effective area is determined as follows:

(i) When $\frac{D}{t} \leq \frac{0.11E}{F_y}$

$$A_e = A_g \tag{A-16}$$

(ii) When $\frac{0.11E}{F_y} < \frac{D}{t} < \frac{0.45E}{F_y}$

$$A_e = \left[\frac{0.038E}{F_y\left(D/t\right)} + \frac{2}{3}\right]A_g \tag{A-17}$$

where

D = outside diameter of round HSS, in. (mm)

t = thickness of wall, in. (mm)

Establishing and Developing the Weak-Axis Strength of Plates Subjected to Applied Loads

CHARLES J. CARTER, LARRY S. MUIR and BO DOWSWELL

ABSTRACT

When a plate is subjected to applied loads and significant out-of-plane deformation, the demand on the connection may exceed that derived from calculations due to the applied loads only. Where inelastic behavior is acceptable, the intent may be to ensure ductile behavior. For plates with fillet-welded edge connections, this can be accomplished by sizing the fillet welds to develop the strength of the plate.

One specific example of this arises when a brace in a special concentrically braced frame (SCBF) is subject to compression and buckles out-of-plane. Bending of the gusset plate may demand more of the gusset plate edge connection than the calculated forces that result on the gusset edge due to the brace force specified in Section F2.6c.2 of AISC 341-16 (AISC, 2016). If not accounted for in the weld size, the uncalculated weak-axis moment on the welds from out-of-plane bending of the gusset plate might cause rupture of the fillet welds to govern the behavior of the system.

The method provided in this paper is suitable to determine the minimum size of fillet welds necessary to prevent weld rupture as out-of-plane deformations occur. It can be used for fillet-welded gusset plate edges in SCBFs to satisfy the exception provided in Section F2.6c.4 of AISC 341-16.

Keywords: gusset plate, fillet welds, special concentrically braced frame, hinge, seismic, connection.

INTRODUCTION

When a plate is subjected to applied loads and significant out-of-plane deformation, the demand on the connection may exceed that derived from calculations due to the applied loads only. Where inelastic behavior is acceptable, the intent may be to ensure ductile behavior. For plates with fillet-welded edge connections, this can be accomplished by sizing the fillet welds to develop the strength of the plate.

One specific example of this arises when a brace in a special concentrically braced frame (SCBF) is subject to compression and buckles out-of-plane. Resulting weak-axis bending of the gusset plate may demand more of the gusset plate edge connection than the calculated forces that result on the gusset edge due to the brace force specified in Section F2.6c.2 of AISC 341-16 (AISC, 2016). If not accounted for in the weld size, the uncalculated weak-axis moment on the welds from out-of-plane bending of the gusset plate might cause rupture of the fillet welds to govern the behavior of the system.

Section F2.6c.4 of AISC 341-16—a new provision at the time of writing of this paper—provides a fairly simple approach that can be used to determine an appropriate fillet weld size to preclude this concern. It allows the required shear strength for the welds to be taken equal to $0.6R_yF_yt_p/\alpha_s$ (i.e., the expected shear strength of the plate), where these variables are defined in AISC 341-16. A user note is provided to further simplify this for common steel grades and double-sided fillet welds: A weld size of $0.62t_p$ is sufficient for 36-ksi gusset plates and 70-ksi weld metal, and a weld size of $0.74t_p$ is sufficient for 50-ksi gusset plates and 70-ksi weld metal.

An exception also is provided to recognize that a weak-axis flexural hinge in the gusset plate edge can be used to protect the fillet welds. It recognizes that the forces present from the brace consume a portion of the strength of the gusset plate edge. This paper explains how to calculate the portion consumed, the remainder of the gusset plate strength that must be developed, and the corresponding fillet weld size that will do so. It also shows that this approach will produce a smaller required fillet weld size than the other option provided in Section F2.6c.4 of AISC 341-16.

Charles J. Carter, S.E., P.E., Ph.D., Vice President and Chief Structural Engineer, AISC, Chicago, IL (corresponding). Email: carter@aisc.org

Larry S. Muir, P.E., Director of Technical Assistance, AISC, Roswell, GA. Email: muir@aisc.org

Bo Dowswell, P.E., Ph.D., Principal, ARC International, LLC, Birmingham, AL. Email: bo@arcstructural.com

Paper No. 2015-31

INTERACTION ON THE GUSSET PLATE EDGE

A yield mechanism can be used in the gusset plate to determine the maximum weak-axis bending moment that can exist in the presence of the gusset plate edge forces that result from the force in the brace. Using the generalized interaction equation recommended by Dowswell (2015), the total utilization of the gusset plate in shear, compression, and strong- and weak-axis bending can be expressed as:

$$\left(\frac{P_u}{\phi R_y P_y}\right)^2+\left(\frac{V_u}{\phi R_y V_p}\right)^4+\left[\left(\frac{M_{ux}}{\phi R_y M_{px}}\right)^{1.7}+\left(\frac{M_{uy}}{\phi R_y M_{py}}\right)^{1.7}\right]^{0.59}\le 1 \quad (1)$$

where

P_u = gusset edge compression force due to brace compression force specified in section F2.6c.2, kips

V_u = gusset edge shear force due to brace compression force specified in Section F2.6c.2, kips

M_{ux} = gusset edge strong-axis moment due to brace compression force specified in Section F2.6c.2, kip-in.

M_{uy} = gusset edge weak-axis moment due to deformations from brace buckling, kip-in.

$\phi R_y P_y = 0.9 R_y F_y L t_p$, the expected compression strength of the gusset place edge, kips

$\phi R_y V_p = 1.0(0.6 R_y F_y L t_p)$, the expected shear strength of the gusset plate edge, kips

$\phi R_y M_{px} = \dfrac{0.9 R_y F_y L t_p^2}{4}$, the expected strong-axis flexural strength of the gusset plate edge, kip-in.

$\phi R_y M_{py} = \dfrac{0.9 R_y F_y L t_p^2}{4}$, the expected weak-axis flexural strength of the gusset plate edge, kip-in.

R_y = ratio of the expected yield stress to the specified minimum yield stress, F_y

F_y = specified minimum yield stress, ksi

L = length of fillet welds on gusset plate edge, in.

t_p = gusset plate thickness, in.

Because all variables in Equation 1 except M_{uy} are known for a given gusset plate, it is convenient to rewrite it at the point of equivalency as follows:

$$M_{uy\ max}=\frac{0.9 R_y F_y L t_p^2}{4}\left[\left(1-P'^2-V'^4\right)^{1.7}-M'^{1.7}_x\right]^{0.59} \quad (2)$$

where

$$P' = \frac{P_u}{0.9 R_y F_y L t_p} \quad (3)$$

$$V' = \frac{V_u}{0.6 R_y F_y L t_p} \quad (4)$$

$$M'_x = \frac{4 M_{ux}}{0.9 R_y F_y L^2 t_p} \quad (5)$$

Equation 2 provides the maximum weak-axis moment, $M_{uy\ max}$, that can be delivered to the welds by the gusset plate in the presence of P_u, V_u, and M_{ux}.

In the preceding formulations, the expected yield strength, $R_y F_y$ is used rather than the minimum specified yield strength, F_y. To not use R_y would reduce the denominator in these terms—and thereby also reduce the calculated value of the remaining weak-axis flexural demand, $M_{uy\ max}$, that must be developed. $R_y F_y$ also is used in the denominator of the weak-axis flexural strength ratio as provided in Section A3.2 in AISC 341-16 because all of these ratios are determined for the same element in the interaction equation.

DESIGN REQUIREMENTS FOR GUSSET PLATE EDGE FILLET WELDS

The four required strengths at the gusset plate edge (P_u, V_u, M_{ux} and $M_{uy\ max}$) can be used to design fillet welds that will fully develop the edge of the gusset plate and preclude weld rupture. All four effects produce shear on the effective throat of the fillet weld. The effects of P_u, M_{ux} and $M_{uy\ max}$ all are oriented transverse to the fillet weld, while the effect of V_u is oriented parallel to the weld axis. Accordingly, the maximum weld force per unit length due to the combination of all four effects can be expressed as follows:

$$f_u=\sqrt{f_{uv}^2+\left(f_{up}+f_{um_x}+f_{um_y}\right)^2} \quad (6)$$

where

$$f_{uv} = \frac{V_u}{2L}, \text{ kips/in.} \quad (7)$$

$$f_{up} = \frac{P_u}{2L}, \text{ kips/in.} \quad (8)$$

$$f_{um_x} = \frac{2M_{ux}}{L^2}, \text{ kips/in.} \quad (9)$$

$$f_{um_y} = \frac{M_{uy\ max}}{\left(t_p+0.5w\right)L}, \text{ kips/in.} \quad (10)$$

w = weld size, in.

The corresponding weld design strength per inch is:

$$\phi r_n = 1.392D\left(1.0 + 0.5\sin^{1.5}\theta\right) \tag{11}$$

where

$$\theta = \tan^{-1}\left(\frac{f_{up} + f_{um_x} + f_{um_y}}{f_{uv}}\right) \tag{12}$$

Here, D is the number of sixteenths in the weld size, and the basic weld strength of $1.392D$ is determined as explained in Part 8 of the AISC *Steel Construction Manual* (AISC, 2011). Because the quantity in Equation 11 must equal or exceed the quantity in Equation 6, the minimum weld size can be determined as:

$$D_{min} = \frac{f_u}{1.392\left(1.0 + 0.5\sin^{1.5}\theta\right)} \tag{13}$$

This weld size is sufficient to develop the gusset plate; therefore, it is unnecessary to also apply the "Richard" 1.25 weld ductility factor (AISC, 2011), which is used to address hot spots in cases where the welds do not develop the gusset plate.

Equation 10 is based on a moment arm equal to the distance between centroids of the effective throats of the fillet welds taken at 45 degrees in the welds ($t_p + 0.5w$); see Figure 1. Although some references illustrate the use of the weld area centroids—a moment arm of $t_p + 0.67w$ in this case—the calculations in this paper are made relative to the centroids of the effective throats, and the moment arm of $t_p + 0.5w$ is used for consistency.

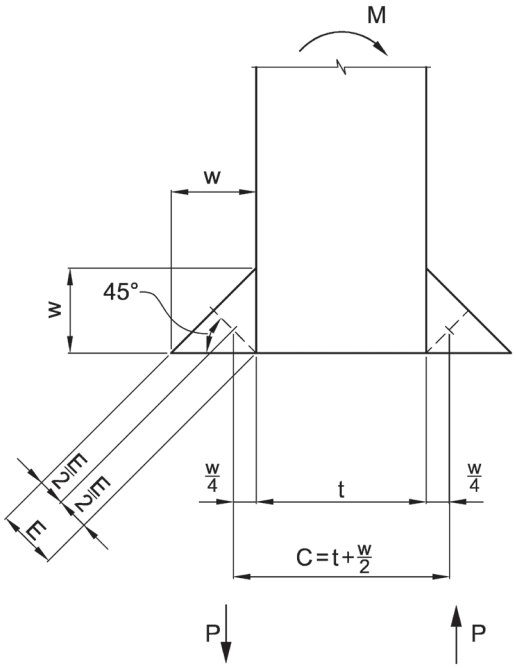

Fig. 1. Moment arm for weak-axis bending.

This equation is directly useful when checking a design, as shown in Examples 1 and 2 at the end of this paper, but requires iteration when designing a connection. Iteration can be minimized by assuming a weld size; a reasonable starting assumption is $w = t_p/2$, in which case, $t_p + 0.5w = 1.25t_p$. Alternatively, the weld size can be ignored in design and the moment arm taken as t_p if the resulting penalty is not objectionable.

COMPARISON TO TEST DATA

Table 1 shows the available testing (Johnson, 2005; Roeder, 2015) by which the suitability of the foregoing method can be judged. Predicted and actual test results are shown as GY and BR for gusset yielding and brace rupture and WR for weld rupture. The former is the desired behavior; the latter is undesirable.

Note that weld tearing as testing progresses is not preventable and should not be confused with weld rupture. The geometric deformations of the specimens during testing will cause tearing starting at the ends of the welds. As long as the specimen remains viable and the brace continues to function through the testing until the brace fractures, it is an acceptable result. The key concept here is that the weld tearing cannot be unstable and result in complete weld rupture. Rather, weld tearing must be stable so that gusset yielding can occur, and ultimately, brace rupture will limit the test.

Tests are available on both sides of the prediction point of the method, and as can be seen in Table 1, the prediction of the method provided in this paper is correct for all tests shown. The testing by Roeder (2015) and the two edge connections in test HSS 01 (Johnson, 2005) are the most relevant because they bound the prediction and all have a weld size within 1⁄16 in.—the smallest increment of weld size—of the prediction of the method.

Table 1 also shows a comparison to the use of the $0.6R_yF_yt_p/\alpha_s$ provision from Section F2.6c.4 of AISC 341-16, which is easier to use but requires a larger weld size than the method provided in this paper. Adjusting from weld size to weld volume to better reflect the impact on the cost of welding, the difference is from 125% to 300% in the cases shown in Table 1.

ASD DERIVATION

All of the foregoing information was presented using LRFD equations. Following are the similar equations for an ASD solution:

Table 1. Test Data and Comparison of Method Predition to Actual Results

	Roeder SCBF 1	Roeder SCBF 2	Roeder SCBF 3	Johnson HSS 01 (beam edge)	Johnson HSS 01 (column edge)	Johnson HSS 02 (beam edge)	Johnson HSS 02 (column edge)	Johnson HSS 03 (beam edge)	Johnson HSS 03 (column edge)	Johnson HSS 04 (beam edge)	Johnson HSS 04 (column edge)	Johnson HSS 05 (beam edge)	Johnson HSS 05 (column edge)
General Parameters													
L, in.	20	18	17.375	33	29	24	20	24	20	24.5	20.375	24	20
t_p, in.	0.5	0.625	0.625	0.5	0.5	0.5	0.5	0.5	0.5	0.5	0.5	0.375	0.375
w, in.	5/16	1/4	1/4	3/16	3/16	1/2	1/2	7/16	7/16	7/16	7/16	5/16	5/16
F_{exx}, ksi	70	70	70	70	70	70	70	70	70	70	70	70	70
F_y, ksi	50	50	50	50	50	50	50	50	50	50	50	50	50
R_y	1.1	1.1	1.1	1.1	1.1	1.1	1.1	1.1	1.1	1.1	1.1	1.1	1.1
Gusset Edge Forces													
P_u, kips	84.8	83.6	83.5	64.3	49.1	71.5	54.6	71.5	54.6	71.3	54.5	68.2	52.1
V_u, kips	116	106	92.8	139	124	115	97.7	115	97.7	116	100	109	93.2
M_{ux}, kip-in.	7	59.1	0	6.43	0	7.15	0	7.15	0	10.7	6	6.82	0
Calculated Parameters													
P'	0.171	0.150	0.155	0.0787	0.0684	0.120	0.110	0.120	0.110	0.118	0.108	0.153	0.140
V'	0.352	0.286	0.259	0.255	0.259	0.290	0.296	0.290	0.296	0.287	0.297	0.367	0.377
Mx'	0.00283	0.0236	0	0.000954	0	0.00201	0	0.00201	0	0.00288	0.00234	0.00255	0
$M_{uy\ max}$, kip-in.	59.1	84.4	81.6	101	88.9	72.6	60.6	72.6	60.6	74.2	61.8	40.0	33.4
f_{uv}, kips/in.	2.90	2.94	2.67	2.11	2.14	2.40	2.44	2.40	2.44	2.37	2.45	2.27	2.33
f_{up}, kips/in.	2.12	2.32	2.40	0.974	0.847	1.49	1.37	1.49	1.37	1.46	1.34	1.42	1.30
f_{umx}, kips/in.	0.0350	0.365	0	0.0118	0	0.0248	0	0.0248	0	0.0357	0.0289	0.0237	0
f_{umy}, kips/in.	4.50	6.25	6.26	5.16	5.16	4.04	4.04	4.21	4.22	4.22	4.22	3.14	3.14
f_u, kips/in.	7.26	9.41	9.07	6.49	6.38	6.05	5.93	6.21	6.09	6.18	6.10	5.12	5.02
θ, radians	1.16	1.25	1.27	1.24	1.23	1.16	1.15	1.17	1.16	1.18	1.16	1.11	1.09
D_{min}, 16ths	3.63	4.62	4.44	3.19	3.14	3.02	2.97	3.09	3.04	3.07	3.05	2.58	2.55
w_{min}, in.	1/4	5/16	5/16	1/4	1/4	1/4	3/16	1/4	1/4	1/4	1/4	3/16	3/16
Results													
Is $w \geq w_{min}$?	Yes	No	No	No	No	Yes	Yes	Yes	Yes	Yes	Yes	Yes	Yes
By how much?	1/16" >	1/16" <	1/16" <	1/16" <	1/16" <	1/4" >	5/16" >	3/16" >	3/16" >	3/16" >	3/16" >	1/8" >	1/8" >
Prediction	GY & BR	WR	WR	WR	WR	GY & BR	GY & BR	GY & BR	GY & BR	GY & BR	GY & BR	GY & BR	GY & BR
Actual Behavior	GY & BR	WR	WR	WR	WR	GY & BR	GY & BR	GY & BR	GY & BR	GY & BR	GY & BR	GY & BR	GY & BR
Method works?	Yes	Yes	Yes	Yes	Yes	Yes	Yes	Yes	Yes	Yes	Yes	Yes	Yes
Alternative $0.6R_yF.0_yt_p/\alpha$ Comparison													
D_{min}, 16ths	5.93	7.41	7.41	5.93	5.93	5.93	5.93	5.93	5.93	5.93	5.93	4.45	4.45
w_{min}, in.	3/8	1/2	1/2	3/8	3/8	3/8	3/8	3/8	3/8	3/8	3/8	5/16	5/16
Size increase	1/8	3/16	3/16	1/8	1/8	1/8	3/16	1/8	1/8	1/8	1/8	1/8	1/8
% vol. increase	125%	156%	156%	125%	125%	125%	300%	125%	125%	125%	125%	178%	178%

$$\left(\frac{P_a\Omega}{R_yP_y}\right)^2+\left(\frac{V_a\Omega}{R_yV_p}\right)^4+\left[\left(\frac{M_{ax}\Omega}{R_yM_{px}}\right)^{1.7}+\left(\frac{M_{ay}\Omega}{R_yM_{py}}\right)^{1.7}\right]^{0.59}\le 1 \quad (1a)$$

where

P_a = gusset edge compression force due to brace compression force specified in Section F2.6c.2, kips

V_a = gusset edge shear force due to brace compression force specified in Section F2.6c.2, kips

M_{ax} = gusset edge strong-axis moment due to brace compression force specified in Section F2.6c.2, kip-in.

M_{ay} = gusset edge weak-axis moment due to deformations from brace buckling, kin-in.

$\frac{R_yP_y}{\Omega} = \frac{R_yF_yLt_p}{1.67}$, the expected compression strength of the gusset plate edge, kips

$\frac{R_yV_p}{\Omega} = \frac{0.6R_yF_yLt_p}{1.5}$, the expected shear strength of the gusset plate edge, kips

$\frac{R_yM_{px}}{\Omega} = \frac{R_yF_yL^2t_p}{4(1.67)}$, the expected strong-axis flexural strength of the gusset plate edge, kip-in.

$\frac{R_yM_{py}}{\Omega} = \frac{R_yF_yLt_p^2}{4(1.67)}$, the expected weak-axis flexural strength of the gusset plate edge, kip-in.

$$M_{ay\ max}=\frac{R_yF_yLt_p^2}{4(1.67)}\left[\left(1-P'^2-V'^4\right)^{1.7}-M_x'^{1.7}\right]^{0.59} \quad (2a)$$

where

$$P' = \frac{1.67P_a}{R_yF_yLt_p} \quad (3a)$$

$$V' = \frac{1.5V_a}{0.6R_yF_yLt_p} \quad (4a)$$

$$M'_x = \frac{4(1.67)M_{ax}}{R_yF_yL^2t_p} \quad (5a)$$

$$f_a = \sqrt{f_{av}^2+\left(f_{ap}+f_{am_x}+f_{am_y}\right)^2} \quad (6a)$$

where

$$f_{av} = \frac{V_a}{2L},\ \text{kips/in.} \quad (7a)$$

$$f_{ap} = \frac{P_a}{2L},\ \text{kips/in.} \quad (8a)$$

$$f_{am_x} = \frac{2M_{ax}}{L^2},\ \text{kips/in.} \quad (9a)$$

$$f_{am_y} = \frac{M_{ay\ max}}{\left(t_p+0.5w\right)L},\ \text{kips/in.} \quad (10a)$$

$$\frac{r_n}{\Omega} = 0.928D\left(1.0+0.5\sin^{1.5}\theta\right) \quad (11a)$$

where

$$\theta = \tan^{-1}\left(\frac{f_{ap}+f_{am_x}+f_{am_y}}{f_{av}}\right) \quad (12a)$$

$$D_{min} = \frac{f_a}{0.928\left(1.0+0.5\sin^{1.5}\theta\right)} \quad (13a)$$

CONCLUSIONS

The method provided in this paper is suitable to determine the minimum size of fillet welds necessary to prevent weld rupture as out-of-plane deformations occur. It can be used for fillet-welded gusset plate edges in special concentrically braced frames (SCBFs) to satisfy the exception provided in Section F2.6c.4 of AISC 341-16.

REFERENCES

AISC (2011), *Steel Construction Manual,* 14th Ed., American Institute of Steel Construction, Chicago, IL, p. 8-8.

AISC (2012), *Seismic Design Manual,* 2nd Ed., American Institute of Steel Construction, Chicago, IL.

AISC (2016), *Seismic Provisions for Structural Steel Buildings*, ANSI/AISC 341-16, American Institute of Steel Construction, Chicago, IL.

Dowswell, B. (2015), "Plastic Strength of Connection Elements," *Engineering Journal*, AISC, Vol. 52, No. 1, First Quarter, pp. 47–65, Chicago, IL.

Johnson, S.M. (2005), *Improved Seismic Performance of Special Concentrically Braced Frames*, Masters Thesis, University of Washington, Seattle, WA.

Muir, L.S. and Thornton, W.A. (2014), *Vertical Bracing Connections—Analysis and Design*, AISC Design Guide 29, American Institute of Steel Construction, Chicago, IL.

Roeder, C. (2015), "Three SCBF Test Reports Provided to AISC," University of Washington, Seattle, WA.

Example 1. ASTM A36 Gusset Plate Using Theoretical Derivation

Consider the gusset plate-to-beam flange fillet welds for the upper gusset plate illustrated in Figure 2 [Figure 5-33 of the AISC *Seismic Design Manual* (AISC, 2012)] and the loads for Case 2 (a 444-kip brace force; see page 5-230). Determine if the ⅜-in. fillet welds used are acceptable for the new criterion. (Note that this example in the 2nd Edition AISC *Seismic Design Manual* illustrates the requirements in the 2010 AISC *Seismic Provisions*, which did not contain a requirement like that in Section F2.6c.4 of AISC 341-16 and illustrated in this paper.)

From the example:

$L = 25.75$ in. $t_p = 0.75$ in. $F_y = 36$ ksi $R_y = 1.3$ $F_{EXX} = 70$ ksi
$V_u = 216$ kips $P_u = 193$ kips $M_{ux} = 0$ kip-in.

The maximum weak-axis flexural moment that can exist in the presence of V_u, P_u, and M_{ux} can be calculated as follows:

$$P' = \frac{P_u}{0.9R_yF_yLt_p} \tag{3}$$
$$= \frac{193 \text{ kips}}{0.9(1.3)(36 \text{ ksi})(25.75 \text{ in.})(0.75 \text{ in.})}$$
$$= 0.237 \text{ kip}$$

$$V' = \frac{V_u}{0.6R_yF_yLt_p} \tag{4}$$
$$= \frac{216 \text{ kips}}{0.6(1.3)(36 \text{ ksi})(25.75 \text{ in.})(0.75 \text{ in.})}$$
$$= 0.398 \text{ kip}$$

$$M_x' = \frac{4M_{ux}}{0.9R_yF_yL^2t_p} \tag{5}$$
$$= 0 \text{ kip-in.}$$

$$M_{uy\ max} = \frac{0.9R_yF_yLt_p^2}{4}\left[\left(1 - P'^2 - V'^4\right)^{1.7} - M_x'^{1.7}\right]^{0.59} \tag{2}$$
$$= \frac{0.9(1.3)(36 \text{ ksi})(25.75 \text{ in.})(0.75 \text{ in.})^2}{4}\left\{\left[1 - \left(0.237 \text{ kip}\right)^2 - \left(0.398 \text{ kip}\right)^4\right]^{1.7} - 0^{1.7}\right\}^{0.59}$$
$$= 140 \text{ kip-in.}$$

The resultant weld force per inch can be calculated as follows:

$$f_{uv} = \frac{V_u}{2L} \tag{7}$$
$$= \frac{216 \text{ kips}}{2(25.75 \text{ in.})}$$
$$= 4.19 \text{ kips/in.}$$

$$f_{up} = \frac{P_u}{2L} \tag{8}$$
$$= \frac{193 \text{ kips}}{2(25.75 \text{ in.})}$$
$$= 3.75 \text{ kips/in.}$$

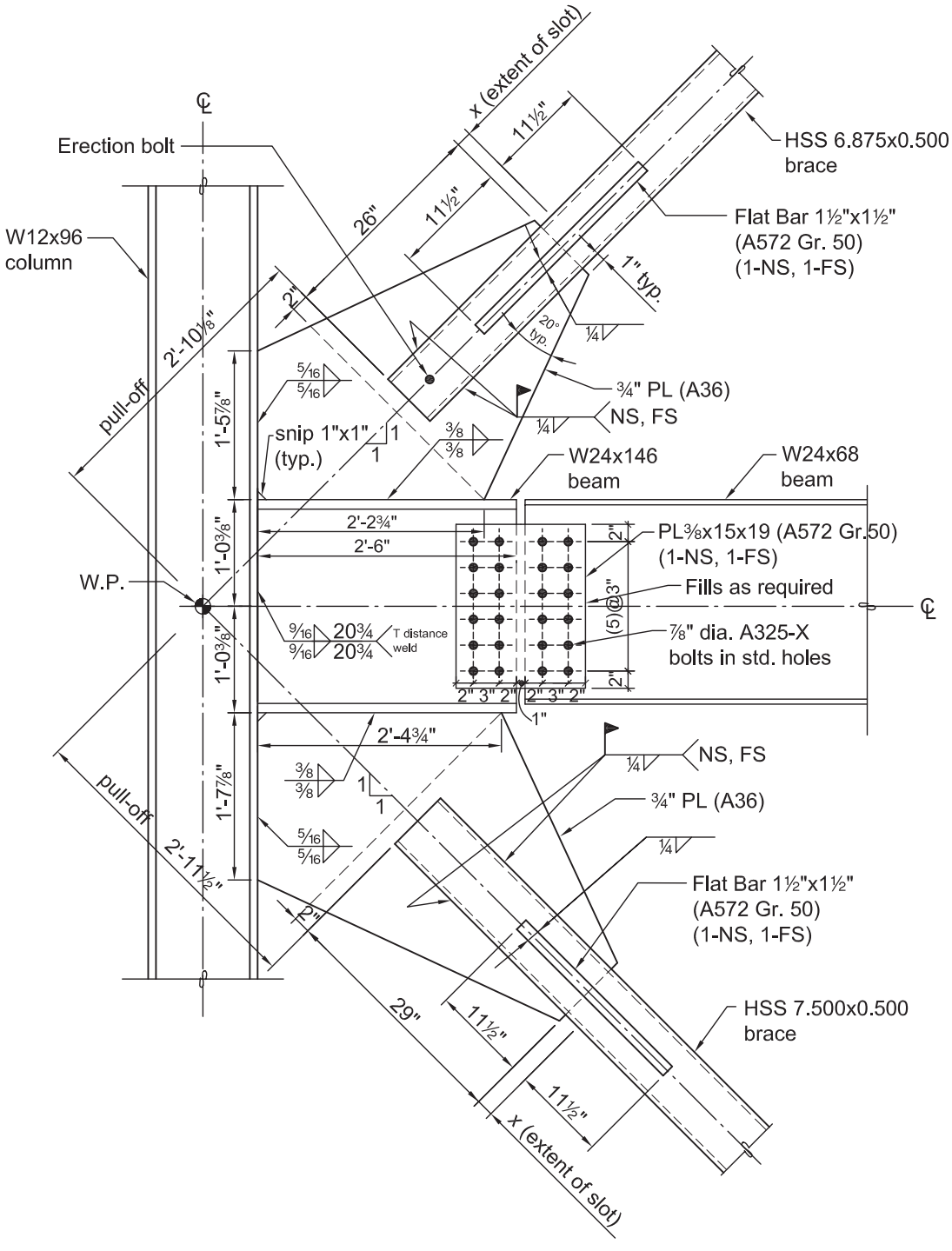

Note: A325-X bolts are to be pretensioned with slip-critical faying surfaces.

Fig. 2. Replication of Figure 5-33 of the AISC Seismic Design Manual, 2nd Ed.

$$f_{um_x} = \frac{2M_{ux}}{L^2} \tag{9}$$
$$= 0 \text{ kips/in.}$$

$$f_{um_y} = \frac{M_{uy\ max}}{\left(t_p + 0.5w\right)L} \tag{10}$$
$$= \frac{140 \text{ kip-in.}}{\left[0.75 \text{ in.} + 0.5(0.375 \text{ in.})\right](25.75 \text{ in.})}$$
$$= 5.80 \text{ kips/in.}$$

$$f_u = \sqrt{f_{uv}^2 + \left(f_{up} + f_{um_x} + f_{um_y}\right)^2} \tag{6}$$
$$= \sqrt{(4.19 \text{ kips/in.})^2 + (3.75 \text{ kips/in.} + 0 + 5.80 \text{ kips/in.})^2}$$
$$= 10.4 \text{ kips/in.}$$

$$\theta = \tan^{-1}\left(\frac{f_{up} + f_{um_x} + f_{um_y}}{f_{uv}}\right)$$
$$= \tan^{-1}\left(\frac{3.75 \text{ kips/in.} + 0 + 5.80 \text{ kips/in.}}{4.19 \text{ kips/in.}}\right)$$
$$= 1.16 \text{ radians}$$

The required fillet weld size can be calculated as follows:

$$D_{min} = \frac{f_u}{1.392\left(1.0 + 0.5\sin^{1.5}\theta\right)} \tag{13}$$
$$= \frac{(10.4 \text{ kips/in.})}{1.392\left[1.0 + 0.5\sin^{1.5}(1.16)\right]}$$
$$= 5.21 \text{ sixteenths}$$

The ⅜-in. fillet welds shown are adequate for the proposed criterion.

Now compare to the fillet weld size that would be required by the $0.6R_yF_yt_p/\alpha_s$ alternative provision given in Section F2.6c.4 of AISC 341-16:

$$D_{min} = \frac{0.6R_yF_yt_p/\alpha_s}{2\times1.392} = \frac{0.6(1.3)(36 \text{ ksi})(0.75 \text{ in.})/1.0}{2\times1.392} = 7.56 \text{ sixteenths}$$

These ½-in. fillet welds, though easier to determine, would require 78% more weld metal volume.

Example 2. ASTM A572 Grade 50 Gusset Plate Using Theoretical Derivation

Consider the gusset plate-to-beam flange fillet welds for the gusset plate illustrated in Figure 3 [Figure 6-1 of AISC Design Guide 29 (Muir and Thornton, 2014)] and the brace compression force of 783 kips (see page 296). Determine if the ½-in. fillet welds used are acceptable for the new criterion. (Note that this example in AISC Design Guide 29 illustrates the requirements in the 2010 AISC *Seismic Provisions*, which did not contain a requirement like that in Section F2.6c.4 of AISC 341-16 and illustrated in this paper.)

From the example:

$L = 34.25$ in. $t_p = 1$ in. $F_y = 50$ ksi $R_y = 1.1$ $F_{EXX} = 70$ ksi
$V_u = 493$ kips $P_u = 161$ kips $M_{ux} = 1{,}290$ kip-in.

The maximum weak-axis flexural moment that can exist in the presence of V_u, P_u, and M_{ux} can be calculated as follows:

$$P' = \frac{P_u}{0.9R_yF_yLt_p} \tag{3}$$

$$= \frac{161 \text{ kips}}{0.9(1.1)(50 \text{ ksi})(34.25 \text{ in.})(1 \text{ in.})}$$

$$= 0.0949 \text{ kip}$$

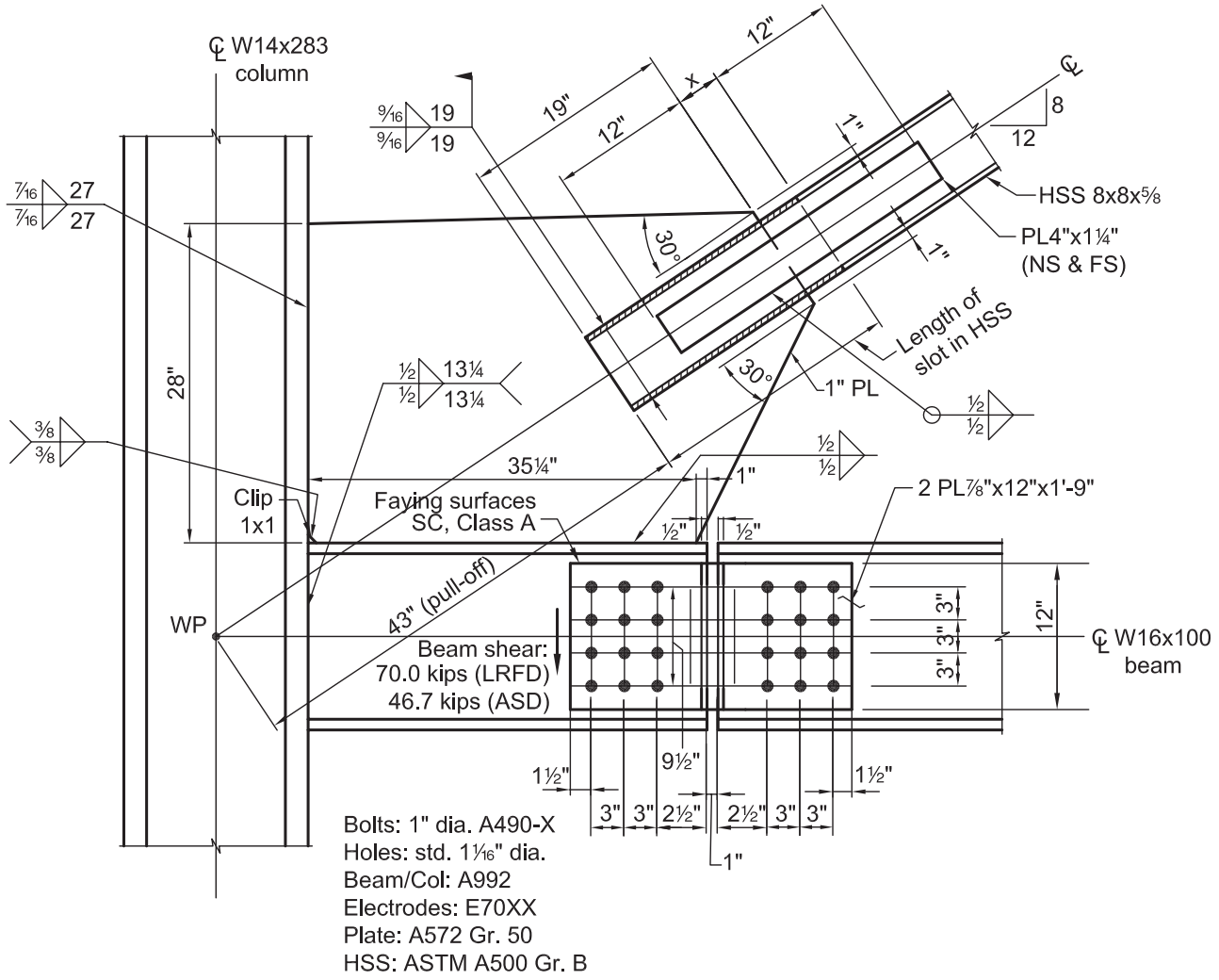

Fig. 3. Replication of Figure 6-1 of AISC Design Guide No. 29.

$$V' = \frac{V_u}{0.6R_yF_yLt_p} \quad (4)$$
$$= \frac{493 \text{ kips}}{0.6(1.1)(50 \text{ ksi})(34.25 \text{ in.})(1 \text{ in.})}$$
$$= 0.436 \text{ kip}$$

$$M_x' = \frac{4M_{ux}}{0.9R_yF_yL^2t_p} \quad (5)$$
$$= \frac{4(1{,}290 \text{ kip-in.})}{0.9(1.1)(50 \text{ ksi})(34.25 \text{ in.})^2(1 \text{ in.})}$$
$$= 0.0889 \text{ kip-in.}$$

$$M_{uy\ max} = \frac{0.9R_yF_yLt_p^2}{4}\left[\left(1 - P'^2 - V'^4\right)^{1.7} - M_x'^{1.7}\right]^{0.59} \quad (2)$$
$$= \frac{0.9(1.1)(50 \text{ ksi})(34.25 \text{ in.})(1 \text{ in.})^2}{4}\left\{\left[1 - (0.0949 \text{ kip})^2 - (0.436 \text{ kip})^4\right]^{1.7} - (0.0889 \text{ kip-in.})^{1.7}\right\}^{0.59}$$
$$= 400 \text{ kip-in.}$$

The resultant weld force per inch can be calculated as follows:

$$f_{uv} = \frac{V_u}{2L} \quad (7)$$
$$= \frac{493 \text{ kips}}{2(34.25 \text{ in.})}$$
$$= 7.20 \text{ kips/in.}$$

$$f_{up} = \frac{P_u}{2L} \quad (8)$$
$$= \frac{161 \text{ kips}}{2(34.25 \text{ in.})}$$
$$= 2.35 \text{ kips/in.}$$

$$f_{um_x} = \frac{2M_{ux}}{L^2} \quad (9)$$
$$= \frac{2(1{,}290 \text{ kip-in.})}{(34.25 \text{ in.})^2}$$
$$= 2.20 \text{ kips/in.}$$

$$f_{um_y} = \frac{M_{uy\ max}}{\left(t_p + 0.5w\right)L} \quad (10)$$
$$= \frac{400 \text{ kip-in.}}{\left[1 \text{ in.} + 0.5(0.5 \text{ in.})\right](34.25 \text{ in.})}$$
$$= 9.35 \text{ kips/in.}$$

$$f_u = \sqrt{f_{uv}^2 + \left(f_{up} + f_{um_x} + f_{um_y}\right)^2} \quad (6)$$
$$= \sqrt{(7.20 \text{ kips/in.})^2 + (2.35 \text{ kips/in.} + 2.20 \text{ kips/in.} + 9.35 \text{ kips/in.})^2}$$
$$= 15.7 \text{ kips/in.}$$

$$\theta = \tan^{-1}\left(\frac{f_{up} + f_{um_x} + f_{um_y}}{f_{uv}}\right)$$
$$= \tan^{-1}\left(\frac{2.35 \text{ kips/in.} + 2.20 \text{ kips/in.} + 9.35 \text{ kips/in.}}{7.20 \text{ kips/in.}}\right)$$
$$= 1.09 \text{ radians}$$

The required fillet weld size can be calculated as follows:

$$D_{min} = \frac{f_u}{1.392\left(1.0 + 0.5\sin^{1.5}\theta\right)} \tag{13}$$
$$= \frac{15.7 \text{ kips/in.}}{1.392\left[1.0 + 0.5\sin^{1.5}(1.09)\right]}$$
$$= 7.93 \text{ sixteenths}$$

The ½-in. fillet welds shown are adequate for the proposed criterion.

Now compare to the fillet weld size that would be required by the $0.6R_yF_yt_p/\alpha_s$ alternative provision given in Section F2.6c.4 of AISC 341-16:

$$D_{min} = \frac{0.6R_yF_yt_p/\alpha_s}{2\times1.392} = \frac{0.6(1.1)(50 \text{ ksi})(1 \text{ in.})/1.0}{2\times1.392} = 11.9 \text{ sixteenths}$$

These ¾-in. fillet welds, though easier to determine, would require 125% more weld metal volume.

Strength of Beams in Beam-to-Column Connections with Holes in the Tension Flange

JAMES A. SWANSON

ABSTRACT

A discussion of several approaches to predicting the flexural strength of beams with holes in the tension flanges is presented. Experimental data pertinent to the discussion is then presented, summarized and analyzed. It is observed that although provisions in the AISC 360-16 specification predict a net section fracture of the tension flanges in a number of the experiments, many of those beams were able to achieve their full plastic moment prior to failure. Two alternative models are proposed as improvements to the provisions in AISC 360-16; the merits and limitations of those models are discussed.

Keywords: beam-to-column connection, moment connection, bolted connection, net section fracture, flange plate connection, T-stub connection, double-tee connection.

INTRODUCTION

When a bolted connection is made to the flange of a beam, material is invariably removed, which can require either reinforcing of the flange or a reduction in available strength of the beam. The issue of reduced strength or net sections in flexural members dates back as early as 1891 (Lilly and Carpenter, 1939). The issue was first encountered in the context of plate girders—before the acceptance of modern welding procedures, sections were invariably built up from plates and angles that were riveted together resulting in girders with numerous flange perforations. Before experimental data were available to indicate otherwise, strength calculations were based on the net-section properties of the girders, even though deflections were often computed using gross-section properties.

The 1939 paper by Lilly and Carpenter includes discussion by W. R. Osgood, which refers to an experiment conducted by Friedrich Hartmann, wherein Hartmann concluded that "in the absence of considerations of fatigue, girders of symmetrical cross sections may be designed safely on the basis of gross moment of inertia." Lilly and Carpenter used two experiments to investigate the elastic stiffness and flange stresses of flexural members built up from plates that were riveted together using angles. Based on the findings of their study, they suggested that the design of girders could be based on the gross-section girder properties but proposed an equation resulting in a slightly reduced "effective" moment of inertia. The two girders tested by Lilly and Carpenter, however, were not tested to failure. The extensive discussion that followed the publication of the paper is evidence of just how contentious the issue was. At least 18 different engineers and scientists wrote to express their opinions of Lilly and Carpenter's findings—most expressed their discomfort with the idea of using the gross-section properties for the design of girders, even when designs were limited by elastic allowable stresses.

Today, girders built up from plates and angles that are riveted together are a thing of past, but the idea of using effective section properties or imposing reductions to the available strength of beams and girders persists. One of the most direct applications on these provisions is in the design of bolted moment connections in lateral force resisting systems.

BACKGROUND

AISC General Provisions

The provisions in Section B10 of the 3rd Edition LRFD *Specification* (AISC, 1999) covered the determination of flexural strength of rolled or built-up members with holes in their tension flanges. The provisions consisted of a design check, shown as Equation 1, wherein an engineer investigated the ratio of the net-section-fracture strength to the gross-section-yielding strength, both evaluated using corresponding resistance factors. In cases where the available gross-section-yielding strength governed the behavior of the tension flange, the full plastic moment of the section was available and could be used. When the net-section-fracture

James A. Swanson, Associate Professor, Department of Civil and Architectural Engineering and Construction Management, University of Cincinnati, Cincinnati, OH. Email: swansojs@ucmail.uc.edu

Paper No. 2015-32

strength governed, however, a reduction in strength was required. This reduction was made by computing an effective area for the tension flange using Equation 2, which included the ratio of resistance factors of 0.75 to 0.90, or 5/6. Using the effective flange area, modified flexural properties were computed and the moment capacity was based on the modified section modulus.

$$0.75F_uA_{fn} \geq 0.90F_yA_{fg} \quad (1)$$

$$A_{fe} = \frac{5}{6}\frac{F_u}{F_y}A_{fn} \quad (2)$$

where

F_y = yield strength of beam material, ksi

F_u = ultimate strength of beam material, ksi

A_{fg} = gross tension flange area, in.^{2}

A_{fn} = net tension flange area, in.^{2}

A_{fe} = effective net tension flange area, in.^{2}

An unfortunate reality of these provisions, however, was that almost none of the members tabulated in the AISC *Steel Construction Manual* (AISC, 2001) would pass the initial design check when two typically sized bolt holes are placed in the flange, as would be typical for a bolted beam-to-column connection. If A992 material is assumed for the beam and it is assumed that two 7/8-in.-diameter bolts are placed in the beam flanges, not a single W-section in the manual would satisfy the criterion shown as Equation 1. As a result, using the 1999 provisions, it is impossible to design to a fully bolted moment connection capable of reaching the plastic moment of the beam without providing reinforcement to the flanges.

The revised provisions appearing in Section F13 of AISC 360-05 (AISC, 2005), which remain unchanged in AISC 360-10 (AISC, 2010b) and AISC 360-16 (AISC, 2016b), are largely the same as those in AISC 1999 except for three subtle, but important changes. The check of net-section-fracture strength versus gross-section-yielding strength now appears as shown in Equation 3. Like before, when this design check is satisfied, no reduction in moment capacity is needed, and the full plastic moment of the beam can be used. The first difference is that the resistance factors of 0.75 and 0.90 have been removed from the design check and from the reduction formula. The second difference is that a factor, Y_T, was added in the design check to guard against the detrimental effect of a high-yield-strength to ultimate-strength ratio. The last difference is in the way that the strength reduction is made for beams failing the design check. Previously, if a section failed the design check shown in Equation 3, an engineer had to recompute the section properties of the beam based on an effective flange area and then base the moment capacity on yielding at that location. This approach has been streamlined by using the ratio of A_{fn} to A_{fg} to modify the nominal elastic section modulus, S_x. This reduced modulus is then multiplied by the ultimate strength, as shown in Equation 4, to arrive at the moment capacity at the net section.

$$F_uA_{fn} \geq Y_TF_yA_{fg} \quad (3)$$

$$M_n = \frac{F_uA_{fn}}{A_{fg}}S_x \quad (4)$$

where

$Y_T = 1.0$ when $F_y/F_u \leq 0.80$

$Y_T = 1.1$ when $F_y/F_u > 0.80$

S_x = section modulus for the beam's gross section, in.^{3}

The basis for the changes from the 1999 provisions to the 2005 provisions is discussed by Geschwindner (2010). An important ramification of the changes is that a larger number of W-sections pass the design check, permitting them to be designed for their full plastic moment capacity without flange reinforcement. As before, if A992 material is assumed for the beam and it is assumed that two 7/8-in.-diameter bolts are placed in the beam flanges, more than two-thirds of the tabulated W-sections pass the AISC 360-16 design check shown as Equation 3.

AASHTO Provisions

The American Association of State Highway Transportation Officials (AASHTO) specification (AASHTO, 2016) includes a provision to limit stress at net sections of girders. The provision, shown as Equation 5, limits the stress in the tension flange, f_l, under strength limit loading and during construction. Rewriting the equation, it can be shown that the moment capacity of the member at the net section is limited by the smaller of the yield moment, F_yS_x, or the moment corresponding to fracture, as shown in Equation 6. The value of 0.84 found in both equations is the ratio of the AASHTO resistance factor for fracture, 0.80, to the factor for yielding, 0.95. It should be noted that a comparison of the 0.84 factor in Equation 6 to the factor of 5/6 in Equation 2 must include the understanding that the AASHTO specification is based on a different probabilistic model for loading than the AISC specifications, which refers to ASCE-7-10 (2010):

$$f_l \leq 0.84\left(\frac{A_{fn}}{A_{fg}}\right)F_u \leq F_y \quad (5)$$

$$M_n = 0.84\left(\frac{A_{fn}}{A_{fg}}\right)F_uS_x \leq F_yS_x \quad (6)$$

Because the focus of this paper is beams and beam-to-column connections in buildings, wherein the sections, connections, and splices are often proportioned differently than in bridges, the AASHTO provisions are included for sake of completeness but will not be discussed further.

AISC Seismic Provisions

When beam-to-column connections are designed for special moment frames and intermediate moment frames, one option for satisfying the conformance demonstration required in the AISC *Seismic Provisions* (AISC, 2010a) is to select a connection prequalified by the AISC Connection Prequalification Review Panel (CPRP) (AISC, 2011). Two connections in the current AISC 358 specification, the bolted flange plate (BFP) and Kaiser bolted bracket (KBB) connections, and one more to appear in the next edition of the specification (AISC, 2016b), the double-tee (DT) connection, employ connections whereby the beam is bolted through its flanges.

The design procedure for the BFP connection includes a check of the beam net section to make sure that the beam can reach its full plastic moment. The check is written such that the maximum bolt diameter is determined, assuming that standard holes are used in the beam flange. Although this check is expressed differently, it is algebraically the same as the provisions in Section F13 of AISC 360-16 as shown in Equation 3.

The KBB provisions make no mention of a check for the net section of the connected beam but do employ "clamp plates" on the inside faces of the beam flanges to limit distortion and strains at the net section due to local buckling and necking (AISC, 2011; Kasai and Bleiman, 1996). The commentary to the KBB provisions notes that in similar experiments performed with and without clamp plates, those without clamp plates failed by necking and then fracture through the net section of beam flanges, whereas those experiments with the clamp plates failed via yielding and fracture through the gross section of the beam flange outside of the clamped region. The provisions also mention the reduced strength of the column resulting from drilling holes. In step 7 of the design procedure, a check of the column net section is performed that is consistent with Section F13 of AISC 360-16 shown in Equation 3. The commentary cites work by Masuda et al. (1998) that showed that removing as much as 30 to 40% of the column flange resulted in only a 10% reduction in yield moment.

The 2016 AISC 358 specification (AISC, 2016a) will include double-tee standards that require the strength corresponding to fracture on the net plastic section to be greater than the plastic moment of the gross section. Written in terms of the expected strengths, R_yF_y and R_tF_u, this requirement can be written mathematically as shown in Equation 7. Restricting the discussion to A992 steel where $R_y = R_t$, it can be shown that the full plastic moment capacity of the section is available provided that $Z_{x,net}/Z_x$ is not less than $F_y/F_u = 0.7692$.

$$Z_{x,net}R_tF_u \geq Z_xR_yF_y \tag{7}$$

The introduction of Equation 7 was born from the idea that the provisions in AISC 360 were too conservative, as was evidenced by experimentation, and that the comparison of net fracture and gross yielding limit states should be made at the plastic moment as opposed to the yield moment. Because the context within which this equation is presented is that of a full-strength moment connection, no mention is made of a reduced moment capacity of the beam in the case that Equation 7 is not satisfied.

SUMMARY OF RECENTLY ADDED EXPERIMENTAL DATA

During an investigation of the moment capacity of T-stub connections at the Georgia Institute of Technology (Smallidge, 1999; Swanson, 1999; Schrauben, 1999; Swanson and Leon, 2000), several fully bolted moment connections were able to develop moments in the beams that exceeded the plastic moment of the sections. Further, in studies on bolted flange plate connections at the University of Texas, University of Illinois, and the University of California–San Diego (Larson, 1996; Schneider and Teeraparbwong, 2002; Sato et al., 2007), several more moment connections with bolted flanges were also able to develop moments in the beams that exceeded the plastic moment of the sections. Finally, in experiments on steel girders with holes in the tension flanges conducted at the University of Minnesota (Altstadt, 2004), three of four specimens were able to develop bending moments that exceeded the plastic moment of the sections. In all of these cases, the beams failed to satisfy the net-section-facture design check in Section B10 of the 1999 provisions, and in several cases, the beams failed to satisfy the net-section-facture design check in Section F13 of AISC 360-16.

The following sections summarize recent research data that are applicable to the current discussion. The first three programs—conducted at Georgia Tech, the University of Texas, and the University of Illinois—were completed as part of the SAC Steel Project in the aftermath of the 1994 Northridge, California, earthquake; the fourth program, conducted at UC San Diego, focused on bolted flange plate connection performance in special moment frames; and the last program was conducted at the University of Minnesota in 2003 to investigate the rotational capacity of girders constructed from high-performance steel (50W and 70W). An additional test program, conducted in 2004 at the University

of Cincinnati to provide additional data to answer questions about the influence of fabrication methods on the strength and ductility of net sections (Yuan, 2005), is not included in this work because the experiments were of specimens loaded axially instead of flexurally.

Georgia Tech T-Stub Tests

As part of the SAC Steel Project conducted in the aftermath of the Northridge earthquake, a series of eight full-scale beam-column subassemblies was tested at the Georgia Institute of Technology in 1998 (Schrauben, 1999; Smallidge, 1999; Swanson 1999). These assemblies, summarized in Table 1, consisted of cantilever beams connected to pinned-pinned columns using fully bolted T-stub connections to resist moment and a shear tab connections to resist shear. Values reported for F_y and F_u in Table 1 were measured during material testing performed at Georgia Tech. The critical section noted in the table is the net section in the beam at the row of bolts farthest from the face of the column. The connections were loaded by applying a displacement to the ends of the cantilever beams.

Connections FS-01 and FS-02 were designed as partial-strength top-and-seat angle connections and are not reported herein. Connection FS-03 failed when the stem of one of the T-stubs connecting the beam to the column sustained a net-section fracture after a limited amount of flange yielding was noted in the beam. Testing of connection FS-04 was stopped after the beam developed a plastic hinge and the flanges sustained significant inelastic local buckling. Testing of connections FS-05, FS-06 and FS-08 was stopped after the beam developed plastic hinges and the flanges and webs sustained significant inelastic local buckling. Connection FS-07 failed by a net-section fracture of the beam flange, but only after significant yielding and localized flange buckling had occurred. The net-section beam-flange fracture began when the material between the bolt hole and the edge of flange fractured, as shown in Figure 1. The fracture then progressed across the remainder of the flange and into the web, as shown in Figures 2 and 3, before the experiment was stopped. Connection FS-09 failed when the bolts connecting the T-stub to the column flange fractured, though Schrauben (1999) reported that yielding was observed in the beam flanges and web prior to bolt failure. Testing of

Fig. 1. Initial fracture in the beam flange of connection test FS-07.

Fig. 2. Beam from connection FS-07 after disassembling the connection.

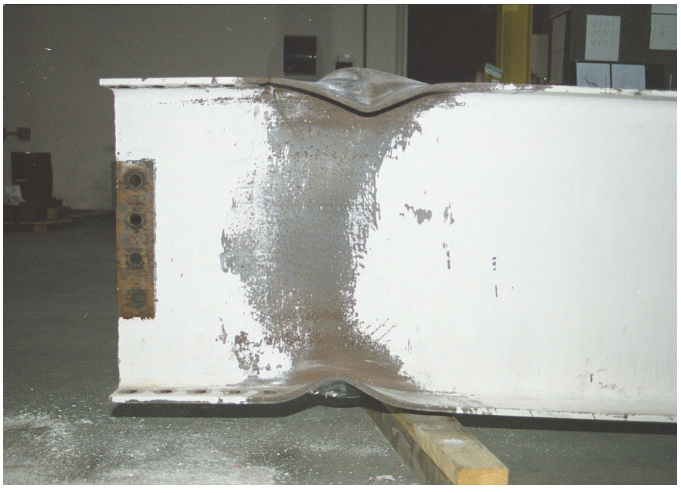

Fig. 3. Beam from connection FS-07. White-wash spalling indicates the formation of a plastic hinge.

Table 1. Details of Georgia Tech Connection Tests												
					Measured				@ Column Face		@ Crit Net Section	
Test ID	Beam Section	Bolt Diameter (in.)	Hole Diameter (in.)	Beam Grade	F_y (ksi)	F_u (ksi)	F_yZ_x (k-in.)	Expected Failure	$M_{Failure}$ (k-in.)	% Above	$M_{Failure}$ (k-in.)	% Above
FS-03	W21×44	⅞	0.938	A572-50	58.0	71.0	5,533	T-stub NSF	5,773	4%	5,405	–2%
FS-04	W21×44	1	1.063	A572-50	58.0	71.0	5,533	Beam FLB	5,949	8%	5,526	0%
FS-05	W24×55	⅞	0.938	A572-50	61.0	76.0	8,235	Beam WLB & FLB	9,363	14%	8,629	5%
FS-06	W24×55	1	1.063	A572-50	61.0	76.0	8,235	Beam WLB & FLB	8,642	5%	8,028	–3%
FS-07	W24×55	⅞	0.938	A572-50	61.0	76.0	8,235	Beam NSF	9,205	12%	8,483	3%
FS-08	W24×55	1	1.063	A36	53.8	70.7	7,263	Beam WLB & FLB	8,254	14%	7,527	4%
FS-09	W27×84	⅞	0.938	A572-50	59.1	78.3	14,420	T-stub T-Bolts	17,794	23%	16,105	12%
FS-10	W27×84	1	1.063	A572-50	59.1	78.3	14,420	Beam FLB/ Fixture	18,269	27%	16,660	16%
WLB - Web Local Buckling FLB - Flange Local Buckling				NSF - Net Section Fracture					Ave: 13% StDev: 8%		Ave: 4% StDev: 6%	

connection FS-10 was discontinued when the connection at one end of the column failed. Schrauben reported yielding and local buckling in the beam flanges and web along with extensive yielding in the T-stubs prior to stopping the test.

In all cases—even FS-03, which was stopped after a T-stub failure—the maximum moment developed at the face of the column during the experiment exceeded the expected plastic moment[1] of the beam. The experimental moment at the column was, on average, 13% higher than the expected plastic moment of the beam. Alternatively, the experimental moment at the critical beam section was, on average, 4.2% higher than the expected plastic moment of the beam.

University of Texas Tests

A series of five full-scale beam-column subassemblies was tested at the University of Texas at Austin in 1996 (Barbaran, 1996; Larson, 1996). These assemblies consisted of cantilever beams connected to pinned-pinned columns using a shear tab to resist shear and, in most cases, fully bolted T-stubs to resist moment. The first specimen was designed with a shear-only connection—with a shear tab but without T-stubs—so as to investigate the contribution of the shear tab and beam web to the moment strength of the connection. The second and third specimens were designed both with a shear tab and T-stubs, but the T-stubs were configured to provide only a partial-strength beam connection. The fourth and fifth specimens, indicated in Table 2 as DT04 and DT05, were designed with both a shear tab and T-stubs, with the tees in DT-04 proportioned to transmit 100% of the beam plastic moment to the column and the tees in DT05 proportioned to transmit approximately 125% of the beam's plastic moment (Barbaran, 1996). Values reported for F_y and F_u in Table 2 were measured during material testing performed at the University of Texas at Austin as reported in Larson (1996) for static loading of flat coupons cut from the beam flange parallel to the direction of rolling. The critical section noted in the table is the net section in the beam at the row of bolts farthest from the face of the column, though it should be noted that Larson and Barbaran indicated the presence of vacant holes farther from the column face in the beams of some specimens. The connections were loaded by applying a displacement to the ends of the cantilever beams.

Connection DT-04 failed when the bolts connecting the T-stubs to the column flange fractured. After disassembling the connection, small fractures near the bolt holes in the flange of the beam were noted as is shown in Figure 4. Testing of connection DT-05 was stopped when a fracture of the beam flange, shown in Figure 4, was noticed. Comparing the maximum moment observed at the critical section to the expected plastic moment of the section shows that the beams exceeded the expected plastic moment by margins of 3% and 19%.

1 When the yield strength was measured, either through mill certification or independent testing, the expected plastic moment is defined as $M_{pe} = Z_x F_{y,measured}$. In other cases, the expected plastic moment is defined as $M_{pe} = Z_x R_y F_y$.

Table 2. Details of University of Texas at Austin Connection Tests												
					Measured				@ Column Face		@ Crit Net Section	
Test ID	Beam Section	Bolt Diameter (in.)	Hole Diameter (in.)	Beam Grade	F_y (ksi)	F_u (ksi)	F_yZ_x (k-in.)	Expected Failure	$M_{Failure}$ (k-in.)	% Above	$M_{Failure}$ (k-in.)	% Above
DT-04	W36×150	1¼	1.313	A36	37.7	57.2	21,904	T-Bolts/ NSF	25,862	18%	22,533	3%
DT-05	W36×150	1¼	1.313	A36	37.7	57.2	21,904	Beam NSF	30,016	37%	26,152	19%
NSF - Net Section Fracture									Ave: 28% StDev: 13%		Ave: 11% StDev: 12%	

University of Illinois Tests

Again, as part of the SAC Steel Project, a series of eight full-scale beam-column subassemblies was tested at the University of Illinois (Schneider and Teeraparbwong, 2002). These assemblies, summarized in Table 3, consisted of cantilever beams connected to columns using bolted flange-plate connections to resist moment and shear tab connections to resist shear. Six of the tests incorporated W24×68 beam sections, and two incorporated W30×99 beam sections. Column sections were W14×120, W14×145 or W14×211 sections. Values reported for F_y and F_u in Table 3 are those reported on manufacturer's mill reports. The critical section noted in the table is the net section in the beam at the row of bolts farthest from the face of the column. The connections were loaded by applying a displacement to the free ends of the cantilever beams.

In one case (BFP-01), the failure was described as a heat-affected-zone fracture of the weld connecting the flange plate to the column flange. In a second case (BFP-08), the failure was described as a net-section fracture of the flange plate connecting the beam flange to the column. In all six remaining cases, the failure was described as a net-section fracture of the beam section. Oversized holes were used in the beam flanges in specimens BFP-01 and BFP-06. In specimens BFP-05 and BFP-07, "clamp plates" were included in the grip of the bolts at the critical section in an effort to push flange local buckling away from the net section of the beam and mitigate its effect on the net-section strength. Because these plates were not welded to the beam flange, they were not treated as flange reinforcement herein.

In all eight experiments—even BFP-01, which failed with a HAZ fracture, and BFP-08, which failed with a flange-plate fracture—the moment developed at the column face exceeded the expected plastic moment of the beam. The experimental moment at the column face was, on average, 23% greater than the expected plastic moment of the beam. Alternatively, the experimental moment at the critical

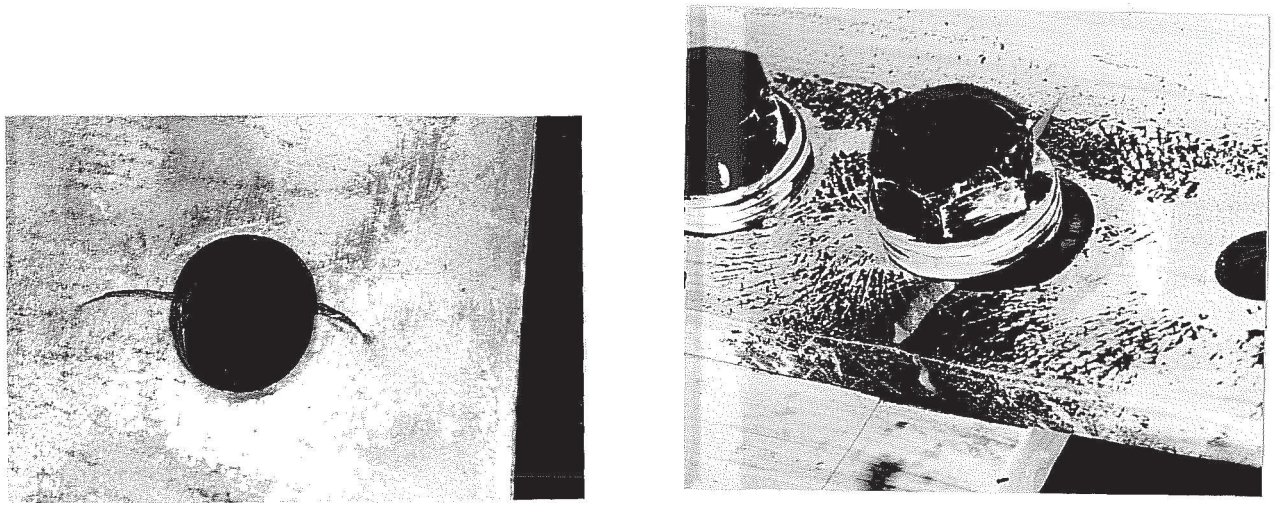

Fig. 4. Beam flange fractures in the University of Texas at Austin tests (Larson, 1996:) specimen DT-04 (left) and specimen DT-05 (right).

Table 3. Details of the University of Illinois Tests

Test ID	Beam Section	Bolt Diameter (in.)	Hole Diameter (in.)	Beam Grade	Mill Certified F_y (ksi)	Mill Certified F_u (ksi)	Mill Certified F_yZ_x (k-in.)	Expected Failure	@ Column Face $M_{Failure}$ (k-in.)	@ Column Face % Above	@ Crit Net Section $M_{Failure}$ (k-in.)	@ Crit Net Section % Above
BFP-01	W24×68	1	1.250	A572-50	56.0	74.0	9,912	HAZ Fracture	11,606	17%	9,377	–5%
BFP-02	W24×68	1	1.063	A572-50	56.0	74.0	9,912	Beam NSF	12,144	23%	10,868	10%
BFP-03	W30×99	1	1.063	A572-50	53.5	67.5	16,692	Beam NSF	21,362	28%	17,725	6%
BFP-04	W24×68	1	1.063	A572-50	56.0	74.0	9,912	Beam NSF	12,337	24%	10,505	6%
BFP-05	W30×99	1	1.063	A572-50	53.5	67.5	16,692	Beam NSF	21,390	28%	17,748	6%
BFP-06	W24×68	1	1.250	A572-50	56.0	74.0	9,912	Beam NSF	12,158	23%	10,616	7%
BFP-07	W24×68	1	1.063	A572-50	56.0	74.0	9,912	Beam NSF	12,379	25%	11,078	12%
BFP-08	W24×68	1	1.250	A572-50	56.0	74.0	9,912	FP Fracture	11,702	18%	9,582	–3%
										Ave: 23%		Ave: 5%
										StDev: 4%		StDev: 6%

HAZ - Heat Affected Zone
FP - Flange Plate
NSF - Net Section Fracture

BFP-01: Oversize Holes, Slip Critical Design
BFP-05: Used Clamp Plates Under Last Two Rows of Bolts
BFP-06: Oversized Holes
BFP-07: Used Clamp Plates Under Last Two Rows of Bolts

Table 4. Details of the UC San Diego Tests

Test ID	Beam Section	Bolt Diameter (in.)	Hole Diameter (in.)	Beam Grade	Measured F_y (ksi)	Measured F_u (ksi)	Measured F_yZ_x (k-in.)	Expected Failure	@ Column Face $M_{Failure}$ (k-in.)	@ Column Face % Above	@ Crit Net Section $M_{Failure}$ (k-in.)	@ Crit Net Section % Above
BFP-11	W30x108	1	1.063	A992	52.0	77.5	17,992	Beam FLB & NSF	23,643	31%	20,985	17%
BFP-12	W30x148	1	1.063	A992	58.5	80.0	29,250	Beam LTB	40,381	38%	33,350	14%
BFP-13	W36x150	1	1.063	A992	58.0	75.0	33,698	Beam FLB & NSF	47,375	41%	40,937	21%
										Ave: 37%		Ave: 17%
										StDev: 5%		StDev: 4%

FLB - Flange Local Buckling
NSF - Net Section Fracture
F_y and F_u for BFP-13 taken from Mill Certificates

section of the beam was, on average, 4.8% higher than the expected plastic moment of the beam.

University of California, San Diego Tests

A series of three full-scale bolted flange plate connections were tested at the University of California–San Diego to examine performance in special moment frames (Sato et al., 2007).[2] These assemblies, summarized in Table 4, consisted of cantilever beams connected to columns using bolted flange-plate connections to resist moment and shear tab connections to resist shear. Values reported for F_y and F_u were determined by coupon testing except for BFP-13, which are those reported on manufacturer's mill reports. The critical section noted in the table is the net section in the beam at the row of bolts farthest from the face of the column. The connections were loaded by applying a displacement to the free ends of the cantilever beams.

In BFP-11 and BFP-13, yielding and local buckling of the beam flanges and webs were noted prior to a fracture of the beam flange at the critical section. In both cases, some lateral-torsional buckling of the beam was observed. In BFP-12, lateral-torsional buckling of the beam led to the discontinuation of the experiment prior to failure of the beam, column or connection. In all three experiments—even BFP-12—the

2 Experiments BFP-1, BFP-2 and BFP-3, as reported in Sato et al., have been renumbered herein as BFP-11, BFP-12 and BFP-13, respectively, for ease of reference and to avoid confusion with the Illinois tests.

moment developed at the column face exceeded the expected plastic moment of the beam. The experimental moment at the column face was, on average, 37% greater than the expected plastic moment of the beam. Alternatively, the experimental moment at the critical section of the beam was, on average, 17% higher than the expected plastic moment of the beam.

University of Minnesota Tests

A series of eight experiments on high-performance steel plate girders was carried out at the University of Minnesota in an effort to quantify the rotational capacity of these sections (Altstadt, 2004). The girders were detailed with extremely thick top flanges to simulate the distribution of strain present in a fully composite bridge design. Specifically, the researchers were interested in determining if the newer high-performance steel possessed sufficient ductility—and thus, rotational capacity—to reach a full plastic moment, even under the severe strain distributions found in composite sections. The girders were tested by applying a point load at the mid-span of the girders. Four of these eight girders included a pair of bolted splices situated symmetrically about the mid-span of the girders. All of the bolt holes for these splices were drilled. The girders were built up of 8-in. × 3½-in. top flanges, 29-in. × ¾-in. web plates and 8-in. × ¾-in. bottom flanges. Additional details are provided in Table 5.

Three of the four girders failed with the development of a net-section fracture in the tension flange, with the fourth girder failing via lateral-torsional buckling prior to fracture of the tension flange (necking of the tension flange was observed, however). In three of four cases, the moment developed at the critical section exceeded the expected plastic moment of the section. The moment on the critical section was, on average, 4.3% larger than the expected plastic moment.

DISCUSSION

Considering all of the experiments described in the previous sections, there are 25 relevant data points. Considering all 25 experiments, the strength of the beams at the critical net sections was, on average, 5.7% larger than the expected plastic moment.

Because the strength of connection FS03 was limited by a failure mode not associated with net fracture of the beam flange, that experimental data point represents a lower bound to the net-section fracture strength of the beam. The same argument can be made for connections BFP01, BFP08 and GIR-7. If these experiments are excluded, the strength of the remaining beams at their critical net sections was, on average, 7.0% larger than the expected plastic moment. Going a bit further, if the scope of this paper is limited to sections with proportions similar to those expected in moment frames, GIR-6, GIR-8 and GIR-10 could also be excluded. In that case, the strength of the 18 remaining beams was, on average, 8.7% larger than the expected plastic moment with a corresponding standard deviation of 6.7%. It can also be noted that in only one of the remaining cases, FS-06, was the maximum moment at the critical net section lower than the expected plastic moment of the beam.

The remaining 18 admissible data points are shown as bold diamonds in Figure 5,[3] where the independent parameter is presented as the ratio of A_{fn} to A_{fg} and the dependent parameter is the measured moment capacity normalized by the expected plastic moment, or M_n/M_{pe}. A regression analysis of these 18 data points, shown as a dashed black line in Figure 5, yields a slope of 1.136 with an R^2 of 0.5448.

The cluster of gray data points in Figure 5 represents the normalized moment capacity of all tabulated W-shapes with ratios of A_{fn} to A_{fg} associated with two standard holes in each flange for bolts ranging from ½ in. to 1½ in. diameter using the provisions in Section F13 of AISC 360-16 (data points where a reduction in strength was not required are not shown). The cluster of gray data points can be conveniently represented using a line with a slope of 1.139. Note that the experimental data lie well above the line representing the provisions in Section F13 of AISC 360-16. Further, note that the provisions include a discontinuity for the moment capacity at the ratio of $A_{fn}/A_{fg} = 0.7692$, which corresponds to the ratio of $Y_T F_y/F_u$ for A992 steel, below which the provisions are particularly conservative. Finally, while the cluster of gray data points in Figure 5 represents all combinations of standard bolt holes in all possible beams without regard to workable gages or minimum edge distances, the author notes that fewer points would likely result if workable gages and minimum edge distances were taken into account.

Proposed Model 1

As was noted in the previous section, there is a discontinuity in the AISC 360-16 provisions at $A_{fn}/A_{fg} = Y_T F_y/F_u$. For A992 steel, this discontinuity corresponds to an offset in the curve of $M_n/M_{pe} = 1 - 0.8761 = 0.1239$ when $A_{fn}/A_{fg} \leq Y_T F_y/F_u$. One potential improvement would be to remove the discontinuity from the provisions in Section F13 of AISC 360-16 by simply shifting the sloped portion of the strength model shown in Figure 5 upward to provide a continuous, but not smooth, solution. This results in the solution shown as the lower of the two black lines in Figure 6, which will be referred to herein as proposed model 1a. The black diamonds in Figure 6 again represent the 18 pertinent data points.

---

3 Note that data points for BFP-03 and BFP-05 lie on top of each other, making it appear as though there are only 17 data points in the figure.

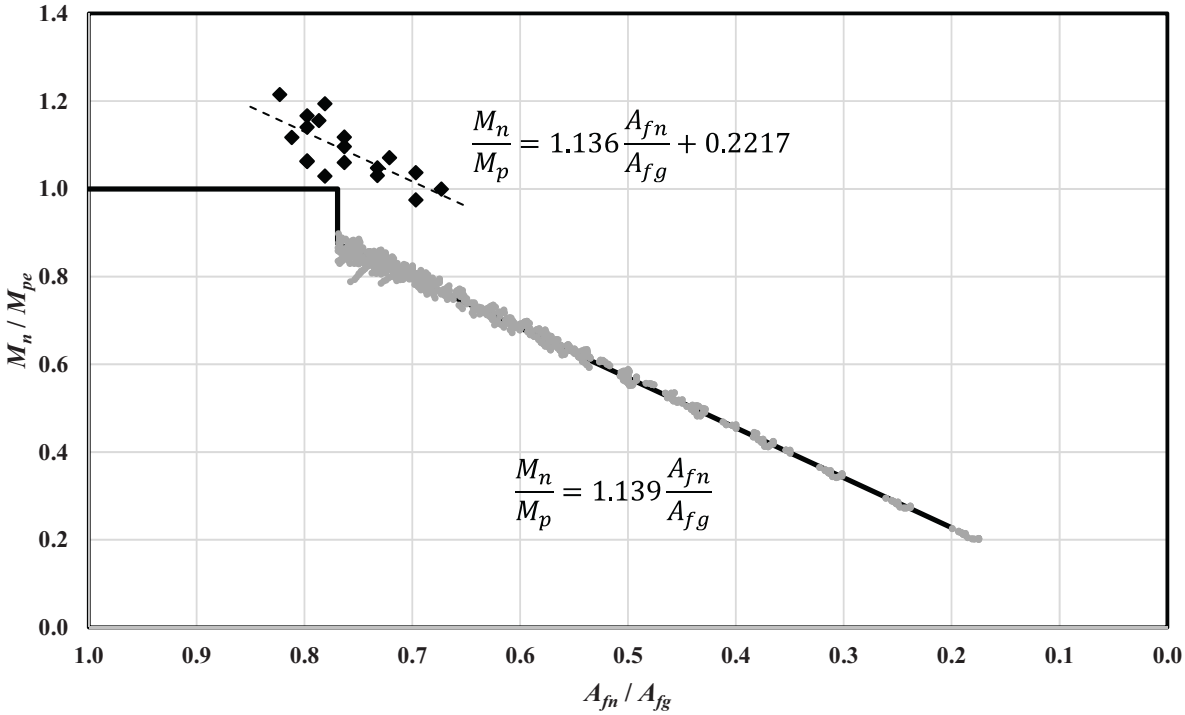

Fig. 5. Solution space for W-shapes with A992 steel for provisions in AISC 360-16.

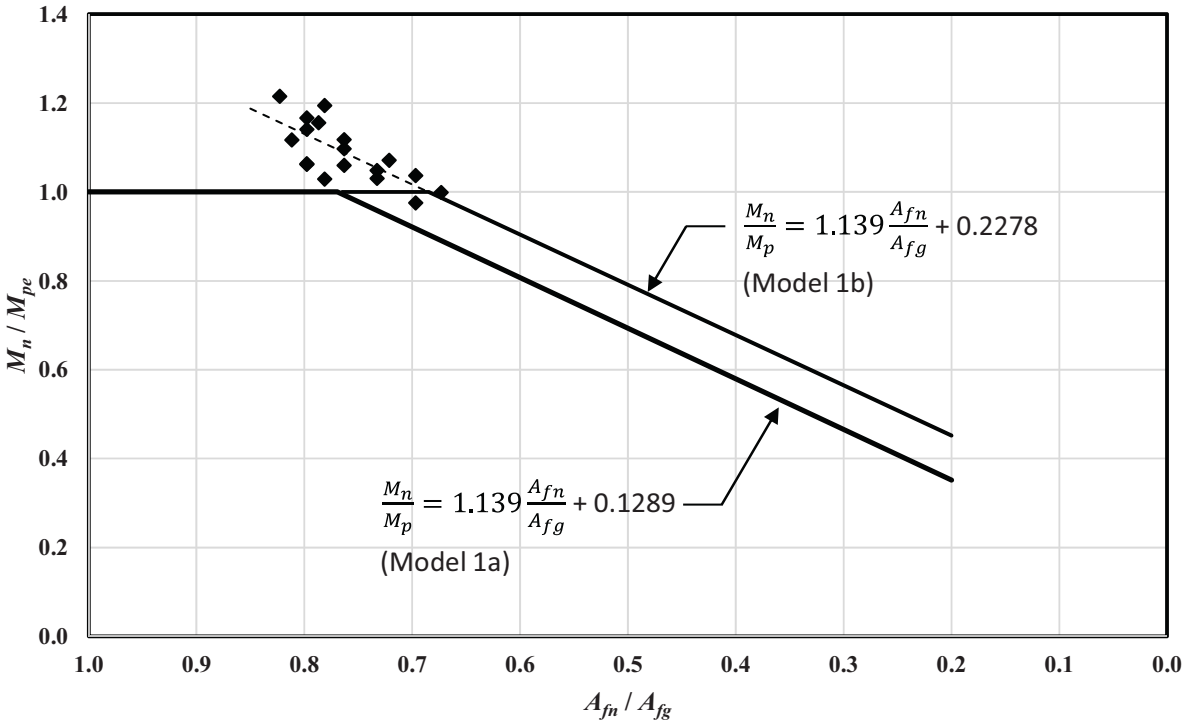

Fig. 6. Solution space for W-shapes with A992 steel for proposed models 1a and 1b.

Table 5. Details of the University of Minnesota Tests											
				Mill Certified				@ Center Line		@ Crit Net Section	
Test ID	Beam Section	Bolt Diameter (in.)	Tension Flange	F_y (ksi)	F_u (ksi)	Plastic Moment (k-in.)	Expected Failure	$M_{Failure}$ (k-in.)	% Above	$M_{Failure}$ (k-in.)	% Above
GIR-6*	Built-Up	1	A709-70W	90.0	103.0	3,141	NSF	3,460	10%	3,007	–4%
GIR-7	Built-Up	⅞	A709-70W	88.1	101.2	3,031	LTB	3,634	20%	3,091	2%
GIR-8	Built-Up	1	A709-70W	88.1	101.2	3,031	NSF	3,566	18%	3,097	2%
GIR-10**	Built-Up	⅞	A572-50	55.0	71.5	2,381	NSF	3,215	35%	2,794	17%
*GIR-6 Incorporated Oversized Holes			NSF - Net Section Fracture					Ave: 21%		Ave: 4.3%	
**R_yF_y and R_tF_u Reported for GIR-10 (F_y and F_u at nominal values)			LTB - Lateral-Torsional Buckling					StDev: 10.4%		StDev: 9.2%	

When $F_uA_{fn} < Y_TF_yA_{fg}$, this strength model, model 1a, could be presented mathematically as:

$$M_n = \frac{F_uA_{fn}}{A_{fg}}S_x + F_yS_x\left(\frac{Z_x}{S_x} - Y_T\right) \quad (8)$$

If the discussion is restricted to W-shapes rolled from A992 steel, where $F_u/F_y = 1.300$, $Y_T = 1.0$, and it is observed that on average $Z_x/S_x = 1.147$, then when $F_uA_{fn} < Y_TF_yA_{fg}$, model 1a could be presented mathematically as:

$$M_n = 1.139F_yZ_x\left(\frac{A_{fn}}{A_{fg}} + 0.1132\right) \le F_yZ_x \quad (9)$$

One shortcoming of model 1a, presented as Equation 9, is that it would still require a strength reduction for many beams that were shown experimentally to reach their expected plastic moment. Nine of the 18 beams would require a reduction in strength, wherein only one of those nine failed to achieve its expected plastic moment. In a different context, if these nine excluded beams were employed in a BFP connection, they would either be deemed not conforming to the specification or would require a reinforcement of the net section.

To address this issue, the constant in Equation 9 can be increased to shift the value of A_{fn}/A_{fg} that results in a need to reduce the moment strength of the beam. Using a constant of 0.2 instead of 0.1132—as is shown in Equation 10 and as shown as the upper black line in Figure 6, hereafter referred to as proposed model 1b—results in a reduced beam strength that matches very well with the regression analysis of the 18 experimental data points. This would correspond to the requirement of a strength reduction for beams with A_{fn}/A_{fg} less than 0.6850, which in turn corresponds to being able to employ the full plastic moment for all but one of the beams in the 18 data points.

$$M_n = 1.139F_yZ_x\left(\frac{A_{fn}}{A_{fg}} + 0.2\right) \le F_yZ_x \quad (10)$$

Proposed Model 2

The provisions in the double-tee chapter of AISC 358-16 address limits in the net section of the tension flange that will ensure that the plastic moment of the beam can be reached prior to a net-section fracture of the tension flange occurring. As a result, those provisions make no mention of a reduction in the flexural strength of a beam when the design check shown as Equation 7 is not satisfied. Still, a strength reduction can be inferred from Equation 7 if one assumes that the flexural strength would be equal to the lesser of the net-section moment at F_u and the gross-section plastic moment strength represented by the left-hand side and right-hand side, respectively, of the inequality in Equation 7. Doing so, and limiting the discussion to A992 steel, one can show that the moment strength when $Z_{x,net}/Z_x$ is less than 0.7692 can be represented as shown in Equation 11 and as shown in Figure 7 where the independent parameter is presented as the ratio of $Z_{x,net}$ to Z_x.

$$M_n = F_uZ_{x,net} = 1.300F_yZ_{x,net} \quad (11)$$

If the 18 admissible data points shown in Figures 5 and 6 are also plotted on this chart, a regression analysis can be performed as is represented by Equation 12 and shown in Figure 7. The R^2 value associated with this regression analysis is 0.4219. This relationship can be extrapolated to provide a moment capacity as shown in Figure 7, hereafter referred to as proposed model 2.

$$M_n = 1.895F_yZ_x\left(\frac{Z_{x,net}}{Z_x} - 0.2699\right) \le F_yZ_x \quad (12)$$

Proposed Model 3

If one considers the strength provided by Equation 4 but adds to it the plastic moment provided by the web of the sections, the following equation results, which will be referred to as proposed model 3a.

$$M_n = \frac{F_u A_{fn}}{A_{fg}} S_x + F_u Z_{x,web} \le F_y Z_x \tag{13}$$

The first term to the left of the inequality in Equation 13 represents the strength of the flange at fracture, while the second term to the left of the inequality represents the strength of the web when the flange is at fracture. It is acknowledged that, because the first term includes S_x, it inherently includes some contribution from the web of the section. It is noted, however, that S_x is dominated by the area of the flange. If model 3 is applied to all tabulated W-shapes with ratios of A_{fn} to A_{fg} associated with two standard holes in each flange for bolts ranging from ½ in. to 1½ in. diameter, then the cluster of gray data points shown in Figure 8 results (data points where a reduction in strength was not required are not shown). It can be seen that this leads to some scatter when plotted as a function of A_{fn}/A_{fg}, but the results provide a strong correlation to the experimental data.

Figure 9 shows the correlation that is obtained from model 3a when the model is applied to the 18 admissible connections using measured material strengths and compared to the experimental results. In Figure 9, both axes have been normalized by the expected plastic moment. The correlation is shown as the dashed line, which has a slope of 1.116 (i.e., a professional factor) and an $R^2 = 0.7278$. The regression analysis is performed on the 16 solid data points because experiments FS-09 and DT04 both failed via bolt fracture. These two data points, represented as open diamonds in Figure 9, were not included in the regression. In addition to the strong correlation, model 3a also has the advantage of correctly indicating which 16 of the 18 beams successfully reached their expected plastic moment before failing.

The possibility of capturing the web strength using F_y instead of F_u, as shown in Equation 14 and referred to herein as proposed model 3b, was also considered. The professional factor that was found for model 3b was 1.030 with an $R^2 = 0.7609$, both of which are better than for model 3a, but model 3b predicted that 6 of the 18 beams would fail via beam net fracture prior to reaching their expected plastic moment. While those six beams included the two that actually were not able to achieve their expected plastic moment, and because this paper is written with the bolted moment connection in mind, the author felt that this shortcoming was not offset by the superior professional factor. Thus, model 3b was not investigated further.

$$M_n = \frac{F_u A_{fn}}{A_{fg}} S_x + F_y Z_{x,web} \le F_y Z_x \tag{14}$$

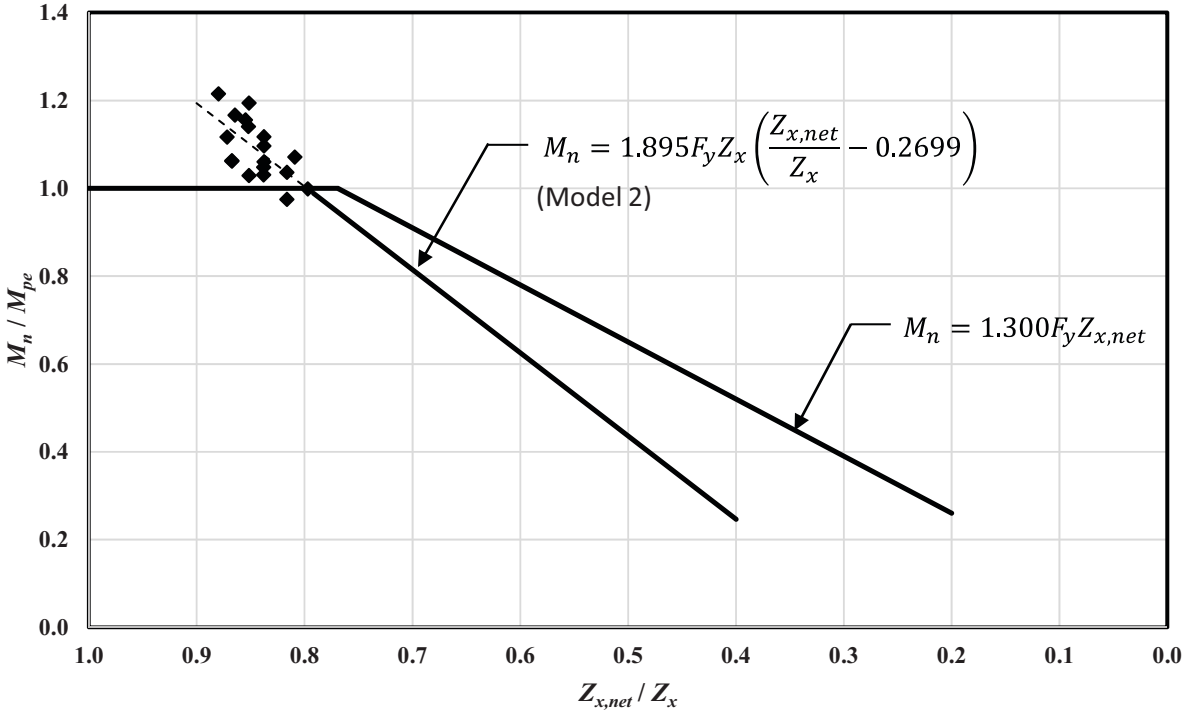

Fig. 7. Solution space for W-shapes with A992 steel for proposed model 2.

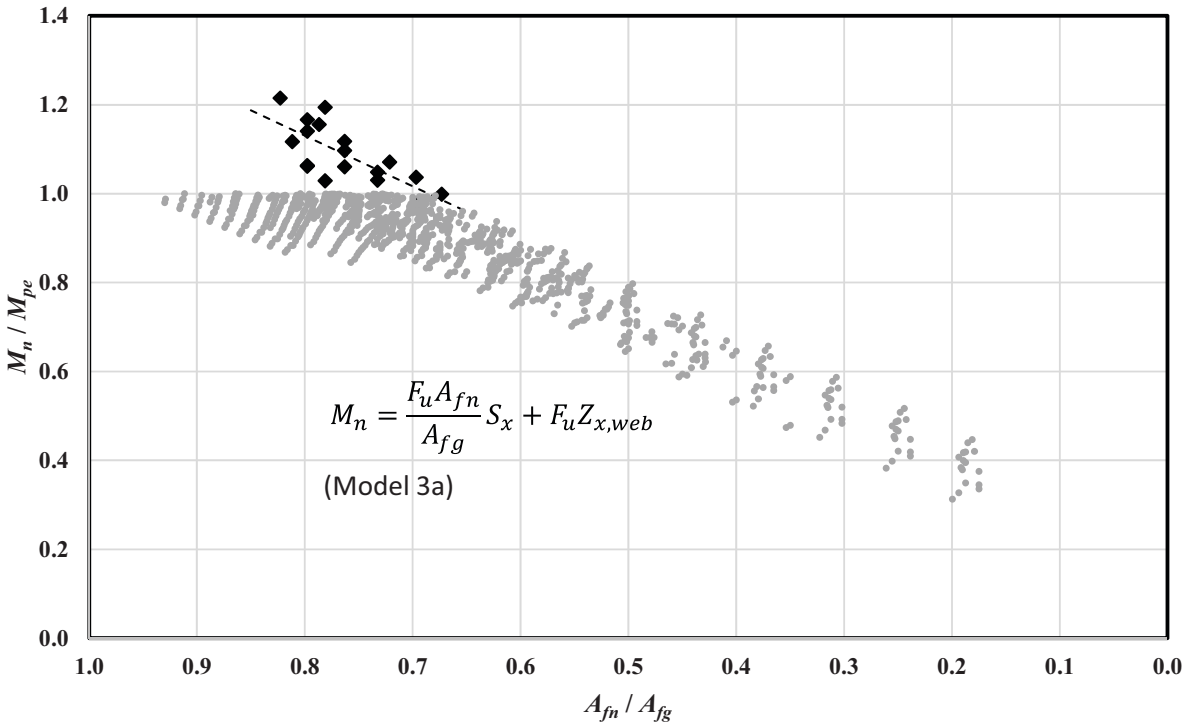

Fig. 8. Solution space for W-shapes with A992 steel for proposed model 3a.

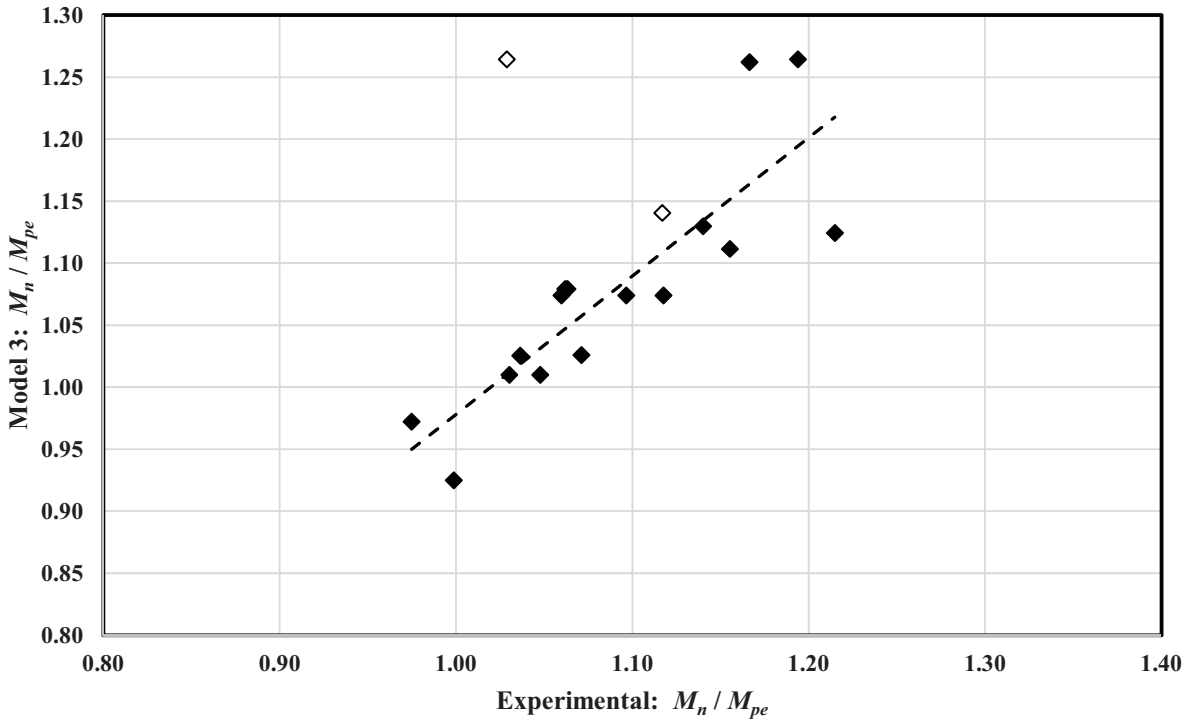

Fig. 9. Experimental correlation for proposed model 3a.

CONCLUSIONS

The experimental data summarized in this paper certainly show that beams with net sections that violate the design check in the 2016 AISC specification AISC 360-16 are, in many cases, able to reach the full plastic moment of their gross section before fracturing. Further, it is the opinion of the author that the provisions of Section F13 in AISC 360-16 are not rational because the strength model includes a discontinuity when examined as a function of the independent parameter, A_{fn}/A_{fg}. It is the author's opinion that the discontinuity at $A_{fn}/A_{fg} = Y_T F_y/F_u$ is excessively penal and unwarranted when compared to the experimental data.

Three models are proposed for the flexural strength of beams with holes in the tension flanges. Model 1 is based on a linear regression analysis of the experimental data with A_{fn}/A_{fg} as the independent parameter. Model 2 is also based on a linear regression of the experimental data but with $Z_{x,net}/Z_x$ as the independent variable. In both cases, the plastic moment of the beam is imposed as an upper limit of flexural strength.

Model 1 has the advantage of familiarity in that it, like the model in AISC 360-16, is a function of A_{fn}/A_{fg}. Model 1 also has the advantage of a slightly higher correlation constant of $R^2 = 0.5448$ compared to the $R^2 = 0.4219$ for model 2. Model 2, however, enjoys the advantage that it, in the opinion of the author, is more reflective of the mechanics associated with the failure mechanism that it is predicting because it is a function of Z_{net}, which is a parameter associated with flexure, as opposed to A_{fn}, which is a parameter associated with axial behavior. As such, model 2 inherently recognizes the contribution of the web in aiding the flanges in carrying moment and resisting a net-section fracture, whereas model 1 does not.

Model 3a enjoys the advantages of (1) having a rational basis, (2) being familiar to practicing engineers, (3) a strong correlation with experimental data with a professional factor of 1.116 and $R^2 = 0.7278$, and (4) being able to accurately predict which beam configurations will be able to reach their expected plastic moment. It is because of this that the author recommends model 3a for use in designing moment connections where components are bolted to the beam flanges.

It should be noted that all three proposals rely on extrapolation well beyond the limits of the existing experimental data. Prudence would demand that additional experimentation be conducted on beams at lower levels of A_{fn}/A_{fg} or $Z_{x,net}/Z_x$ to verify the applicability of the models before they are implemented. At a minimum, limits of applicability should be applied to the models based on the available data set.

REFERENCES

AASHTO (2016), *LRFD Bridge Design Specifications* 7th Ed., American Association of State Highway Transportation Officials, Washington, DC.

AISC (1999), *Load and Resistance Factor Design Specification for Structural Steel Buildings*, American Institute of Steel Construction, Chicago, IL.

AISC (2001), *Manual of Steel Construction,* 3rd Ed., American Institute of Steel Construction, Chicago, IL.

AISC (2005), *Specification for Structural Steel Buildings*, ANSI/AISC 360-05, American Institute of Steel Construction, Chicago, IL.

AISC (2010a), *Seismic Provisions for Structural Steel Buildings*, ANSI/AISC 341-10, American Institute of Steel Construction, Chicago, IL.

AISC (2010b), *Specification for Structural Steel Buildings*, ANSI/AISC 360-10, American Institute of Steel Construction, Chicago, IL.

AISC (2011), *Prequalified Connections for Special and Intermediate Steel Moment Frames for Seismic Applications*, Supplement No. 1, ANSI/AISC 358s1-11, American Institute of Steel Construction, Chicago, IL.

AISC (2016a), *Prequalified Connections for Special and Intermediate Steel Moment Frames for Seismic Applications*, ANSI/AISC 358-16, American Institute of Steel Construction, Chicago, IL, Public Review Draft, March 2015.

AISC (2016b), *Specification for Structural Steel Buildings*, ANSI/AISC 360-16, American Institute of Steel Construction, Chicago, IL, Public Review Draft, March 2015.

Altstadt, S. (2004), "Tensile Strength and Ductility of High Performance Steel Girders," M.S. Thesis, submitted to the faculty of the University of Minnesota.

ASCE A(2010), *Minimum Design Loads for Buildings and Other Structures*, ASCE/SEI 7-10, American Society of Civil Engineers, Washington, DC.

Barbaran, F.V.U. (1996), "Tension Bolt Behavior in Moment Connections for Seismic Applications," University of Texas at Austin.

Geschwindner, L.F. (2010), "Notes on the Impact of Hole Reductions on the Flexural Strength of Rolled Beams," *Engineering Journal*, AISC, Vol. 47, No. 1, 1st Quarter, pp. 37–40.

Kasai, K. and Bleiman, D. (1996), "Bolted Brackets for Repair of Damaged Steel Moment Frame Connections," *Proc. 7th US–Japan Workshop on the Improvement of Structural Design and Construction Practices: Lessons Learned from Northridge and Kobe,* Kobe, Japan.

Larson, P.C. (1996), "The Design and Behavior of Bolted Beam-to-Column Frame Connections Under Cyclical Loading," University of Texas at Austin.

Lilly, S.B. and Carpenter, S.T. (1939), "Effective Moment of Inertia of a Riveted Plate Girder," *Transactions of the ASCE,* Paper No. 2089.

Masuda, H., Tamaka, A., Hirabayashi, K. and Genda, I. (1998), "Experimental Study on the Effect of Partial Loss of Sectional Area on the Static Characteristics of H-Beams," *Journal of Structural and Construction Engineering (Transaction of AIJ),* Architectural Institute of Japan, No. 512, pp. 157–164 (in Japanese).

Sato, A., Newell, J. and Uang, C.M. (2007), "Cyclic Testing of Bolted Flange Plate Steel Moment Connections for Special Moment Frames," Final Report to the American Institute of Steel Construction from the Department of Structural Engineering, University of California, San Diego.

Schrauben, C.S. (1999), "Behavior of Full-Scale Bolted Beam-to-Column T-stub and Clip Angle Connections under Cyclic Loads," M.S. Thesis, submitted to the faculty of the Georgia Institute of Technology.

Schneider, S.P., and Teeraparbwong, I. (2002), "Inelastic Behavior of Bolted Flange Plate Connections," *Journal of Structural Engineering*, ASCE, Vol. 128 No. 4, pp. 492–500.

Smallidge, J.M. (1999), "Behavior of Bolted Beam-to-Column T-Stub Connections under Cyclic Loading," M.S. Thesis, submitted to the faculty of the Georgia Institute of Technology.

Swanson, J.A. (1999), "Characterization of the Strength, Stiffness, and Ductility of T-stub Connections," Ph.D. dissertation submitted to the faculty of the Georgia Institute of Technology.

Swanson, J.A. and Leon, R.T. (2000), "Bolted Steel Connections: Tests on T-stub Components," *Journal of Structural Engineering*, ASCE, Vol. 126, No. 1, pp. 50–56.

Yuan, Q. (2005), "Investigation of Hole Making Practices in the Fabrication of Structural Steel," Thesis, submitted in partial fulfillment of the requirements for the degree of Master of Science, University of Cincinnati.